# INFORMATION TO USERS

This manuscript has been reproduced from the microfilm master. UMI films the text directly from the original or copy submitted. Thus, some thesis and dissertation copies are in typewriter face, while others may be from any type of computer printer.

**The quality of this reproduction is dependent upon the quality of the copy submitted.** Broken or indistinct print, colored or poor quality illustrations and photographs, print bleedthrough, substandard margins, and improper alignment can adversely affect reproduction.

In the unlikely event that the author did not send UMI a complete manuscript and there are missing pages, these will be noted. Also, if unauthorized copyright material had to be removed, a note will indicate the deletion.

Oversize materials (e.g., maps, drawings, charts) are reproduced by sectioning the original, beginning at the upper left-hand corner and continuing from left to right in equal sections with small overlaps. Each original is also photographed in one exposure and is included in reduced form at the back of the book.

Photographs included in the original manuscript have been reproduced xerographically in this copy. Higher quality 6" x 9" black and white photographic prints are available for any photographs or illustrations appearing in this copy for an additional charge. Contact UMI directly to order.

**UMI**

A Bell & Howell Information Company
300 North Zeeb Road, Ann Arbor MI 48106-1346 USA
313/761-4700 800/521-0600

# FOURIER TRANSFORM INFRARED MICROSPECTROSCOPY OF BENIGN AND NEOPLASTIC CERVICAL SQUAMOUS EPITHELIUM

by

Luis Alberto Chiriboga

A dissertation submitted to the Graduate Faculty in Biochemistry in partial fulfillment of the requirements for the degree of Doctor of Philosophy, The City University of New York

1997

# Faculty Approval

This manuscript has been read and accepted for the Graduate Faculty in Biochemistry in satisfaction of the dissertation requirement for the degree of Doctor of Philosophy

4-6-97
Date

Chair of Examining Committee
Max Diem Ph.D

4-6-97
Date

Co-Chair of Examining Committee
David Zakim M.D.

4/16/97
Date

Executive Officer
Horst Schulz Ph.D

Examining Committee:

Dixie Goss Ph.D

Giorgio Inghirami M.D

Lawrence Kobilinsky Ph.D

Gary Quigely Ph.D

## Abstract

Fourier Transform Infrared Microspectroscopy Of Benign And Neoplastic Cervical Squamous Epithelium

by

Luis A. Chiriboga

Advisor: Professor Max Diem

Fourier transform infrared spectroscopy is a well established analytical method that is extremely sensitive to molecular composition and structure. More recently, Fourier transform infrared spectrometers have been coupled with traditional light microscopes yielding an extremely powerful tool to observe and collect molecular level information from complex samples. In this study, Fourier transform infrared microspectroscopy (FT-IRM) is used to analyze formalin fixed, paraffin embedded, cervical tissue biopsies. The goal of this work is to identify and characterize the infrared spectral signatures of the various cellular components found in benign and neoplastic cervical squamous epithelium. The methods for obtaining the infrared spectra of formalin fixed, paraffin embedded tissue biopsies is described. The infrared spectra collected from various epithelial components of benign and neoplastic cervical epithelium are presented. These spectra are evaluated in terms of the major biochemical components present within cervical epithelial cells. The spectra are also related to the observed histopathology. The results show that FT-IRM is able to distinguish between the normal anatomic layers of benign cervical epithelium. These spectra correlate well with the normal biochemical composition of cervical epithelium.

In neoplastic cervical epithelium, the spectra are significantly different. The observed spectral changes are consistent with the histopathology of neoplastic cervical epithelium. In addition, the morphologic changes seen in neoplastic cervical epithelium are mirrored by the infrared spectra. In conclusion, FT-IRM is capable of accurate and reproducible infrared measurement of precise anatomic locations based on correlation with observed histopathology in formalin fixed paraffin embedded tissue.

# Acknowledgments

Dedicated to my son, Matthew

and in memory of a friend.....

There are so many people who have helped me through the years, that to simply acknowledge them is not sufficient. To all of you, I offer my sincerest and heartfelt thanks for your advice, criticism, support, and patience.

I would like to thank my family. Your love and encouragement has sustained me through my academic pursuits. For this, I am truly indebted. To my wife, your constant love and support have given me the strength to complete my education. To my mother and father, your endless encouragement and commitment to my education have made this possible. To my sister, your honesty and kindness are unequaled. To Marian & Bob and Tonya & Bob, your love and support have given me peace of mind. I can never fully express my thanks.

I have had the good fortune of working with many wonderful scientist and physicians. It has been an honor and privilege to work under your expertise. To Dr. Max Diem, thank you for your time and energy. You have opened my eyes to the world of vibrational spectroscopy. More importantly, you have taught me a great deal about science itself. You have been an exceptional mentor and I will always be grateful. To Dr. David Zakim, your unrelenting drive and perseverance have made this work possible. I am indebted to you for letting me be a part of this scientific endeavor. To Dr. Giorgio Inghirami, your interest in my education has meant a great

deal to me. I will always be thankful for your encouragement and support. I would also like to thank Dr. Herman Yee for answering my endless questions and for all the engaging discussions we've had. Likewise, I am extremely grateful to Dr. Ping Xie for his valuable assistance and critical thoughts over the past few years. I would like to express my gratitude to John Lord, Peter Hoffmeister, Dr. Wei Zhang and Brian Mellen for their help during the preparation of this manuscript. To Robert Conrads and Herald Ritch, your professional wisdom is greatly appreciated. Without your generous support this project would never have been completed.

In addition, I would like to acknowledge the faculty and staff of Lutheran Medical Center. Thanks to Dr. Vincent Vigorita, Dr. Thomas Garven, Lisa Woody and Lawrence Adegbile for their invaluable assistance. I would like to thank the entire department of pathology for their kind help and technical assistance.

To all the faculty, staff and students of the City University of New York Graduate School and University Center, thank you for a wonderful educational experience. I am very grateful to Dr. Robert Rothchild and Dr. Lawrence Kobilinsky for their advice and guidance while an undergraduate student. Thanks to Dr. Dixie Goss for her support and assistance while I was a graduate student. A special thanks to Sophie Weintraub for her guidance and encouragement. To all my friends at CUNY: Igor, Ronnie, Brian, Les, Abajge, Ron, Bob, Kim, Ali, Sheryl, Susie, Terry, and Lisa (and many more), thanks for your support. Best wishes for the future.

Finally I would like to recognize the faculty and staff in the department of pathology at NYU Medical Center. I have made many friends over the last several years and have enjoyed working closely with all of you. I am very grateful to the following people for their support and encouragement: Dr. H. Feiner, Dr. S Gottesman, Dr. M. Vasquez, Dr. P. Thomas, Dr. C Rizk, Dr. M. Finfer, Dr C Finfer, Dr. A Edelman, Dr. L. Opitz, Dr. P. Zhang, Dr. F. Alfonso, Dr. S. Feinberg, U. Brown, S. Validahares, J. Sanchez, D. D'Amingo, P. Borrow, H. Hotaling, and J. Rocco.

# Table of Contents

# List of Tables

# List of Illustrations

# Chapter 1 : Introduction

Presently, the light microscope remains the most widely used instrument for studying histopathology. Supplemental techniques such as phase contrast which allows the study of living cells, and fluorescence microscopy which permits the characterization of expressed cellular proteins by immunohistochemistry, have expanded the domain of light microscopy. In contrast, the goal of infrared spectroscopy is to obtain quantitative and qualitative information of the interactions of molecules probed with infrared light. Similarly, but on a larger scale, the objective of light microscopy is to collect quantitative and qualitatively information from cells based on the appearance of cells under visible light. When infrared spectroscopy and light microscopy are combined, a new level of microanalysis is attainable. There is a natural synergy when these two techniques are joined. With the advent of Fourier transform infrared microspectroscopy (FT-IRM), previous difficulties in micro-sampling and cellular infrared analysis can be overcome. The primary advantage of FT-IRM is in allowing the analyst to select the sampling area for microspectroscopic analysis. In cells and tissues, the visualization of their respective geometry and location by FT-IRM adds valuable information and identifies specific features that were previously undetectable by FT-IR analysis. FT-IRM removes the requirements for physical separation of tissues into their individual components and/or implementing complex mathematical methods to identify and separate spectral components.

There is one potential problem in the analysis of cells and tissue by FT-IRM. Traditionally, infrared analysis of biological systems has focused on individual and

small clusters of molecules. In addition, there was typically other information available regarding the composition of the molecule(s) being studied. In contrast, eukaroytic cells contain millions of molecules with a high degree of variability in composition. As a result, an infrared measurement of an intact cell is an analysis of all the molecules, present in various proportions, in the tissue. Thus, analysis and correlation of infrared data collected from cells and tissue can only be presented in an elementary, qualitative fashion. Therefore the goal of this work is to define a method using FT-IRM for identifying and establishing the spectral patterns of various cellular components and to determine whether pathological specimens contain neoplastic cells identifiable by their infrared signatures. Formalin fixed, paraffin embedded cervical biopsies are an ideal source of tissue for this type of analysis. These specimens are readily available and do not require extensive pre-analysis preparation.

The importance of examining cervical disease is evident by the current issues facing the medical community. Invasive squamous cell carcinoma of the uterine cervix represents the most common malignancy of the female reproductive system in American women younger than 50 years of age (Qualters, Lee et al. 1992; Cannistra and Niloff 1996). In 1995, there were over 15,000 cases with 4,800 deaths associated with invasive cervical carcinoma (Cannistra and Niloff 1996). Age adjusted incidence rates (per100,000) fell from 34 in 1947 to 15 in 1970 (Blaustein 1982). The low incidence rate is attributable to cytology screening established in the early 1950's after the introduction of the PAP smear. In locations with high quality large scale screening programs, there has been over a 50% reduction in the mortality rate from cervical carcinoma. Nevertheless, the PAP smear screening test has inherent problems

associated with its methodology (Gustafsson, Sparen et al. 1995, Nieminen, Kallio et al. 1995). Although invasive carcinoma of the cervix can occur at any age between 17 and 90 years, there has been a shift in the age of incidence toward women under the age of 35 (Qualters, Lee et al. 1992; Austin, Degefu et al. 1994; Rakar, Kovacic et al. 1994; Cannistra and Niloff 1996). Cervical carcinoma is now detected more frequently in younger women because of the increase in the number of women being screened (Benedet, Anderson et al. 1992; Levine, Harper et al. 1993; Beral, Hermon et al. 1994). However, only half of U.S. women age 20 or older partake in cervical screening (Cannistra and Niloff 1996). Consequently, cervical malignancy continues to be a common and lethal disease in women.

## 1.1 Review Of Cervical Neoplasia:

Carcinoma (neoplasms originating from epithelial tissues) *in situ* (CIS) has been accepted as the precursor lesion of invasive squamous cell carcinoma (Blaustein 1982). However, the origin of CIS has remained a controversial topic. Much of the debate stems from differences in definition, terminology and the investigative techniques used to study the origins and history of pre-invasive cervical neoplasia. Early classifications stated that only lesions in which the full thickness of the epithelium is occupied by undifferentiated cells, should be classified as CIS (Blaustein 1982). This system did not address the instances in which lesions failed to span the entire thickness of the epithelium. As a result, lesions of this type were either followed, treated or ignored. In addition, the nomenclature used to describe these lesions varied from atypical hyperplasia and pre-canceroses to borderline lesion and dysplasia. Currently, dysplasia is the most widely used term and refers to an abnormal epithelial growth without any further mention as to the biological significance (Blaustein 1982). Finally, a working formulation for the classification of cervical lesions that do not occupy the full thickness of the epithelium was enacted. The system used a grading scheme that characterized the progressive increase in undifferentiated cells occupying the epithelium: one third (mild dysplasia), two thirds (moderate dysplasia), and the entire thickness (severe dysplasia/CIS) of the cervical epithelium. Hence, the system is a measure of the degree of cervical intraepithelial

neoplasia (CIN) and is defined as the spectrum of intraepithelial changes that begin with mild dysplasia and end with invasive carcinoma as shown in Figure 1:1. Each grade is commonly referred to as CIN 1, 2 or 3 respectively. The end stage of CIN/CIS is defined by a clone of cells breaking through the epithelial basement membrane and invading the underlying stroma. Currently, it is believed that invasion occurs at the CIS stage. Although there is no evidence to suggest otherwise, invasion may occur earlier as shown in Figure 1:1 (Blaustein 1982).

Consistent with the difficulties in defining dysplasia and carcinoma *in situ*, their diagnoses have historically been categorized as two distinct diseases. The principle notion separating the two states is the progression of the latter into invasive carcinoma. It has been estimated that 60 to 70% of CIS will develop into invasive disease. On the other hand, it has been suggested that dysplasia left untreated would either persist or regress and would rarely advance into invasive disease (Blaustein 1982). This concept is largely based on histologic observations and retrospective studies, which suffered from the same inconsistencies as mentioned previously. In support of the progression from dysplasia to CIS (and invasive carcinoma), are more recent clinical and laboratory studies. These results have altered the traditional view of the differences between dysplasia and invasive carcinoma (Cristoforoni, Favre et al. 1995; Saegusa, Takano et al. 1995; Comerci, Runowicz et al. 1996; Iwasaka, Matsuo et al. 1996; Shoji, Saegusa et al. 1996). In contrast to previous theories, it is now believed that there is a continuum between dysplasia and CIS, suggesting different stages in a common pathway. Studies have shown that changes occurring in dysplastic and CIS cells are qualitatively similar and remain consistent throughout the

progression of disease (Rosai 1989). Many of the alterations that occur in CIN and CIS (and also invasive carcinoma) are associated with the formation of an abnormal number of chromosomes (DiPaolo, Popescu et al. 1993; Heselmeyer, Schrock et al. 1996). Aneuploid chromosomal content is a common feature of non-endocrine dependent invasive cancer cells and is usually not present in benign neoplasms Additional studies have shown that 95% of CIN lesions are unifocal and confluent, indicating that the lesions arise from a single cell or at most a small group of cells (Blaustein 1982; Rosai 1989). The findings that qualitative features of early dysplasia are consistent with patterns found in invasive carcinoma presents strong evidence that dysplastic lesions are the pre-invasive component of cervical carcinoma.

The epidemiology of cervical neoplasia suggests that the disease is a continuum between CIN and invasive carcinoma (Stone, Zaidi et al. 1995). Epidemiological studies have found that first intercourse and first pregnancy at an early age, as well as a large number and short interval between pregnancies, are risk factors for the disease. Additional risk factors include frequent intercourse, multiple partners and poor hygiene. These findings indicate that cervical cancer is caused by a venereally transmitted virus. The two most likely candidates are Herpes Simplex Virus Type 2 (HSV-2) and Human Papillomavirus (HPV) (Shroyer, Lovelace et al. 1993; Jones 1995). Both HSV-2 and HPV have been found in patients with dysplasia and invasive carcinoma. Presumably, the viruses infect undifferentiated cells found in immature squamous epithelium. However, evidence to establish that either of these two viruses give rise to cervical neoplasia is unclear (Munoz, Bosch et al. 1994; Vecchione, Cermele et al. 1994). In principle, virally induced transformation of cervical

epithelium supports the notion that dysplasia and invasive carcinoma are part of a single progressive disease.

The most important feature, from a clinical perspective, is whether the disease has crossed the boundary from an intraepithelial dysplastic lesion to an invasive malignancy. The significance of this transition is readily apparent in the staging scheme developed by the International Federation of Gynecologists and Obstetricians (FIGO) shown in Table 1:1. The rationale behind the staging strategy is the direct relationship between the survival rate and stage of disease. Diagnostically, the most important consideration is to determine the clinical extent of the disease. This may be readily apparent in stages II through IV where the histologic degree of differentiation does not influence the clinical outcome significantly. In stage I, the relationship between histopathology, extent of invasion and clinical outcome is unclear Therefore, additional methods of monitoring the progression of the disease are needed to evaluate and more clearly define therapeutic strategies.

In stage I, the characterization of microinvasive carcinoma (MICA) has suffered a similar fate as the early classification system for dysplasia. Chiefly, there is no definite guideline for determining the relationship between extent and severity of disease. The common methods used to evaluate MICA are the depth of invasion and degree of vascular involvement (compared with the frequency of lymph node metastasis and disease recurrence) (Ostor 1993). Accordingly some characterize MICA by the presence or absence of vascular invasion or by the degree of lymphatic involvement (Bremer, Tiebosch et al. 1995; Elliott 1995; Benedet and Anderson 1996;

Benedetti-Panici, Maneschi et al. 1996). Others describe MICA by the depth of stromal invasion (Stewart and McNicol 1992; Jones, Mercer et al. 1993; Girardi, Burghardt et al. 1994; Benedet and Anderson 1996). In a study of 57 women with lymphadenectomies, lesions with limited stromal invasion and no vascular space involvement, had no potential for metastasis. Deeper lesions had only a slightly greater risk of lymph node metastasis as is shown in Table 1:2.

More recently the evaluation of surgical margins and determination of the lateral extent of MICA has become more important in the diagnosis of cervical malignancy (Ostor 1993; Benedet and Anderson 1996). Table 1:2 shows the relationship of the lateral extent of MICA and the remaining invasive disease in 134 women treated first by conization and then by hysterectomy. The greater the lateral extent of MICA in a cone biopsy, the greater the risk of finding residual disease in the hysterectomy sample. Likewise, evaluation of the surgical margins in cone specimens have shown that MICA with intraepithelial or invasive disease in the margin is often associated with residual disease in the hysterectomy specimen as shown in Table 1:2.

The prognosis for invasive cervical cancer depends on the extent of the tumor at the time of diagnosis. Surgery, radiation or a combination of surgery and radiation are the three basic elements used to treat invasive cervical carcinoma (Blaustein 1982; Rosai 1989). Stage 0 through Ia are typically treated by conization. However as mentioned, there is a high frequency (as high as 35%) of finding residual disease in hysterectomy samples after prior conization (regardless of the cause for residual disease) (Blaustein 1982). Thus, close follow up with cervical cytology is

recommended for patients treated with conization. For stages Ib through IIa, radical hysterectomy with bilateral lymhadenectomy is recommended to rule out lymphatic involvement. Radiation may be administered followed by radical surgery to treat these cases as well. For stage IIb through III the preferred treatment is combined external and intracavitary radiation (Blaustein 1982; Gershenson, DeCherney et al. 1993). The general 5 year survival rates for adequately treated cases of all stages is 60%. The survival rates according to FIGO clinical stages are: stage I, 85-90%; stage II, 70-75%; stage III, 30-35%; and stage IV, 10%. If lymph node involvement is discovered at any stage, the survival rates may decrease by up to 50% (Blaustein 1982; Rosai 1989). The main cause of death from invasive cervical carcinoma is ureteral obstruction leading to renal failure. Peritonitis following obstruction and perforation of the bowel as well as respiratory failure associated with pulmonary metastasis, are the other major causes of death.

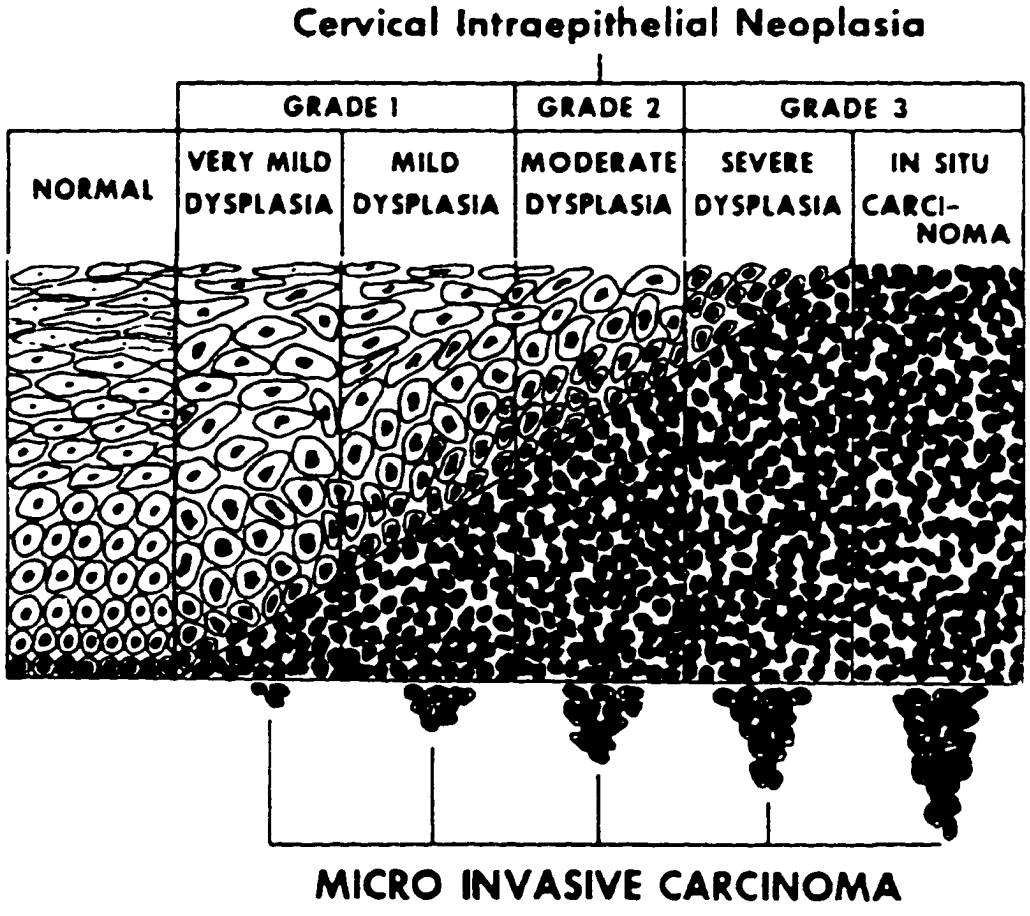


Figure 1:1 Illustration of the histopathology grading scheme for cervical intraepithelial lesions (adapted from Blaustein 1982).

Table 1:1 FIGO 1994 staging for carcinoma of the cervix uteri.

| *Stage* | *Description* |
|---|---|
| 0 | Carcinoma in situ, intraepithelial carcinoma |
| 1A | The carcinoma is strictly confined to the cervix |
| 1A-1 | Minimal microscopically evident stromal invasion |
| 1A-2 | Lesions detected microscopically that can be measured. The upper limit should not show a depth of 5 mm from base of epithelial surface. The horizontal spread must not exceed 7mm |
| 1B | Lesions of greater dimension than stage 1A-2 whether seen clinically or not |
| II | The carcinoma extends beyond the cervix but has not extended to the pelvic wall. The carcinoma involves the vagina but not as far as the lower third |
| IIA | No obvious parametrial involvement |
| IIB | Obvious parametrial involvement |
| III | The carcinoma has extended to the pelvic wall. The tumor involves the lower third of the vagina All cases with hydronephrosis or non-functioning kidney are included |
| IIIA | No extension to the pelvic wall |
| IIIB | Extension to the pelvic wall and or hydronephrosis |
| IV | The carcinoma has extended beyond the true pelvis or has clinically involved the mucosa of the bladder or rectum |
| IVA | Spread of the growth to other organs |
| IVB | Spread to distant organs |

Table 1:2 Comparison of depth, lateral extent and cone margins with the degree of residual disease (adapted from Blaustein, 1982).

| *Depth Of Invasion (mm)* | *Lymph Node Metastasis* |
|---|---|
| 1.0-3.0 | 0% |
| 3.0-5.0 | 2.7% |
| *Lateral Extent Of Invasion (mm)* | *Residual Disease* |
| <4 | 2% |
| <8 | 27% |
| >8 | 35% |
| *Cone Margins* | *Residual Disease* |
| Positive | 50-78% |
| Negative | 0% |

## 1.2 Review Of IR Spectroscopy Of Cells And Tissue:

The first attempts at collecting infrared spectra of tissue were performed in the late 1940's (Blout and Mellors 1949). Blout and Mellors examined formalin fixed paraffin embedded and fresh frozen tissue from normal and cancerous samples. Tissue sections between 4 and 50 microns thick were mounted onto silver chloride disks and covered with a drop of mineral oil or liquid fluorocarbon. Spectral data were collected on a dispersive instrument in the mid-infrared region between 5000 $cm^{-1}$ and 600 $cm^{-1}$. Blout and Mellors were able to correlate the strongest absorption bands with known functional groups and concluded that the bulk of the spectral features arose from the protein portion of the sample. There were significant differences between normal and neoplastic samples obtained from formalin fixed and frozen breast biopsy samples. The majority of these differences were localized below 1400 $cm^{-1}$ in the finger print region of the infrared spectrum. However, because the exact area from which infrared data was collected was not known, direct correlation between results and cellular composition could not be made. Similarly, comparisons between thick (50 micron) and thin (10 micron) sections were made without taking into account the anatomical heterogeneity of the tissue. These early results revealed the utility of infrared spectroscopy as a method to examine tissues. It also showed that it is possible to obtain molecular level information from specific pathological processes in

tissue samples. While the results were promising, the inability to define the exact sampling area made further interpretation difficult.

The first infrared microscope attachment was available commercially in 1953. It produced reasonable quality spectra although it was not utilized to any great extent (Kwiatkoski and Reffner 1987). It was not until the advent of Fourier transform infrared spectrometers that the convergence of spectroscopy and microscopy became a successful technique. Prior to this most biological infrared studies focused on measuring specific compounds within intact cells or tissue as a means to monitor cellular events. For example, Caughey's group at Colorado State University was developing a non-invasive method to detect carbon monoxide in blood samples for *in vivo* use (Alben and Caughey 1968; Maxwell, Barlow et al. 1974). In parallel, was the development of infrared techniques to analyze the average oxy- and deoxy hemoglobin equilibrium for clinical purposes (Alben and Caughey 1968; Jobsis 1977). By the late 1970's, infrared spectroscopy was firmly established as a method for the study of small ligands bound to metalloproteins in tissue (Maxwell and Caughey 1978). At the same time, O'Leary, at the Armed Forces Institute of Pathology in Washington DC, was able to detect the presence of abnormal amyloid in medullary carcinoma of the thyroid from deparaffinized tissue sections by transmission infrared spectroscopy (O'Leary and Levin 1985). To ensure that the abnormal protein was sampled, the protein had to constitute the majority of the specimen.

A few years later, Caughey was collecting data of single cells in suspension by FT-IRM. The spectra were obtained from human erythrocytes suspended in isotonic

buffer and placed between two barium fluoride ($BaF_2$) disks (Dong, Messerschmidt et al. 1988). A variable masking aperture was used to isolate and target the red cell to be measured. The spectra were of high quality and showed that they could detect carbon monoxide-hemoglobin moieties on an individual cell basis. Meanwhile, O'Leary had collected reflectance spectra by FT-IRM of paraffin embedded medullary carcinoma of the thyroid (O'Leary 1989; O'Leary, Engler et al. 1989). By using a gold coated microscope slide he could visually examine the area in which data was to be acquired by reflectance. Although the visual images were "fuzzy", they were of sufficient quality to establish location within the sample. The results were consistent with their earlier investigation. Separately, Benedetti had been investigating the spectral differences between normal and leukemic lymphocytes using standard FT-IR methods (Benedetti, Papineschi et al. 1984; Benedetti, Palatresi et al. 1985). Chronic lymphocytic leukemia (CLL) cells were obtained by separating the lymphocytes from peripheral blood. This methodology generated a relatively pure cell population for analysis. The cells were dried and mixed with potassium bromide to obtain pellets from which measurements were made. Spectral differences were mainly associated with changes in the bands corresponding to the phosphate vibrations of DNA. They also compared the solid state CLL cell results with measurements of different structural forms of DNA in aqueous phase. The changes in the phosphate bands were also observed in measurements of nuclei isolated from CLL samples (Benedetti, Palatresi et al. 1986). He also separated cells from malignant lung tumors and prepared mono-layers from the cell suspensions on $BaF_2$ windows. By using FT-IRM to measure different fields of the mono-layer, bands associated with sample

preparation could be eliminated (Benedetti, Teodori et al. 1990). The results indicated that there were notable differences between normal and tumor lung cells within the 1800-900 $cm^{-1}$ range.

By the 1990's, analysis of micro-biological systems by infrared spectroscopy had fallen into two groups. The first group is exemplified by Daudon's approach of using FT-IRM to identify urinary crystals that could not be distinguished by conventional morphological microscopic techniques (Daudon, Marfisi et al. 1991) Urine samples presenting with crystalluria were either centrifuged, filtered or evaporated to concentrate the urinary sediment. The crystals were separated visually from other particulate and then analyzed. With the FT-IRM method they were able to characterize several endogenous urinary products and drug compounds. They also examined crystals extracted from paraffin embedded renal biopsies (Estepa-Maurice, Hennequin et al. 1996). In order to facilitate characterization of the crystals, it was necessary to subtract spectra of the surrounding tissue from the spectra of the crystals. In this way they could compare the spectra of the unknown crystals with pure reference compounds. As in their earlier work, they were able to identify the crystals in all cases examined.

The second group approached the infrared analysis of cells and tissues. Rigas and Wong used FT-IR and pressure tuning IR to investigate the spectral patterns associated with human colorectal cancer (Rigas, Morgello et al. 1990). Small amounts of normal and neoplastic tissue were collected and frozen. Half of the tissue was used for infrared analysis. A frozen tissue section was collected from the adjacent area and

examined by standard histological methods to correlate the pathology of each tissue section with the infrared result. The colorectal tumor samples showed alterations to the phosphate and carbon-oxygen stretching bands as well as the carbon-hydrogen bending and carbonyl stretching modes when compared to normal tissue. However, no direct correlation between the tissue histology and the spectra was possible. Likewise the standard FT-IR studies did not take into account the distribution or architecture of colon tissue. Subsequently they used frozen colon tissue embedded in Optimal Cutting Temperature (OCT) or snap frozen in isopentane for analysis (Wong and Rigas 1990). The tissue was sectioned and placed between two $BaF_2$ windows. While the OCT embedded tissue contained contaminating bands from the embedding media, the snap frozen tissue produced high quality spectra. Despite these results, the question of tissue composition in the tumor was not adequately answered. To resolve this they utilized human colon cell lines and compared their spectra to the colon carcinoma data (Rigas and Wong 1992). The spectra were in good agreement, but the exact origin of the colon cancer spectra was still unknown. It was concluded that the malignant colon cell was responsible for the majority of the spectral changes since it resembled the patterns from the cell lines. Using the same methodology, Wong also examined exfoliated cervical cells (Wong, Wong et al. 1991). Exfoliated cells were collected from cervical brushes and suspended in saline. Half of the cell suspension was centrifuged and the pellet frozen in liquid nitrogen. The remainder was smeared and evaluated via the Papanicolau stain. FT-IR results showed that the normal samples contained reproducible bands at 1025 $cm^{-1}$ and 1047 $cm^{-1}$ corresponding to the $-CH_2OH$ modes as well as the -CO stretching and bending

vibrations of -C-OH groups. This was assigned to the carbohydrate complement of the cells. Wong *et al* assigned a band at 1082 $cm^{-1}$ to the symmetric phosphate stretching vibration. An assignment which we feel is incorrect in samples with high carbohydrate content (A: Chiriboga, Xie et al. 1997; B: Chiriboga, Xie et al. 1997; C: Chiriboga, Xie et al. 1997). The $PO_3^{-2}$ symmetric stretching mode corresponded to the band at 970 $cm^{-1}$. Similarly, the asymmetric stretching band of phosphate was present at 1244 $cm^{-1}$. It was concluded that the 1082, and 1244 bands arose from the phosphodiester groups of nucleic acids while the band at 970 $cm^{-1}$ originated from phosphorylated (monoester) proteins. A band located at 1155 $cm^{-1}$ and belonging to the C-O stretching vibration of C-OH groups was assigned by Wong to serine, threonine and tyrosine containing proteins of the cell with a minor contribution from carbohydrates. The bands at 1542 and 1652 $cm^{-1}$ (amide II and amide I, respectively) corresponded to the dominant amide group vibrations of proteins. Smaller bands located at 1401 and 1452 $cm^{-1}$ derived from the symmetric and asymmetric $CH_3$ bending modes were assigned to the methyl groups of proteins. The infrared spectra of the abnormal samples showed large differences between 950 and 1350 $cm^{-1}$. In particular the 1082, 1155 and 1244 $cm^{-1}$ bands were shifted to higher frequency. In addition, the ratio of peak intensities between 1025 and 1082 $cm^{-1}$ changed in favor of the band 1082 $cm^{-1}$. Derivative spectra and pressure tuning studies indicated that the changes affecting the 1244 $cm^{-1}$ band arise from the differences in hydrogen bonding of nucleic acids. Similar analysis for the band at 1155 $cm^{-1}$ showed that hydrogen bonding status also played a role in the alterations to the band. It was concluded that there were sufficient differences to distinguish between normal and malignant

exfoliated cervical cells. Similar evidence was obtained in a pressure tuning study of cervical tissue (Wong, Wong et al. 1993). In this study, tissue from normal and neoplastic areas were obtained following the same methodology as before. In addition, connective tissue was obtained by removing the epithelium from the stroma and the spectra of connective tissue were clearly distinguishable from the epithelial component. Comparable results were obtained by other groups using similar methodology (Morris, Lee et al. 1995; Wood, Quinn et al. 1996).

A number of important experimental considerations are missing in the approaches used above. First, the heterogeneity and distribution of tissue elements were not accounted for when evaluating the results. This is an important characteristic of tissue samples that should be considered. For instance, the anatomic architecture or organization of tissue serves as a reference map that establishes the relationship among cellular elements. This anatomical framework is used to evaluate the tissue's histopathology. Therefore, if the architecture is destroyed by grinding up the tissue, the spatial relationships are lost. Likewise, the spectral result will be influenced by the combination of these elements. The contribution of different components present in different proportions will directly affect the composition of the spectra. Similarly, analysis of tissue sections in which the infrared beam interrogation point is not known and/or the sample is poorly orientated, may produce erroneous or misleading results. This is especially important if the grade of disease is not taken into account. Second, conclusions drawn from non-scaled spectral results are misleading. For example, lack of scaling of data by Wong *et al*, leads to an over emphasis of spectral changes due to varying carbohydrate concentration (A: Chiriboga, Xie et al. 1997; B: Chiriboga, Xie

et al. 1997; C: Chiriboga, Xie et al. 1997). These changes are assumed to be due to the presence of disease. However, the variations do not necessarily arise from the presence of disease only. In order to establish the basis for more detailed studies, an investigation into the spectral properties of individual cellular components with respect to their spatial orientation is warranted. The cervix is an excellent candidate because of it's anatomical architecture and histological organization. Within the epithelium of the cervix there are landmarks that can be distinguished easily by histology and can facilitate analysis. The evaluation can be accomplished by accurately measuring the cellular constituents *in situ* by FT-IRM. In this way the anatomical and organizational composition is preserved and a direct correlation with the spectral results can be made. In the next section, the anatomy, histology, and pathology of the cervix will be reviewed. This will be followed by an overview of Fourier transform infrared spectroscopy.

## 1.3 Anatomy, Histology And Pathology Of The Cervix:

The cervix (taken from the Latin meaning neck) is the most inferior portion of the uterus. The entire cervix-uteri is divided into the corpus, isthmus and cervix. Collectively they are called the cervix-uteri and are one organ system as shown in Figure 1:2. The upper two-thirds of the uterus is called the corpus and is a pear shaped hollow structure. The narrow, lower end is connected to the cervix proper via the isthmus and makes up the lower third of the cervix-uteri. The cervix is cylindrically shaped and tapers slightly toward it's lower blunt end. The lower end projects through the anterior upper wall of the vaginal cavity. The vaginal wall is fused distally around the entire circumference of the cervix, dividing it into the upper supravaginal and lower vaginal portion (portio vaginalis). In the adult nulligravida, the cervix measures approximately 2.5 to 3.0 centimeters in length. The portio vaginalis also referred to as the exocervix, has a convex elliptical surface centered by a circular (nulligravida) or slit-like (parous) opening called the ostium (OS). The portio itself may be divided into the anterior and posterior lips. Typically, the anterior lip is shorter and projects further into the cavity than the posterior lip. The vaginal cavity communicates with the uterine cavity via the cervical canal and isthmus. The isthmus is frequently called the internal OS and is where the transition from cervical to uterine mucosa occurs. More precisely, the isthmus is interconnected to the external OS by an elliptical cavity measuring 8 millimeters at the greatest width. The lining of

the cavity consists of longitudinal mucosal ridges or plicae palmatae. More commonly this cavity is called the endocervix.

The cervical tissue is made up of an admixture of fibrous, elastic and muscular tissues. Fibrous tissue predominates making up approximately 15% of the connective tissue matrix. The muscular tissue is almost exclusively found in the endocervix, while the exocervix is virtually devoid of musculature. The portio vaginalis is covered with squamous epithelium from it's point of fusion with the vaginal wall to the OS. The cervical canal, from just below the isthmus to just above the OS, is lined with columnar epithelium. The transition from one tissue type to another may be rather abrupt and as a rule, the transition occurs just above the external OS. Anatomically this is called the squamocolumnar junction (SCJ).

The mucosa of the portio epithelium is composed of a non-keratinizing stratified squamous epithelium normally observed in three relatively distinct layers. Turnover of the epithelial cell population is accomplished by the processes of proliferation, maturation and desquamation during the reproductive period. This series of events is directly modulated by the ovarian hormones secreted during the estrus cycle. Estrogen (estradiol-17β) which quickly rises and reaches it's peak plasma concentration during the early part of the follicular phase, stimulates epithelial proliferation, maturation and exfoliation. During the luteal phase, progesterone (α-hydroxyprogesterone) concentrations increase and inhibit maturation. The hormones act on their target cells by binding to hormone receptors expressed by the epithelial cells in different stages of differentiation and maturation. Monoclonal antibodies

raised against estrogen and progesterone receptors have been used to study the expression patterns in cells of the portio epithelium (Nanogaki, Fujii et al 1990, Konishi, Fujii et al. 1991). Typically re-population of the epithelial mucosa takes 4-5 days. However the process may be accelerated up to 3 days by the administration of estrogen (Blaustein 1982).

In contrast, the mucosa of the endocervix is lined by a single layer of mucus-secreting columnar epithelium. Because the endocervical epithelium is not exfoliated, this mucosa does not undergo the same sequence of proliferation and maturation as the exocervix. Nevertheless, the secretory mucus is strongly influenced by the cyclic hormonal changes. Cervical mucus is a gel composed of glycoproteins in a plasma, rich in sodium and potassium chloride. During peak estrogen levels of the follicular phase, there is abundant mucus secreted that is watery and alkaline in composition. During this period, the mucus is in a favorable state for spermatozoa and increases the possibility of conception at the time of ovulation. When progesterone levels begin to rise during the luteal phase, the mucus changes, becoming less abundant, more viscous and somewhat acidic. These changes create an environment which decreases the likelihood that conception will occur. In fact, when an ovum implants into the uterine wall, hormonal stimuli cause an intense proliferation of endocervical cells. The mucus from these cells becomes thick and forms a plug that completely blocks the cervical canal, protecting the uterine cavity. These characteristics in association with other changes, lead to an event in which the endocervical epithelium moves out onto the exposed portion of the cervix. This process is known as endocervical eversion and occurs in a majority of ante- and postpartum cervixes.

During infancy and the pre-pubescent period, the endocervical epithelium is located above the external OS. This is called the "original " SCJ and has an abrupt transition as mentioned previously. During the reproductive period, the columnar epithelium may extend out onto the portio vaginalis generating everted endocervical epithelium. It is believed that the columnar epithelium is passively carried out onto the exocervix due to protrusion or laceration of the cervical lips during the gestational period. It is known that eversion occurs more frequently on the anterior lip of the portio vaginalis, although both lips may be simultaneously involved. As a result, a remodeling or reepithelialization process occurs in which immature squamous epithelium rapidly replaces or displaces the everted endocervical epithelium. The replacement by squamous epithelium of the everted endocervical glands is most likely a protective response. More importantly, the result is a more gradual transition of the SCJ. The region between the "original" SCJ and the new "functional" SCJ is called the transformation zone. The majority of young women who have been pregnant will exhibit a transformation zone, which may persist for long periods of time. In subsequent pregnancies, the process still occurs but to a lesser extent. In postmenopausal individuals, the transformation zone is absent because of decreased hormone levels as well as retraction of the cervical lips. Accordingly, the SCJ will move back above the OS toward its original position. While the exact mechanism and dynamics of this process are not understood, its impact on the clinical evaluation of the cervix is significant. Approximately 98% of early carcinomas arise in the transformation zone (Noda 1992).

When the portio epithelium is examined in cross section, three zones of cells can be seen. The lowest level or basal zone is responsible for epithelial renewal. The midzone contains the bulk of cells in various stages of differentiation and maturation. The uppermost level or superficial zone contains the most mature cells. Cells from the upper part of the midzone and the entire superficial zone are easily exfoliated and are the cell types most commonly found in cytological preparations.

The basal zone is composed of basal cells and is often referred to as the germinal cell layer. They present as one to two layers of cells oriented perpendicularly to the underlying fibrovascular stoma in what is commonly called the "picket fence" arrangement. Occasionally, the stroma penetrates up into the lower half of the epithelium forming stromal papilla. Separating the epithelium from the connective tissue is the stromo-epithelial junction. The junction consists of a basement membrane which is composed of a complex mucopolysacchride layer that is irregularly present. The function of the membrane is to provide a contact point for cell anchoring as well as a structural support for the epithelium. Basal cells are approximately 10 microns in diameter, round, and with scant cytoplasm. They have oval to cubodial nuclei with smooth nuclear contours and dense chromatin. These cells are the progenitor cells for the epithelium as is evident in their organization as well as occasional mitotic activity.

The lower part of the midzone contains larger cells that, because of their location, are called supra- or parabasal cells. They are larger than basal cells, averaging 15 to 20 microns in diameter and have an elliptical shape. Parabasal cells are held together by an array of tonofilament-desmosomal complexes. In addition,

they have multiple gap junction nexuses, which play an important role in celluiar communication and cell contact inhibition. Their cytoplasm is more abundant and stains pale blue with the standard hematoxylin and eosin stain. Intracytoplasmic glycogen makes its first appearance since enzymes crucial for glycogen synthesis are now expressed. Nuclei in parabasal cells are also slightly larger and have a more granular chromatin pattern. Occasional prominent nucleoli, as well as multinucleated forms, are observed sometimes. These cells are actively proliferating and may exhibit mitotic divisions. Autoradiographic studies have shown that parabasal cell nuclei have an increased uptake of tritated thymidine. Furthermore, recent immunohistochemical studies using a monoclonal antibody raised against proliferating cell nuclear antigen (PCNA) show that this layer is largely responsible for epithelial repopulation (Konishi, Fujii et al. 1991; Mittal, Demopoulos et al. 1993; Shurbaji, Brooks et al. 1993; Raju 1994).

The remaining upper two-thirds of the midzone is populated by intermediate cells. These cells are not proliferating but are involved in an upward maturation process. They are typically much larger than parabasal cells with a polygonal shape between 30 and 60 microns in diameter. When stained they exhibit abundant pale-pink to pink cytoplasm with a clear vacuolated appearance. The accumulation of large amounts of glycogen is principally responsible for the vacuolated appearance. There is evidence of mild keratinization. Keratin is a member of the intermediate filament family of structural proteins that renders the cell somewhat flatter. Cells from this layer also begin exhibiting cytoplasmic clearing that almost always is perinuclear. The nuclei of intermediate cells tend to be slightly smaller than that of parabasal cells.

Their round to oval shape and smooth nuclear contours remain constant until the cell matures into the superficial zone. Likewise, the chromatin pattern remains finely granular.

The final or upper zone, contains superficial cells. They are fully mature, terminally differentiated cells measuring between 40 and 60 microns in diameter. They have abundant cytoplasm rich in glycogen and microfilaments. The microfilaments provide the cell with added rigidity. Keratin is slightly more abundant causing the cells to be flatter and cornified. Collectively these characteristics cause the cytoplasm to stain deep pink to orange in color. The cells are devoid of desmosomes which explains their easy desquamation. Superficial cell nuclei are smaller than basal cell nuclei with a round featureless nuclear envelope. This type of nucleus is referred to as pkynotic and has dense chromatin. As terminally differentiated cells, their function is to protect the underlying mucosa. A summary of the morphological characteristics of cervical squamous epithelial cells is shown in Table 1:3.

As mentioned previously, the transformation zone is of clinical importance because virtually all cervical squamous neoplasia originates here. Histologically there are two mechanisms thought to be responsible for the reepithelialization process. The first consists of a direct in-growth of native squamous epithelium that is present at the outer margin of the eversion. The immature squamous epithelium inserts between the mucinous epithelium and its basement membrane. The squamous epithelium will expand as the squamous cells grow and mature upward. As a result, the endocervical cells are displaced and begin to degenerate, eventually sloughing off. This process is

believed to be responsible for replacement of the outer two-thirds of the cervix. The second mechanism is called squamous proplasia or more commonly squamous metaplasia. Metaplasia typically refers to a process in which mature cells are changed into another type of adult cell that would normally not be found in that anatomic location. In this context, metaplasia refers to a proliferation of undifferentiated subcolumnar reserve cells of the endocervical epithelium. This is evident by the appearance of small cubodial cells beneath the columnar cells of the glands. The reserve cells proliferate (reserve cell hyperplasia) and then differentiate into immature squamous epithelium. The epithelium grows in islands that expand and eventually connect together covering the glandular epithelium. The end result is a fully mature squamous epithelium that is identical to native portio epithelium. What makes this mechanism so engaging is that the subcolumnar reserve cells may also differentiate into mucinous endocervical cells, which are indistinguishable from normal columnar cells. The exact origin of reserve cells is not known and remains controversial. However, the presence of cells with the capability of differentiating along more than one pathway may play a role in carcinogenesis and the origin of invasive squamous cell carcinoma of the cervix. As a result of this complex process, squamous metaplasia is included as part of the differential diagnosis for CIN.

Two other physiological processes should be noted at this time, since they are also part of the differential diagnosis for invasive squamous cell carcinoma. They are both normal occurrences, but their morphological characteristics make careful examination a necessity. First is post-menopausal atrophy. In post-menopausal women there is a decrease in estrogen, which leads to an attenuation of epithelial

maturation. Consequently, the entire epithelium is composed of basal and parabasal cells. This shift in population may resemble neoplastic lesions that arise in the epithelium. One of the hallmarks of intraepithelial lesions is the absence of maturation of the epithelial cells. However, post menopausal atrophy lacks other key features, such as cellular pleomorphism, that are traits of neoplastic lesions.

The second process that must be examined cautiously is seen in the ante- or postpartum cervix. It is known as the decidual reaction and occurs in the stroma of the cervix. It presents as diffuse or patchy areas of large pale cells. The patches may appear to be attached to the under side of the surface epithelium. These stromal changes have been correlated to the actions of gestational hormones, presumably progesterone. In conjunction with decidual reaction there is a decrease in the maturation of cervical epithelium. Thus it is not surprising that this process may be misconstrued as a invasive neoplastic lesion. However, the lack of pleomorphic cells leads to the correct interpretation. It is important to remember that during pregnancy the cervix undergoes drastic changes in preparation for labor. There is increased vascularity resulting in edema as well as widespread destruction of collagen fibers and the accumulation of extracellular glycoprotein ground substance. All of this must happen prior to labor so that cervical softening and effacement can occur. The decidual reaction is part of this process and occurs in about one-third of post-partum cervixes seen histologically. Typically the decidual reaction disappears by two months after parturition .

As a result of the organization of the cervical epithelium, the cellular components may also be viewed from a functional perspective. Basal cells correspond to the germline for the cervical epithelium and are therefore undifferentiated cells. Mutations affecting this layer of cells will have the greatest impact on the stability of the epithelium. Parabasal cells are reproductive and proliferate forming a new generation of epithelial cells. Intermediate cells have stopped dividing but are differentiating and maturing upward. Superficial cells are the terminal products of differentiation and maturation whose duties are to provide structural stability and chemical resistance to the underlying epithelium. As a result of this functional progression, mitotic reproduction in the basal layer is balanced by desquamation at the surface. Under normal circumstances these two processes are maintained at a steady state. Thus it follows, that when differentiating cells abandon mitotic activity, they are locked into a pathway whose course is predetermined by the parent cells from which they arose. Yet, when errors occur in the germline, the differentiating cells may become trapped in an alternate pathway in which they no longer follow the guidelines for normal cellular organization and growth in that particular location. Changes in cell population dynamics in conjunction with cellular abnormalities provide strong histological evidence that a transformation has occurred in a cell population. This transformation process may be caused by any number of factors or may simply arise from accumulated errors. In any event, it is the timeliness and accuracy in which the transformed population is detected that will lead to a favorable outcome.

Nearly all patients with clinically visible cervical carcinoma present with abnormal vaginal bleeding (Blaustein 1982). Gross inspection of early lesions typically

show focal induration, shallow ulceration or slightly elevated granular areas that bleed readily to touch. Rigid histological classification of all cervical carcinomas has shown that 75-77% are squamous cell in origin. The remaining 25% consist of adenocarcinomas (neoplasms arising from glandular epithelium) and double primary carcinomas (neoplasms originating in both glandular and squamous epithelium) Adenocarcinomas of the cervix are distinguished from their squamous counterpart by a distinct, complex glandular pattern that permeates through two-thirds or more of the cervical stroma. Normally, the endocervix is characterized by a complex in-folded, pseudo-glandular organization that is maintained close to the surface of the epithelium The histologic hallmarks of squamous cell carcinomas of the cervix are recognized by the disruption in cellular organization and maturation as well as the display of cytoplasmic and nuclear abnormalities (see Figure 1:1) In fact, abnormal chromatin patterns are the single most important criteria used to distinguish CIN from other benign lesions. The abnormal chromatin patterns are seen at all levels of the epithelium regardless of the presence of cellular maturation. These patterns are also seen in the invasive component but the anaplastic cells tend to remain in the leading edge of the invasive epithelial component. The malignant cells within the epithelial portion of a cervical carcinoma are recognized by their hyperchromatic nuclei in which the chromatin is course and clumped throughout the nucleus. There is also large variation in nuclear size and shape with an irregular nuclear envelope. As the cells become more anaplastic, cytoplasmic membranes and intracellular bridges become less distinct. The cells progressively lose cytoplasmic maturation, with an accompanying loss of intracytoplasmic glycogen and cellular stratification. In

conjunction with greater degrees of anaplasia, there are more normal and abnormal mitotic figures at all levels of the epithelium. These cellular characteristics are typical of carcinoma *in situ* and persist in the epithelial component of an invasive carcinoma.

Once the neoplasm breaks through the plane of the basement membrane, the invading neoplastic tongue has ragged edges that contrast against the smooth and regular features of the basal layer and basement membrane. Neoplastic cells begin their invasion by encroaching directly onto collagen fibers of the cervical stroma. Typically the invading cells are better differentiated than their epithelial counterpart containing abundant cytoplasm and prominent nucleoli. The mechanisms that cause a specific clone (or clones) of neoplastic cells within the epithelium to invade the stroma is unknown. Presumably the invading cells lose their cellular attachments which decreases their cellular adhesiveness. An increase in lysosomal enzymes in conjunction with the loss of contact inhibition in all likelihood leads to the disruption of the basement membrane and allows penetration into the stroma by neoplastic cells.

Invasive squamous cell carcinomas can be broken down into three histologic grades based on the degree of differentiation of the lesion. The largest proportion of squamous cell carcinomas are grade 2 or moderately differentiated carcinomas followed by poorly differentiated grade 3 and well differentiated grade 1 carcinomas. In general, all cervical squamous cell carcinomas are characterized by large solid masses of neoplastic cells infiltrating into the stroma. The margins of the infiltrating nests are characteristically ragged and irregular.

Morphologically, well differentiated lesions exhibit profuse amounts of keratin which is deposited as concentric whorls (keratin pearls) in the center of nests of tumor cells. The neoplastic cells are well differentiated and have abundant eosinophillic cytoplasm. Cellular dyskeratosis (keratinization) is clearly evident as an intense cytoplasmic eosinophillia. Occasionally, neoplastic cells lack the eosinophillic characteristics often seen in these lesions. This is due to the accumulation of intracytoplasmic glycogen that typically is absent in invasive squamous cell carcinoma The nuclei of these cells are large, irregular and hyperchromatic. Within the nests, the cells are tightly packed and have well developed intercellular bridges. The cells appear mature and some minimal stratification is evident especially around the periphery of keratin pearls. The advancing edge of the invading mass of cells typically contains the maximum concentration of mitotic divisions. This is also where the host meets the leading edge of the tumor with an inflammatory response.

In moderately differentiated lesions, the neoplastic cells are more pleomorphic than in grade 1. They have less cytoplasm and large irregular nuclei. The cell borders and intercellular bridges are indistinct. Individual cellular dyskeratosis is present and concentrated at the center of the tumor nests. However in contrast to grade 1, there is no keratin pearl formation. In addition there is an increase in mitotic figures, which are more evenly distributed throughout the tumor mass. Grade 3 carcinomas tend to be composed of masses of anaplastic cells with hyperchromatic oval nuclei and scant cytoplasm similar in appearance to the basal cells of CIN 3. The cell membranes are indistinct and some cells exhibit abortive dyskeratosis. Mitotic figures are abundant. Large areas of necrosis may appear centrally within the nests of tumor cells.

Occasionally, poorly differentiated lesions are composed of large pleomorphic cells with giant distorted and deformed nuclei. This variant also exhibits a large number of abnormal mitotic figures.

The anatomical distribution of early invasive carcinoma can be traced back to the underlying CIN lesion. Although there is no current consensus on the cellular origins of CIN lesions, three cellular sites have been proposed. They are: basal cells of the native portio squamous epithelium, basal cells of the transformation zone epithelium, and reserve cells of the endocervical columnar epithelium. In almost all cases the distribution of the CIN lesion mirrors the distribution of both the everted endocervical epithelium and the transformation zone. Therefore, the area of the transformation zone predetermines the extent and distribution of the CIN lesion (Blaustein 1982; Gershenson, DeCherney et al. 1993). Colposcopic, colpomicroscopic and histologic observations have shown that essentially all CIN lesions originate at the squamocolumnar junction of the transformation zone (Noda 1992; Ostor 1993). CIN lesions have been observed to expand horizontally and may involve the entire transformation zone. However the lesions stop abruptly at the junction with the native portio epithelium. The line defining this point is sharp and perpendicular to the surface. In general the exocervical portion of the CIN lesion (the most exposed component) is well differentiated while the endocervical component tends to be less well differentiated. Thus it is proposed that CIN lesions arise from the coalescence of reserve cells of the everted endocervical epithelium and basal cells of the native portio epithelium of the transformation zone epithelium.

In summary, the histopathological distinction between normal and neoplastic cervical tissue is based primarily on morphological features of the cells and their architectural organization. The morphological changes are rooted in alterations and modifications of the structural, metabolic and functional pathways of the cell. Therefore biochemical molecular events precede the morphological transformation. Because infrared spectroscopy is sensitive to molecular level interactions, early biochemical molecular changes can be observed with this methodology. The following section will present a brief overview of the principles that allow these observations to be made.

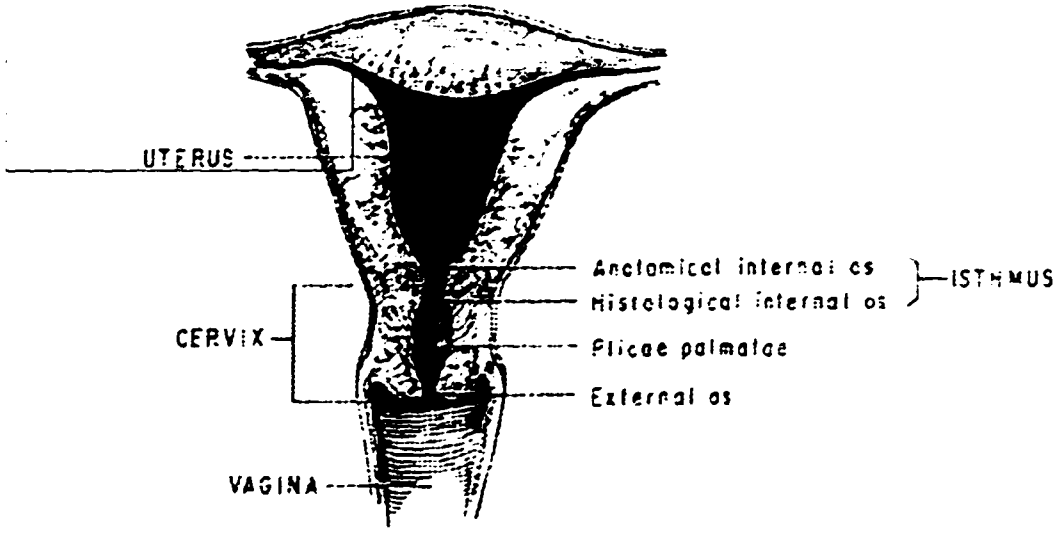


Figure 1.2 Frontal section view of the cervix uteri showing some of the anatomical landmarks [Adapted from Kristners Gynecology Principles and Practice 5th ed 1990]

Table 1.3 Morphological characteristics of normal cervical epithelial cells

| *Criteria* | Basal | Parabasal | Intermediate | Superficial |
|---|---|---|---|---|
| Size | 8-10μ | 15-20μ | 20-60μ | 40-60μ |
| Shape | Round | Round - oval | Polygonal | Polygonal - round |
| Amount of Cytoplasm | Scanty | Adequate | Abundant | Abundant |
| Cytoplasmic Stain | Deep blue | Pale blue | Pale-blue to Pale-pink | Pink to orange |
| Cytoplasmic Vacuolization | None | Occasional | Abundant | Occasional |
| Nuclear Size | 7-9μ | 8-13μ | 10-12μ | 5-7μ |
| Chromatin Pattern | Coarse and dense | Granular | Finely granular | Dense and pyknotic |

## 1.4 Theory And Practice Of Fourier Transform Infrared Spectroscopy:

In absorption spectroscopy, the absorption of electromagnetic radiation by atoms and molecules is observed. The absorption phenomenon occurs between discreet energy states of atoms and molecules. Infrared spectroscopy is a subdivision of absorption spectroscopy in which the interaction of infrared electromagnetic radiation with the vibrational energy levels of molecules is measured. Infrared radiation is a relatively wide band of the electromagnetic spectrum covering wavelengths between 0.70 and 300 microns. In comparison, visible radiation has a narrower band width with wavelengths between 0.30 and 0.70 microns. When an interaction takes place, specific wavelengths of incident radiation are absorbed by a molecule. The resulting loss of radiation is measured in the infrared experiment. For any given molecule, there are a large number of internal vibrations that produce a highly complex absorption spectrum. The spectrum is characteristic of the functional groups and configuration of the molecule and may be used to quantitatively and qualitatively describe the molecule. In order to further understand the absorption process, an empirical model will be used to illustrate the infrared experiment.

Consider the molecule acetaldehyde shown schematically in Figure 1:3. In this illustration, the molecule is symbolized by a mechanical model in which the atoms are represented by spheres. The spatial arrangement of the model closely approximates its actual geometry. The size and weight of each ball corresponds proportionally to the

atomic radius and mass of each respective atom. Likewise, the atoms are held together by springs that approximate the bond lengths and forces that hold the atoms together. If this model were suspended in space and a mechanical force applied, the balls would appear to undergo random periodic motion. The oscillations or vibrations of the model are similar in nature to the real vibrations in a molecule and may be described by classical Newtonian mechanics. In order to simulate the experiment, the model could be viewed with a variable frequency strobe light. As the frequency of the strobe light is varied, some combinations of balls in the model would appear to become stationary. This effect occurs when the frequency of the strobe light approaches the frequency of the oscillating group in the model. When the spheres appear motionless, the exact frequency of the vibration is known. The vibration of a group in the model depends on the mass of each ball and the forces acting upon the springs. The lack of motion of a particular group could be plotted as a function of the frequency of light. The resulting curve would be characteristic for that particular group in the model. While this is a fairly accurate representation of the real motions of atoms, it does not completely describe the mechanism in which light interacts with molecular vibrations. However, the model does illustrate two integral components of the process. First, atoms and the bonds between them determine the relative frequencies of the vibrations. Secondly, the interaction with light allows the visualization of characteristic absorption patterns.

The electromagnetic spectrum is typically broken down into various regions established in practice by the different instrumental methods used to measure and detect the light. As a standard, the infrared region of the electromagnetic spectrum is

divided into three parts known as the near, middle and far infrared. The most active of these regions is the mid-infrared which has wavelengths between 3 and 15 microns (*ca* 3000-600 $cm^{-1}$). By convention, the wavelength of light used is not expressed in microns. Instead, the wavenumber is used to describe infrared spectra and is given by:

$$\tilde{\nu} = 1/\lambda \qquad (1.1)$$

where the wavenumber, $\tilde{\nu}$, is defined as the number of waves per centimeter and is expressed in units of reciprocal centimeters ($cm^{-1}$). While each region is usually described by the wavelength or wavenumber, it may also be characterized in terms of energy. This is an important consideration because an exact amount or quantum of energy must be supplied for an absorption event to take place. The relationship between the frequency and wavelength of electromagnetic radiation is give by:

$$\nu = c/\lambda \qquad (1.2)$$

where $\lambda$ is the wavelength in centimeters, $\nu$ is the frequency in hertz and $c$ is the velocity of light. The relationship between energy and frequency is given by:

$$E = Nh\nu \qquad (1.3)$$

where $E$ is the energy of an Avogardo's number, $N$, of photons and $h$ is Plank's constant[1]. Therefore, when a molecule absorbs radiation at a given wavelength, each

[1] Velocity of light = $2.998 \times 10^{10}$cm $sec^{-1}$, Avogardos's number = $6.023 \times 10^{23}$, Plank's constant = $6.624 \times 10^{-27}$erg sec.

mole absorbs an amount of energy $E$ that can be expressed in kilocalories per mole The energies associated with the mid-infrared range are on the order of 1 to 10 kilocalories per mole and correspond to the major differences between vibrational states.

Accordingly infrared radiation can also be thought of in terms of energy, including kinetic energy. When a molecule is heated, the kinetic energy of the molecule increases causing an increase in all forms of molecular motion. In a small molecule, the majority of the energy is converted into translational motion causing the molecules to move about at greater rates relative to one another. However in larger systems, the energy absorbed manifests itself as an increase in vibrational motion. As more heat is applied, higher vibrational states are achieved, which cause the average bond distance between the atoms to increase. Obviously, the bonds will break when sufficient energy is supplied. The process of bond dissociation requires a significant amount of energy. For instance, a carbon-hydrogen bond requires approximately 100 kilocalories per mole of energy for the atoms to dissociate. Thus, the energy levels of radiation used in an infrared experiment are several times lower than the actual bond dissociation energies. This and other factors show that any direct disruption of the molecular bonds is unlikely in an infrared experiment. The actual energy required to measure a vibration is a function of the difference in energy between the ground state and the first excited state of the molecule. In the case of the acetaldehyde example, the equivalent situation is the difference between the model at rest and in motion.

At this point, the comparisons between our model and a real molecule begin to break down. This is because real molecules are in constant motion and typically vibrate about average values of interatomic distances. The difference between the frequency of one vibrational state with respect to another is associated with a specific energy level and is therefore quantized. At room temperature, the molecule is mostly in its lowest or ground vibrational state. When absorption of the appropriate energy occurs, the molecule moves to a higher vibrational state in which the amplitude of the vibration is larger. If the two different vibrational states are connected by a difference in dipole moment, the interaction is an observable event. The change in dipole moment of the molecule generates an electric field that oscillates as the interatomic distance changes between the atoms. This electric field can couple with the oscillating electric field of the incident radiation resulting in the absorption of a quantum of light energy.

Diatomic molecules are the simplest form of a vibrating molecular system. In a diatomic molecule, the only vibration is the stretching of the bond separating the two atoms. To a first approximation, we may consider this vibration as a simple harmonic oscillator. In classical mechanics a simple harmonic oscillator is represented by two masses connected by a spring (as in the mechanical model). When the system is perturbed, the force that restores the mass to its equilibrium position is constant for small displacements. This is known as Hooke's law and can be applied towards the quantum mechanical treatment for a diatomic molecule. The fundamental vibration frequency $\nu_0$ for a diatomic molecule can thus be given by equation 1.4 where $k$ is the force constant and $\mu$ is the reduced mass of the two atoms. Therefore the fundamental

vibration frequency of a bond depends on the masses of the vibrating atoms and the restoring force constant. The greater the force constant, the higher the fundamental vibrational

$$\nu_0 = \frac{1}{2\pi}\left(\frac{k}{\mu}\right)^{1/2} \qquad (1.4)$$

frequency and the larger the energy space between vibrational states. On the other hand, the masses are inversely related to the vibrational frequency. The lighter the atom the higher the frequency of its vibration. Therefore the mechanical model is consistent with a real molecular system in that a small weight will oscillate faster on a spring than a larger weight. In acetaldehyde, the carbon-hydrogen vibration is found at a higher frequency (ca 2800 $cm^{-1}$) than the carbon-oxygen vibration (*ca* 1725 $cm^{-1}$).

In polyatomic molecules the situation is more complex because there are many more vibrations possible than just stretching vibrations. In fact, there are two types of fundamental stretching vibrations, symmetrical and asymmetrical as shown in Figure 1:4. In addition to these there are bending or deformation modes that are also shown in Figure 1:4. Each of these fundamental vibrations in a molecule may be described in terms of normal modes. It is assumed with this treatment that the atoms themselves move in straight lines and in phase with each other such that the center of mass of the molecule does not move. As a result of this approximation, different atoms can move different distances giving each vibration a characteristic vibrational frequency or normal mode. The vibration of the entire molecule may then be described by the sum of displacements of the normal modes.

In order to describe the displacements of $N$ atoms in a polyatomic molecule, three Cartesian coordinates may be used to account for their position in space. As a result the molecule can experience $3N$ degrees of vibrational freedom corresponding to the $x$, $y$ and $z$ coordinate displacements for each atom. However in addition to vibrational motion, molecules also have translational and rotational motion which can be described by their own set of coordinates. The overall consequence of these transitions to the intermolecular potential is zero and their effect may be neglected Thus, the number of normal modes is equal to the number of internal degrees of vibrational freedom. Non-linear molecules have $3N$-6 and linear molecules have $3N$-5 degrees of vibrational freedom.

The degrees of freedom for two different molecules is illustrated in Figure 1:5. In the linear triatomic molecule $CO_2$ there are 4 degrees of vibrational freedom. The 4 normal modes consist of two stretching vibrations and two bending motions as shown in Figure 1:5A. The two bending vibrations have the same frequency because the vibrations occur in mutually exclusive planes. Vibrations of this type are called doubly degenerate and exhibit a single vibrational frequency. Similarly, the symmetric stretching vibration is not active in the infrared. $CO_2$ is symmetrical in its equilibrium state and does not have a dipole moment. As mentioned earlier, a change in dipole moment is required for the vibration to be observed in the infrared. The symmetrical stretching motion does not induce a dipole moment and therefore this vibration is not seen. It should also be noted that the stretching vibration has a higher frequency than the bending motions. This is usually true because a larger force is required to stretch a molecule rather than bend it.

In contrast, $H_2O$ is nonlinear triatomic molecule whose 3 normal modes are shown in Figure 1:5B. In this case there are no degenerate vibrations and all the modes are observed. In addition to the fundamental modes, there are harmonic overtones and combination bands observed in the IR spectrum. Combination bands represent the sum of two or more fundamental vibrations. However, the fundamental mode combinations are not precise and so the sums are not exact. Similarly, the vibration of one bond also involves the remainder of the molecule. This interaction results in overtones that are not strictly harmonic and therefore are not exact multiples of the fundamental mode. This effect is noted in Table 1:4 which gives the infrared bands of $H_2O$ vapor.

Another difference between the model and real molecules relates to the intensity or amplitude of the vibration. For a simple harmonic oscillation, there is no relationship between the frequency and the amplitude of the vibration. The frequency will be the same regardless of the magnitude of the displacement because of the proportionality of the restoring force (Hooke's law). This is true for both the model and any molecule as is evident in equation 1.4. However, in molecular systems the amplitude of the absorption of a vibration originates from the square of the transition moment and is not related to the intensity of a peak in the spectrum. This is in part a reflection of the rate of change of the dipole moment with respect to the displacement of the atoms as mentioned previously. For a vibrational transition to occur the transition moment needs to be non-zero. The non-zero value relates to the permissibility of the vibrational transition, which is dictated by the symmetry of the wavefunctions. The wavefunctions are derived from the quantum mechanical

approach using the Schrödinger equation. The symmetrical stretch of $CO_2$ is a good illustration of a symmetry-related, zero-transition moment. The geometry of $CO_2$ dictates that the symmetrical stretching mode has a zero-transition moment. On the molecular level, there is no seperation of charge in the molecules because the oxygen atoms move equally away from the carbon atom preventing the formation of a dipole as shown in Figure 1:5. Thus the transition moment defines whether a vibrational transition will occur and how intense it will appear. Molecules that have large permanent dipole moments such as those due to the carbonyl group will have very strong absorption bands while non-polar groups will tend to have weaker absorption bands.

The intensity of an absorption in an infrared spectra is directly related to the amount of material in the sample and not the magnitude of the vibration. The probability that a photon of light is absorbed by a molecule is directly proportional to the concentration of the absorbing material. This is known as the Lambert-Beer law and allows the quantitative analysis of absorption bands. Each molecule can be thought of as having a cross section, $k$ for photon capture. The probability that a photon is captured by a molecule is given by:

$$\frac{dI}{I} = -kcdx \tag{1.5}$$

where $I$ is the number of photons per unit area per unit time of a particular wavelength passing through a sample of thickness $dx$, concentration $c$, and emerging as the change in intensity $dI$. The proportionality constant $k$ depends on the wavelength of

the radiation. Integrating equation 1.8 between $I_0$ when x=0 and $I$ when x=$l$ where $l$ is the length of the sample:

$$\int_{I_0}^{I} \frac{dI}{I} = -kc \int_{0}^{l} dx$$

(1.5)

and converting the resultant to log to the base 10 gives the Lambert-Beer law the final form of:

$$\log \frac{I_0}{I} = A = \varepsilon c l$$

(1.6)

where the absorbance is obtained from the log ($I_0/I$), c is the molar concentration and $l$ is the pathlength in centimeters. The proportionality constant $\varepsilon$ is called the molar absorption coefficient and has units of liters mole $^{-1}$ cm$^{-1}$. When integrated over an absorption band, the absorption coefficient is proportional to the transition moment of the vibrating groups contributing to the band. Therefore the absorption coefficient is characteristic of the material being measured and dependent on the wavelength and sample conditions.

Equation 1.7 indicates that the absorbance of a sample is directly proportional to both the concentration and the pathlength of the sample. Accurate quantitative measurement of samples with unknown concentrations may be determined if any of the other three variables of equation 1.7 are known. However, there is one limitation to Lambert's law. As the concentrations of solutes become large, the direct proportionality is lost and the result becomes non-linear. Care must be taken not to

exceed this point in any type of analysis. Typically, concentrations greater than $10^{-3}$ molar should not be exceeded. The most accurate information can be collected if the concentration is maintained such that the absorbances fall between 0.01 and 1.0 absorbance unit. Since the pathlength and the concentration of absorbing groups in tissues are not known, we present the spectrum in arbitrary units along the intensity axis. As a result the ordinate of an absorbance spectrum is a rough measure of the concentration of the absorbing groups at that particular wavelength as given by the absorption coefficient.

In summary, quantum mechanical selection rules dictate whether or not a vibrational transition is allowed. The molecular geometry contributes to the selection rules and determines the intensity based on the magnitude of the change of the molecular dipole moment. Equation 1-4 provides us with the energy of a vibration in terms of the frequency of the normal mode. Therefore, we have the two pieces of an absorbance spectrum. The frequency is measured in wavenumbers and the intensity is given by absorbance. The real intensity of the sample is dictated by equation 1.7 and is a direct measure of the concentration of vibrating groups

Infrared spectroscopy is by no means limited to the study of small molecules. In fact there is an extensive literature on molecules of biological significance. This includes a wide range of proteins, nucleic acids in different forms, and lipids in membrane structures. In order to further understand the applications of infrared spectroscopy, the following discussion will briefly cover the relevant aspects of infrared spectroscopy of biological molecules.

The secondary and tertiary structure of a protein is based on the primary amino acids sequence of the protein. The amino acids are connected together by the peptide or amide linkage. The characteristic vibrations of the amide linkage have been studied extensively and are relatively well understood (Diem 1993; Jackson and Mantsch 1995). The frequency and origin of the relevant amide vibrations are shown in Table 1:5. Many of the experiments that allowed assignment were performed in isotopically substituted aqueous solution. Deuterium oxide solutions have several advantages over aqueous solution. Standard aqueous solutions pose a problem because they exhibit a large absorbance in the amide region of the spectrum due to the water deformation mode (see Table 1:4).

Subsequent to the characterization of the amide vibrations, it was discovered that the frequencies of some amide vibrations vary depending on the secondary structure of the peptide (Diem 1993; Jackson and Mantsch 1995). In proteins each amide linkage participates in some form of secondary structure. The structure may be as well defined as a helix or may be as disorganized as an unordered region of the protein. Each of these structural motifs requires a specific set of hydrogen bonds in order to maintain the integrity of the structural motif. The hydrogen bond interactions include both the C=O and C-N portions of the amide linkage and thus effect the amide I vibration to the greatest extent. Therefore, it is not surprising that the frequencies of the amide I will change depending on secondary structure. The amide II and III modes are also influenced by secondary structure but other conditions make their interpretation less straightforward.

The reason for the frequency shift in the amide bands is dipolar coupling of the strong dipole transition moments among the geometrically fixed carbonyl groups (Diem 1993). A similar effect occurs in electronic spectroscopy and is known as the exciton effect. The coupling lifts the degeneracy of the nearly identical carbonyl vibrations and mixes them into excited states. Depending on the geometry, one or more of the excited states may become the predominate absorption in the overall normal mode absorption band. The result is different absorption frequencies for the amide I vibration depending on the geometry of the peptide linkage. Since the geometry of the different secondary structures is relatively fixed, the frequency shifts are highly reproducible. Table 1:6 shows the variation in amide I frequency as a function of secondary structure.

The same effect may also occur for the side groups of some amino acids resulting in very complex absorption spectra for a peptide. Of course, it should be kept in mind that the frequency determinations were made with small peptides. For a real protein the situation is much more complex. All proteins contain more than one secondary structural motif that can give rise to more than one amide absorption. The exact nature of the secondary structure is dependent on the side chains, solvent conditions and whether the measurements are made in solution or solid state. Even when these conditions are well controlled the main bands are often broad and featureless because of weak seperation and overlap of the component bands (Diem 1993; Jackson and Mantsch 1995). In these situations, mathematical treatment of the absorption bands such as deconvolution can resolve the band into its main

components. However this procedure has many pitfalls and must be performed with extreme care (Jackson, Choo et al. 1995).

In nucleic acids, the base moieties have carbonyl groups, which can also be used to probe molecular secondary structure (Diem 1993). As in the amide vibrations, the carbonyl groups of nucleic acids are involved in hydrogen bonding between the respective strands of the double helix. The carbonyl groups are arranged in fixed geometry and interact by a dipolar coupling mechanism as in the amide I vibrations resulting in conformational sensitivity and a strong vibration at 1650 $cm^{-1}$. In addition to the strong carbonyl vibrations there are other base, sugar and backbone vibrations that contribute to the complexity of nucleic acid spectra. Of these, the phosphodiester vibrations are the most significant. The phosphodiester linkage contains both a symmetric and asymmetric P-O vibration. They are relatively intense bands with the symmetric stretching mode appearing at 1100 $cm^{-1}$ and the asymmetric stretching vibration occurring at 1250 $cm^{-1}$.

Phospholipids in lipid bilayers also contain phosphodiester links between their headgroups and the glycerol moiety that exhibit frequencies similar to the symmetric and asymmetric phosphate vibrations of nucleic acids. The ester links of the fatty acids to the glycerol backbone also provide spectral information based on the carbonyl group. Both of these can be used to monitor the conformation of the headgroup domain of phospholipids in model membranes (Diem 1993). In addition the hydrocarbon chains of the fatty acid groups provide a wealth of conformational information. It was found that the C-H stretching vibrations were extremely sensitive

to the gel-liquid crystal phase transitions. The effects were found in the *ca* 2800 to 3000 $cm^{-1}$ range.

One of the main reasons for the recent advances in the understanding of biological molecules is the development of Fourier transform instrumentation. The interferometric method offers several advantages over traditional dispersive infrared systems. Coupling of Fourier transform spectrometers with compact personal computers has made owning and operating an instrument relatively inexpensive. The speed at which these instruments operate has allowed the rapid and accurate collection of spectral information and has lead to a proliferation of their use.

In dispersive infrared spectrophotometers, a monochromator is used to separate polychromatic light into its corresponding monochromatic components. This is achieved by a diffraction grating according to Bragg's equation. This method is relatively inefficient because only one wavelength is selected at a time and the remaining power is lost in the instrument. Dispersive systems are also slow since the grating requires time to scan the entire wavelength range. In a Fourier transform spectrophotometer, infrared radiation is analyzed by means of a scanning Michelson interferometer. With this method, radiation from the source is collimated by a mirror and the resultant is divided by a beamsplitter. Half the radiation passes to a fixed mirror and half is passed to a moving mirror. The light impinging on the fixed mirror is immediately reflected back to the beamsplitter. The light impinging on the movable mirror is also reflected back but with a phase shift such that for any particular wavelength the light will interfere constructively or destructively when it recombines at

the beamsplitter. Whether the interference is constructive or destructive depends on the path length difference between the two mirrors. When a constant mirror velocity is used, the intensity of the emerging radiation is modulated in a regular sinusoidal wave for a particular wavelength. With polychromatic light the emerging radiation is a complex mixture of sinusoidal frequencies. Both the sampling rate and the mirror velocity are controlled by the use of a helium-neon laser as a reference beam. After passing through the sample the signal reaching the detector is a set of superimposable waves that contains all the information of the spectral range and is called an interferogram.

In order to reconstruct the spectrum, the data must be converted from the interferogram or time domain into the frequency domain. This is achieved by the mathematical process called a Fourier transform. The calculation is based on the Fourier pair, which allows inter-conversion between the time and frequency domains. The interferogram and spectral intensity are related by the Fourier pair:

$$P_{(x)} = \int_{-\infty}^{\infty} P_{(\tilde{\nu})} \cos(2\pi x\tilde{\nu}) d\nu$$

(1.7)

$$P_{(\tilde{\nu})} = \int_{-\infty}^{\infty} P_{(x)} \cos(2\pi x\tilde{\nu}) dx$$

(1.8)

where $P_{(x)}$ is the intensity of the light at the detector, $P_{(\tilde{\nu})}$ is the intensity of the light at the corresponding frequency ($cm^{-1}$) and $x$ is the displacement of the mirror ($cm^{-1}$). The integration is over all frequencies of light reaching the detector from the entire

mirror travel distance. To obtain the spectrum one takes the Fourier transform of equation 1.9. The result is a standard frequency spectrum of the material being studied. The calculation is carried out on a computer or a dedicated fast Fourier transform processor, which makes the time required to transform the data brief (few seconds to a few microseconds, respectively). The individual interferograms are acquired rapidly as well, with the mirror speed being the limiting factor.

The Fourier technique offers several distinct advantages to conventional dispersive methods. The only moving part is the mirror mounted on a near frictionless air bearing. The use of a laser as a reference results in a frequency accuracy of *ca* 0 01 $cm^{-1}$ even with any instability in the mirror movement. This degree of accuracy is far better than in dispersive instruments and allows accurate alignment of multiple scans Thus, repetitive scanning is possible with accurate co-addition of data. Energy wasting slits are not required, allowing a larger angle of incident radiation to fall on the sample. This is known as Jacquinot's advantage. The result is a greater throughput of energy to the sample. The most powerful reason for doing infrared spectroscopy via interferometric methods is known as Felgett's advantage. The advantage arises because all wavelengths are simultaneously detected throughout the scan. In this way, interferometric methods achieve the same signal to noise ratio as dispersive instruments in a fraction of the time. This accounts for the enormous speed at which data can be collected.

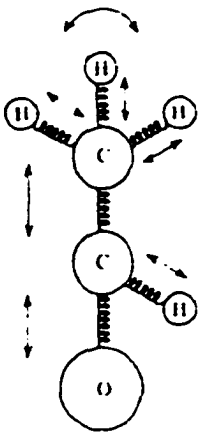

Figure 1:3 Ball and spring model of acetaldehyde. Arrows indicate some of the more prominent vibrations that the spheres may experience.

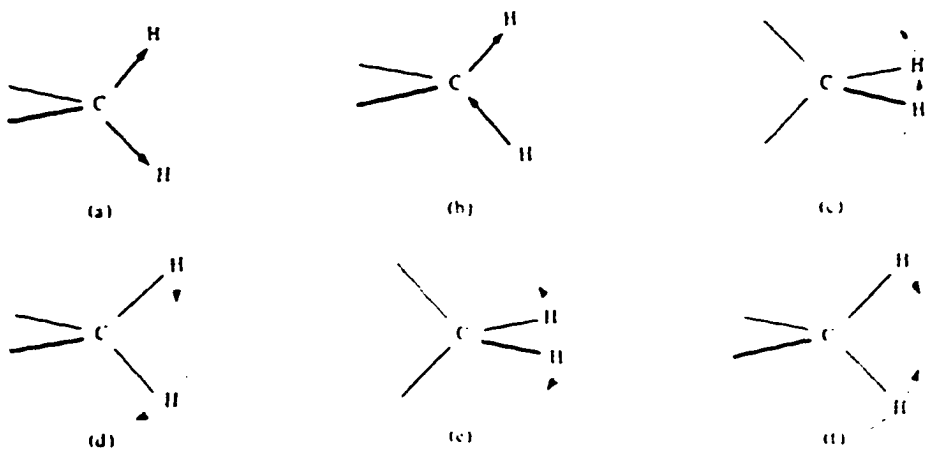

Figure 1:4 Illustration of the stretching and bending vibrational modes for a methylene group. A, symmetric stretching. B, asymmetric stretching. C, wagging out of plane deformation. D, rocking in plane deformation. E, twisting out of plane deformation. F, scissoring in plane deformation.

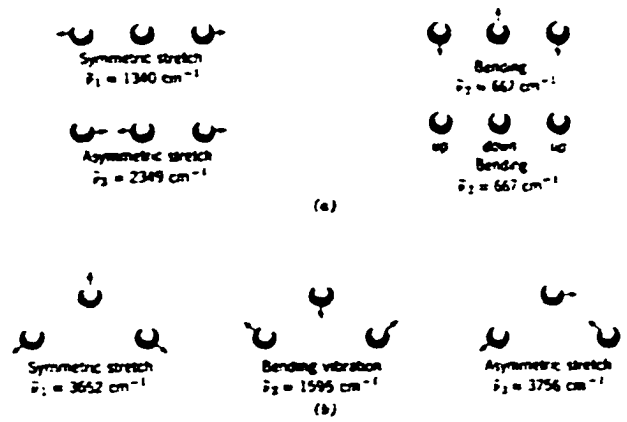

Figure 1:5 Normal modes of vibration. A, The four normal modes for the symmetrical linear $CO_2$ molecule. B, Three normal modes for the asymmetric non-linear $H_2O$ molecule. The frequencies of each vibration are shown beneath the mode along with their vibrational quantum number.

Table 1:4 Frequency and interpretation of $H_2O$ vapor infrared bands. Normal modes, combination bands and overtones are calculated from figure 1:5B.

| $\tilde{\nu}$ *(cm-1)* | *Interpretation* |
|---|---|
| 1595 | $\tilde{\nu}_2$ |
| 3151 | $2\tilde{\nu}_2$ |
| 3651 | $\tilde{\nu}_1$ |
| 3755 | $\tilde{\nu}_3$ |
| 5332 | $\tilde{\nu}_2+\tilde{\nu}_3$ |
| 6874 | $2\tilde{\nu}_2+\tilde{\nu}_3$ |

Table 1:5 Frequency and assignment of some of the amide linkage vibrations.

| Name | Frequency ($CM^{-1}$) | Assignment |
|---|---|---|
| Amide I | 1630-1700 | C=O stretch, with contributions from C-N and C-N-H |
| Amide II | 1510-1570 | N-H deformation |
| Amide III | 1230-1330 | N-H, C-H deformation |

Table 1:6 Amide I frequencies for selected secondary structure.

| *Secondary Structure* | *Amide I frequency ($cm^{-1}$)* |
|---|---|
| Anti-parallel β-sheet | 1675-1695 |
| $3_{10}$-Helix | 1660-1670 |
| α-Helix | 1648-1660 |
| Unordered | 1640-1648 |
| β-Sheet | 1625-1640 |
| Aggregated strands | 1610-1628 |

# Chapter 2 : Materials And Methods

## 2.1 Tissue Sample Preparation And Histology:

All samples examined originated from paraffin embedded cervical cone or punch biopsies surgically collected by the department of obstetrics and gynecology at Lutheran Medical Center (Brooklyn, New York). Tissue processing and routine histology were performed by the department of pathology at Lutheran Medical Center Diagnostic evaluation of samples was performed from routine hematoxylin and eosin (H&E) stained tissue sections prepared in the histology laboratory. Cases for FT-IRM evaluation were selected after the final diagnosis was determined.

Site directed colposcopic punch biopsy was performed during colposcopic examination of the cervix. This procedure was carried out when Papinaclou stained cervical smears were suspected of having a lesion or when a diagnosis of atypical cells was delivered. If a lesion was or was not visualized by colposcopy, a small piece or multiple pieces were clipped from, or adjacent to, the external OS. Single or multiple fragments were generated by this procedure which were as large as 5 millimeters or less than 1 millimeter in greatest dimension. The fragments were placed in 10% neutral buffered formalin for fixation.

Conization was performed to remove a conical shaped specimen that typically includes the lesion, the transformation zone and a portion of the endocervical canal The sample was marked with a suture at the 12 O'clock position to indicate anatomical orientation. The shape of the cone has its base toward the portio vaginalis and the point toward the endocervical canal. Typically the shape (depth and width of base) of the cone depended on the location of the transformation zone.

Upon removal, the specimen was opened longitudinally along the 12 O'clock position and laid flat as indicated in Figure 2:1. The entire cone was sectioned by hand by making parallel longitudinal cuts 2 to 3 millimeters apart starting at the 12 O'clock position and moving clockwise. In this way each gross section contains a representative area of epithelium including the squamocolumnar junction. Each section was placed into a plastic perforated tissue cassette. The entire sample with each section in its respective cassette was placed in 10% neutral buffered formalin.

Tissue samples were processed in a VIP 2000 tissue processor according to the program shown in Table 2:1. The process was controlled by a microprocessor that takes the samples from fixative through a series of alcohols of increasing concentration so that the tissue was dehydrated. A clearing agent was used to remove the alcohol and the tissue was subsequently impregnated with paraffin wax. The program maintained vacuum and temperature of the solvents in the retort to allow a more rapid processing procedure. All samples were kept in 10% neutral buffered formalin from the time of removal until the commencement of processing.

Upon completion of tissue processing, the samples were ready for paraffin embedding. This was performed by taking the tissue out of the cassette and placing it in the bottom of a metal mold or form. If the tissue fragment was large enough, as was the case with cone biopsies, the epithelial surface was embedded perpendicular to the bottom of the mold. In this way a cross section of the epithelial surface was assured. This was not always possible with punch biopsies due to the dimensions of the sample. In these cases the fragments were oriented as close to vertical as possible. With the tissue held in place with a pair of forceps, the mold was filled with liquid paraffin. The mold was placed onto a chilled plate on which the temperature was maintained at approximately -20° C. The paraffin was allowed to solidify slowly over a period of several minutes.

Once the block hardened, the sample was ready to be sectioned on a standard rotary microtome. The block was initially "faced" by trimming away the excess paraffin so that the entire surface of the tissue was exposed. A section for H&E staining was collected at 4 microns thickness. The first H&E section was used for routine histopathological diagnosis and to determine the area to be measured by FT-IRM. The initial examination also served to determine how the tissue should be orientated onto the $BaF_2$ window so as to preserve the integrity of the epithelial surface to be studied. Since the cone biopsy sections were typically larger than the $BaF_2$ window, it was necessary to trim away any unwanted tissue so that the area to be examined could be centered onto the window. After the initial section was examined, the block was re-sectioned. The first section was collected at 4 microns for staining. The second section collected was cut at 6 microns and placed onto a

round 19 millimeter diameter $BaF_2$ window. A third section was obtained at 4 microns for an additional H&E stain. It was critical that the sections were cut without any artifact. Compression, wrinkling, or tearing as well as venetian blind and knife marks produce artifacts, which made visual interpretation difficult. Therefore extreme care was taken during sectioning to obtain smooth, defect-free sections. Likewise, when collecting the section on a $BaF_2$ window, care was taken not to stretch, wrinkle or trap air underneath the tissue section.

H&E staining of paraffin sections was carried out by standard protocol (Sheehan 1980). The procedure for routine H&E staining is shown in Table 2.2. Briefly, the section was deparaffinized and re-hydrated to distilled water. The section was then stained with hematoxylin (Harris's formula: 0.5% hematoxylin (w/v), 5% absolute ethanol (v/v), 10% potassium alum (w/v) in aqueous solution) for 5 minutes. The hematoxylin was differentiated with acid alcohol, and intensified with ammonia solution. The section was then counterstained with eosin (3% eosin Y (w/v) in 70% ethanol solution). The section was dehydrated, cleared and mounted with a synthetic resin.

Periodic acid-Schiff (PAS) staining was performed according to the AFIP modification of McManu's procedure (Sheehan 1980). In short, the section was deparaffinized and hydrated to distilled water. The section was oxidized in periodic acid (0.5% periodic acid (w/v) in aqueous solution) for 5 minutes at room temperature. The section was rinsed in distilled water to remove any excess periodic acid. The section was then placed in Schiff reagent (1% basic fuchsin (w/v), 2%

potassium metabisulfite (w/v), 5% 1N hydrochloric acid in aqueous solution) for 15 minutes at room temperature. The section is then rinsed in lukewarm distilled water for 10 minutes. The section was subsequently counterstained with Mayer's hematoxylin (0.1% hematoxylin, 0.02% sodium iodate, 0.5% potassium alum, 0.1% citric acid, 0.5% chloral hydrate (w/v) in aqueous solution) for 5 minutes. The section was then rinsed briefly in distilled water, dehydrated, cleared and mounted with a synthetic media. The presence of endocervical glands was used as positive control the PAS reaction.

Samples treated with diastase digestion were deparaffinized and re-hydrated as above. The section was exposed to diastase (0.1% (w/v) malt diastase in aqueous solution preheated to 37° C) and then incubated for 1 hour at 37° C. The section was then washed in running tap water for 10 minutes. The sections was then stained with the PAS method described above.

Before the tissue sample could be examined by FT-IRM, it was necessary to deparaffinize and rehydrate the section. This process is analogous to the first 7 steps of Table 2:2 and the reverse of the procedure in Table 2:1. If the paraffin was not removed, the combined refractive index of the tissue and paraffin made target visualization and acquisition difficult. Therefore, all $BaF_2$ window/tissue sections were subjected to a standardized deparaffinization procedure. After sectioning, the window was allowed to dry completely. The window was incubated at 60° centigrade for 1 hour to remove excess paraffin from the window. Subsequently, the section was deparaffinized by passing the window through a series of 3 xylene baths for 5 minutes

each. Re-hydration was initiated with 3 baths of 100% ethanol for 3 minutes each. Hydration was completed by proceeding into 2 baths of 95% ethanol for 3 minutes followed by repeated washings in distilled water. Pooling of water on the $BaF_2$ window tended to etch the surface of the window, so water was completely removed. At this point the sample was ready for FT-IRM analysis.

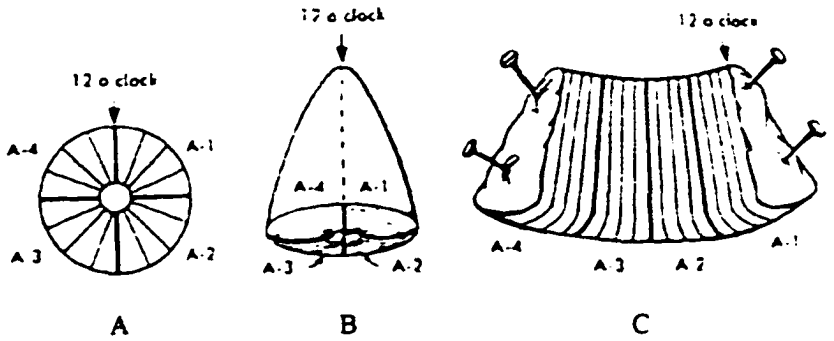


Figure 2:1 Gross dissection of a cervical cone biopsy. A, Front view of cone biopsy illustrating the 4 quadrant dissection approach. B, Top view showing the longitudinal incision starting at the portio vaginalis and moving toward the endocervix from the 12 O'clock suture. C, Opened cone biopsy. The cone is not bisected but opened along the anterior portion. Note how each section may be located relative to the 12O'clock position. The number of sections is limited only by the dimensions of the cone (adapted from Akerman's Surgical Pathology 1989).

Table 2:1 Routine H&E staining procedure for tissue sections.

| *Reagent* | *Time* |
|---|---|
| Clearing Reagent | 2 Minutes |
| Clearing Reagent | 10 Dips |
| 100% Reagent Alcohol | 10 Dips |
| 100% Reagent Alcohol | 10 Dips |
| 95% Reagent Alcohol | 10 Dips |
| 95% Reagent Alcohol | 10 Dips |
| Tap Water | Rinse Gently |
| Harris Hematoxylin | 5 Minutes |
| Acid Alcohol (1% HCL in 70 % Alcohol) | 4 Dips |
| Tap Water | Rinse Gently |
| Ammonia Water (200 µl 28% Ammonia to 400 ml Distilled Water) | 5 Dips |
| Tap Water | Rinse Gently |
| 95% Reagent Alcohol | 10 Dips |
| 1% Alcoholic Eosin | 30 Seconds |
| 95% Reagent Alcohol | 10 Dips |
| 95% Reagent Alcohol | 10 Dips |
| 100% Reagent Alcohol | 10 Dips |
| 100% Reagent Alcohol | 10 Dips |
| Clearing Reagent | 10 Dips |
| Clearing Reagent | 10 Dips |
| Clearing Reagent | 5 Minutes |

Table 2:2 Tissue processing schedule. Each station has a designated reagent that is pumped into and out of the retort chamber. Exposure time, temperature and pressure/vacuum parameters are as indicated.

| *Station* | *Reagent* | *Time* | *Temperature* | *Pressure/Vacuum* |
|---|---|---|---|---|
| 1 | Formalin | 1 Hour | 37° C | Yes |
| 2 | Formalin | 1 Hour | 37° C | Yes |
| 3 | 50% Formalin and 50% Reagent Ethanol | 1 Hour | 37° C | Yes |
| 4 | 95% Reagent Alcohol | 30 Minutes | 37°C | Yes |
| 5 | 95% Reagent Alcohol | 1 Hour | 37° C | Yes |
| 6 | 100% Reagent Alcohol | 1 Hour | 37° C | Yes |
| 7 | 100% Reagent Alcohol | 1 Hour | 37° C | Yes |
| 8 | Clearing Reagent | 30 Minutes | 37° C | Yes |
| 9 | Clearing Reagent | 1 Hour | 37° C | Yes |
| 10 | Clearing Reagent | 1 Hour | 37° C | Yes |
| 11 | Paraffin | 30 Minutes | 57 ° C | Yes |
| 12 | Paraffin | 1 Hour | 57° C | Yes |
| 13 | Paraffin | 1 Hour | 57° C | Yes |
| 14 | Paraffin | 1 Hour | 57° C | Yes |

## 2.2 Fourier Transform Infrared Microspectroscopy:

Infrared data was acquired from an *i*-series Perkin-Elmer microscope accessory connected to a Perkin-Elmer Paragon 1000 FT-IR. The entire system was controlled by a Digital computer running Perkin-Elmer's own instrument and data manipulation software. A schematic of the optical system is shown in Figure 2:2. The microscope has two analytical operational modes. All data in this study were collected in transmission mode after visual inspection and alignment of the samples. Barium fluoride was used as the infrared substrate in this study because of its excellent properties. $BaF_2$ has a wide infrared transmitting window with a low frequency cut off of *ca* 870 $cm^{-1}$. This is well within the range of interest. $BaF_2$ is non-reactive and almost totally insoluble and could withstand the deparaffinization process that the tissue sections were subjected to. In addition, it has a low refractive index in the infrared and visible range which makes it ideal for both infrared and visible studies.

In brief, the optical paths for visible and infrared examination are as follows: The reference laser and infrared source beams were transferred via the transfer optics in the spectrophotometer to the microscope accessory. A flat mirror reflected the radiation to a torriod mirror. The torroid mirror reflected the radiation to the bottom mirror (T path in Figure 2:2) which reflected the light to the condenser cassegrain. The condenser cassegrain focused the radiation onto the sample. The sample image was collected by the view/IR cassegrain. An adjustable square aperture was inserted

into the optical path at this point as shown in Figure 2.2. The aperture dimensions were determined by the sample and were measured with a stage micrometer. The light passing through the aperture was reflected off the view/IR mirror and collected by the detector cassegrain. The detector cassegrain refocused the image onto a mid-range mercury-cadmium-telluride (MCT) detector that was cooled by liquid nitrogen. The cassegrain optics gave a final image magnification of 6X in infrared mode.

In light microscope mode, the view/IR mirror was moved out of the optical pathway so the sample could be inspected visually. This automatically turned on a 35 watt variable intensity illuminator that was coaxial with the infrared light path. The visual optical components consisted of 15X oculars with a 2.8X objective giving a 40X final magnification. A single $BaF_2$ window with the tissue section mounted on one side was loaded onto an automated stage that allowed precise manipulation of the sample in the standard X, Y directions.

In order to analyze a sample, it was necessary to find a physical landmark on the $BaF_2$ tissue section that could be seen on an H&E stained section. The tissue section on the $BaF_2$ window did not contain any biochemical dyes, so the features were detected by differences in visual optical density. As a result, only prominent features could be resolved visually in the infrared microscope. For this reason it was extremely important that an H&E section be obtained immediately following the window section. Adjacent sections had the least amount of anatomical deviation, and features could be closely compared. When the differences were greater than several microns, it became extremely difficult to match locations on the window and slide.

The H&E comparison section was viewed on a standard optical microscope with 4, 10 and 40X objectives. After an anatomical landmark was distinguished, a determination was made as to how close the two areas matched in architecture and histology. Once the exact location of the area was determined, the area to be measured was selected and a spectrum could be acquired. The exact anatomical area was known from the H&E section and a direct correlation with the pathology could be made. Subsequently the size of the square aperture was matched to the area to be measured. The exact size of the aperture varied depending on the anatomical location from which a measurement was to be made. Typically the aperture gate was rectangular and measured between 100 x 15 microns to 100 x 75 microns Tissues outside the opening in the aperture were not incorporated into the measurement. The aperture was not transparent in the infrared and as such radiation is blocked from reaching the detector when the aperture is in place. When the aperture size was set, a background spectrum could be collected from an area devoid of tissue.

When focusing the sample in light microscope mode, changes in the position of the stage (sample) relative to the condenser cassegrain, altered the throughput of infrared radiation to the detector. To correct for this, the energy reaching the detector was maximized using manual correction that adjusted the sub-stage cassegrain condenser. Likewise the sample was centered in the optical field to maximize the amount of infrared energy reaching the sample. In addition, it was important to maintain the aperture at the same size as that used for the background when making subsequent measurements. If this was not done, background

subtraction errors would occur in the resulting spectrum. Thus a new background spectrum was collected when the aperture size was changed.

Representative samples of protein, DNA, and glycogen were collected using standard infrared techniques. Samples were prepared by dissolving a representative amount of material in water. A small amount was applied to a $BaF_2$ window and allowed to dry into a film. This was placed in a standard infrared cell and measured directly by the FTIR. Scan and data collection parameters are described below.

Data collection parameters were standardized as follows: 128 scans were collected and co-added for each data acquisition. In each sample there are at least 2 sets of measurements collected. Each set contains measurements from all four histologic layers. The measured spectral range was between 1800 and 700 $cm^{-1}$. The instrument was set to a 2 $cm^{-1}$ resolution and a data collection interval of 1 $cm^{-1}$. A static instrument gain of 2 was used for most measurements unless the area to be measured was extremely small. In these cases the gain was increased to an instrumental maximum of 8. A strong Beer-Norton apodizing function was used in the data treatment to reduce truncation. Background subtraction was carried out by the Perkin-Elmer instrument software. The data was downloaded and further manipulated by software developed in the laboratory. Typically the data were smoothed using an odd point Savitsky-Golay function and then baseline corrected. Peak positions were obtained from second derivatives of the spectra. All spectra were normalized to the amide I peak for comparison.

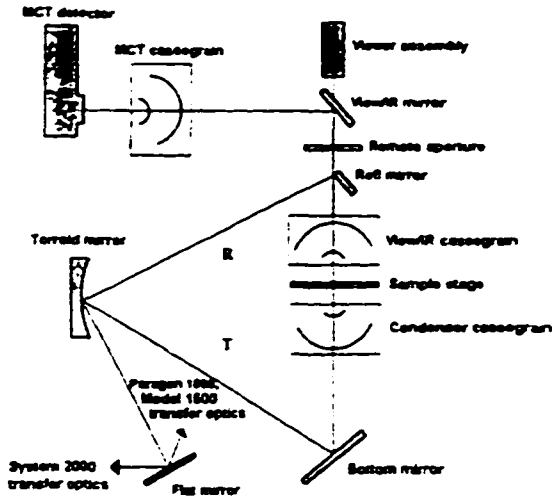


Figure 2:2 Optical schematic for the Perkin-Elmer *i* series infrared microscope. In transmission mode the radiation path follows the line marked T with the reflectance mirror out of the optical path. Likewise the view/IR mirror is moved out of the path in order to visualize the sample in light microscope mode. The infrared and visible light paths are coaxial, selecting the infrared mode automatically turns the visible source off (courtesy of Perkin-Elmer)

# Chapter 3 : Results

## 3.1 FT-IRM Of Non-Neoplastic Cervical Squamous Epithelium:

Figure 3:1 shows the infrared spectra of paraffin wax from 850 to 1800 $cm^{-1}$. Paraffin was not always removed completely during the deparaffinization procedure and varying amounts of residual paraffin were found in many spectra. Therefore the 1450 to 1470 $cm^{-1}$ region corresponding to $-CH_3$ antisymmetric deformation, the symmetric and antisymmetric $-CH_2$ deformation as well as the 1377 $cm^{-1}$ range belonging to the $-CH_3$ symmetric deformation, were disregarded in any comparison. For the same reason, the higher frequency region above 1800 $cm^{-1}$ was not utilized because of strong absorbance associated with the paraffin wax, in particular the methyl and methylene group vibrations found between 3000 and 2800 $cm^{-1}$. The negative peaks between 1500 and 1800 $cm^{-1}$ are due to the vibrational and rotational transitions of atmospheric water vapor.

Figure 3:2 is a photomicrograph of normal cervical epithelium obtained from a cone biopsy stained with H&E. The hematoxylin and eosin stain is the standard biochemical method used for all histopathological interpretation. All samples processed through a histology laboratory have at least one H&E section prepared. Hematoxylin is an aluminum mordant dye that "stains" the nucleus of all cells. This is believed to occur by the formation of dye complexes with the phosphodiester

backbone of DNA and the basic amino acids of the histones. As a result, only heterochromatin is visible with hematoxylin dyes. Eosin on the other hand, is a dye that predominately stains basic amino acids of proteins located in the cytoplasm. This is believed to occur when carboxylic and sulfonic acids of the dye combine with basic tissue constituents. Blue to purple nuclei and pink to orange cytoplasm are the end result of an H&E stain. Additional elements such as connective tissue fibers and red blood cells stain varying shades of pink depending on their composition. In Figure 3:2, the stroma can be seen to occupy approximately the lower half of the photomicrograph and is designated by the letters ST. A single layer of basal cells is seen traversing the Figure and is designated B. Immediately above this, is a thin layer of parabasal cells labeled P. The wide band of cells above the parabasal cells constitutes the intermediate cell layer and is designated I. At the very top is a layer of superficial cells designated by the letter S. There is no evidence of dysplasia in the biopsy shown in Figure 3:2. There is normal maturation and differentiation of the epithelium as indicated by the well defined cellular morphology and architectural organization. The basal layer is only one cell thick and there is no overcrowding. Similarly the parabasal, intermediate and superficial cells are well spaced and have lower nuclear to cytoplasmic ratios (N/C). The cell membranes are distinct and the nuclei have smooth regular features. Intercellular bridges are seen between cells in the lower levels. The chromatin pattern of the cells are homogenous and no chromatin clumping is observed in any of the layers. In the stroma, the elongated nuclei of fibroblasts are orientated parallel to the collagenous fibers which have their characteristic wavy appearance.

Figure 3:3 shows spectra collected between 850 and 1800 $cm^{-1}$ for the four different epithelial layers and stroma shown in Figure 3:2. The spectra were normalized to the amide I intensity. This allows comparison between spectra based on the relative total absorbance in the sample. This can be explained by applying Beer's law since we do not know the pathlength or concentration. Assuming a pathlength of 6 microns, a protein concentration within the cell of 0.1 molar, and a molar extinction coefficient of 1000 for a peptide group, the absorbance of a sample falls between $10^{-1}$ to $10^{-2}$ absorbance units. This crude calculation illustrates that the protein concentration of the cell is not high enough to absorb all the light and the absorption values are well within the range where good signal to noise ratios are obtained. However, different measurement windows and slightly different sample thickness' prohibit direct quantitative comparisons.

The region above 1400 $cm^{-1}$ is relatively the same in all five spectra. The two major bands at 1652 and 1536 arise from the amide I C=O stretching vibration and amide II N-H deformation respectively. The intensity ratio between the amide I band and amide II band (AI/AII) for the epithelial spectra are within 1% of one another. The stroma has a higher ratio by about 10%. The amide II band of the stroma is also broader and shifted to higher frequency.

The bulk of the differences in the spectra of normal cervical epithelium arise in the region between 900 and 1300 $cm^{-1}$. This is shown expanded in Figure 3:4. The most striking feature is the series of peaks observed between 1000 and 1200 $cm^{-1}$ for the superficial, intermediate and parabasal layers. The main peak is located at 1028

$cm^{-1}$ with two lower intensity bands found at 1080 and 1153 $cm^{-1}$. This band pattern is assigned to glycogen and identical to that observed for glycogen in solution (A: Chiriboga, Xie et al. 1997; B: Chiriboga, Xie et al. 1997; C: Chiriboga, Xie et al. 1997). The infrared spectra of hydrated glycogen is shown in Figure 3:5. The vibrations at 1028, 1080 and 1153 $cm^{-1}$originate from C-O-H deformation, C-C stretching and the C-O stretching of the sugar moieties respectively. In the tissue the amide III vibration originating from the combination of N-H and C-H deformations is also observed in the layers and is seen as a broad absorbance at 1235 $cm^{-1}$ with a small component at 1314 $cm^{-1}$. A similar amide III vibration can be seen in bovine serum albumin (BSA) used as a protein analogue and also shown in Figure 3:5. These features are altered in the basal layer and stroma spectra. The basal layer spectrum has a broad absorbance between 1000 and 1100 wavenumbers as does the stroma. However the basal layer has features that are more intense than the stroma in this range. In the basal layer the intensity ratios for the bands at 1031, 1060 and 1080 $cm^{-1}$ differ from the stroma. The 1031 and 1060 $cm^{-1}$ bands are elevated relative to the 1080 $cm^{-1}$ band. These band ratios are reduced in the stroma. These features do not appear to arise from the nucleus. Figure 3:5 also shows the spectra of DNA, which has characteristic vibrations at 965, 1065 and 1095 $cm^{-1}$. These correspond to the C-O stretching of the phosphodiester linkage, the C-O stretch of ribose and the symmetric phosphate stretch. The most striking feature of the stroma is the distinct amide III triplet. A large band located at 1235 $cm^{-1}$ with a low frequency shoulder at 1206 $cm^{-1}$ and a high frequency shoulder at 1280 $cm^{-1}$ are characteristic for the stroma. In addition, the stroma has a band located at 1335 $cm^{-1}$ originating from the $CH_2$

wagging vibration relatively absent in the epithelium. The basal layer has amide III vibrations that more closely resembles the epithelial layers. However, the ratio of the 1314 $cm^{-1}$ and amide III band is opposite of that found in the upper layers. Under normal circumstances, the epithelial layers do not exhibit the distinct amide III features of stroma.

The presence of glycogen in the superficial, intermediate and parabasal cell layers is consistent with morphological and anatomical evidence from tissue. Figure 3:6 shows a photomicrograph of the same area as in Figure 3:2 except the section is stained with PAS. There are many pathological processes that alter cellular glycogen concentrations. Thus, the PAS stain provides a reliable means for demonstrating carbohydrates in tissue sections for histologic evaluation. In short, the tissue sections are oxidized with periodic acid which results in the formation of aldehyde groupings through carbon-carbon bond cleavage. The aldehyde groups are reacted with a Schiff base which forms dialdehyde intermediates. The reduction is completed by the linkage of the intermediate to the Schiff base and oxidation of the adduct to the colored end product. The section is then washed profusely with water to minimize any non-specific staining. The reaction intensities vary depending on the origin of the carbon-carbon bonds cleaved in the primary oxidation. As a result, PAS stains a wide range of components including: polysaccharides, neutral mucosubstances, acidic mucosubstances structural fibers (including basement membranes), and occasionally protein. Proteins show a weak reaction due to N-linked and O-linked glycosylations. The photomicrograph in Figure 3:6 clearly shows that the superficial, intermediate and parabasal layers react strongly with PAS. The PAS stain produces a very intense

reddish-pink color in areas where the reaction has taken place. The most intense reaction is observed in the intermediate and superficial layers where glycogen synthesis and packing is ongoing. The parabasal layers show variable amounts of PAS staining depending on the maturity and location of the cells.

Figure 3:7 is a photomicrograph of diastase treated PAS stained cervical epithelium. Diastase acts on glycogen by hydrolyzing the α(1-4) glycosidic linkages between sugar residues and de-polymerizing the molecule. The smaller sugar residues are washed away during the proceeding water rinses. Non-hydrolyzable sugar moieties are not digested because they lack the branched glycogen structure as well as available α(1-4) linkages. Therefore areas that are PAS negative in the diastase treated section but PAS positive in the untreated section are derived from glycogen. The photomicrograph clearly shows that all the PAS stained areas in the different layers shown in Figure 3:6 are PAS negative. This indicated that the origin of the PAS positive reaction is a result of glycogen.

Figure 3:8 shows five spectra of the superficial layer measured from adjacent areas of the same sample. Not surprisingly, the superficial layer spectra show a high degree of similarity within the same sample. Intermediate and parabasal layer spectra also show a high degree of reproducibility from within the same sample as is shown in Figures 3:9 and 3:10. However, in the intermediate and parabasal layers, the measurement area is visually not as well defined as in the superficial layer (or as in the basal layer). In the superficial layer the aperture window is aligned with the lumen of the cervix which provides a visual reference point. The intermediate and parabasal

layers do not have this feature and anatomic overlap between the layers occurs during the measurement. Nevertheless, the spectra of the upper layers from the same sample are easily duplicated.

Basal layer spectra also shows a high degree of reproducibility within the same sample. Figure 3:11 shows five spectra from the basal layer taken from adjacent areas within the same sample. As with the superficial layer, the basal layer can be measured very accurately because one edge of the aperture window can be aligned with the stromo-epithelial junction. Proximal overlap of the stroma with the basal layer can be determined by the appearance of shoulders at 1206 and 1277 $cm^{-1}$ as well as the appearance of the 1335 $cm^{-1}$ band. These are the most readily distinguishable features of stroma and any spectra containing these bands can be disregarded as being contaminated by area overlap. Distal overlap with the parabasal layer can be seen as an increase in glycogen as is evident by the 1080 and 1153 $cm^{-1}$ bands becoming more prominent. Basal/parabasal overlap can be controlled more effectively than the other types of layer overlap. Since the basal layer is typically only one cell high, the aperture window may be set to these dimensions and aligned accurately with the stromo-epithelial junction as long as it remains linear.

In order to establish the spectral reproducibility of normal biopsy samples, multiple spectra of the superficial layer were collected from different biopsies. Figure 3:12 shows the spectra of the superficial layer from four biopsy samples with histopathological diagnoses of benign epithelium. The major differences between the spectra arise in the glycogen region. This can be seen as the change in the ratio

between the 1027 (G1) $cm^{-1}$ band and the amide I band. The variation in this ratio may be as large as 20-30%. However, the AI/II ratio remains relatively constant for all the samples indicating that the differences lie solely in the glycogen region. This is not surprising considering that the amount of glycogen in the epithelium is a function of hormonal status. Thus, individual variation is expected to be quite large. The same effect is seen in the intermediate and parabasal layers from different samples as is evident in Figure 3:13 and 3:14. Differences in these layers are compounded by the difficulties in defining the exact anatomical boundaries of the these regions. In contrast, the basal layer spectra of the same set of samples are very similar as seen in Figure 3:15. There are only small differences between the samples in the entire range. These differences arise from measurement error in the sizing of the aperture window around the basal layer.

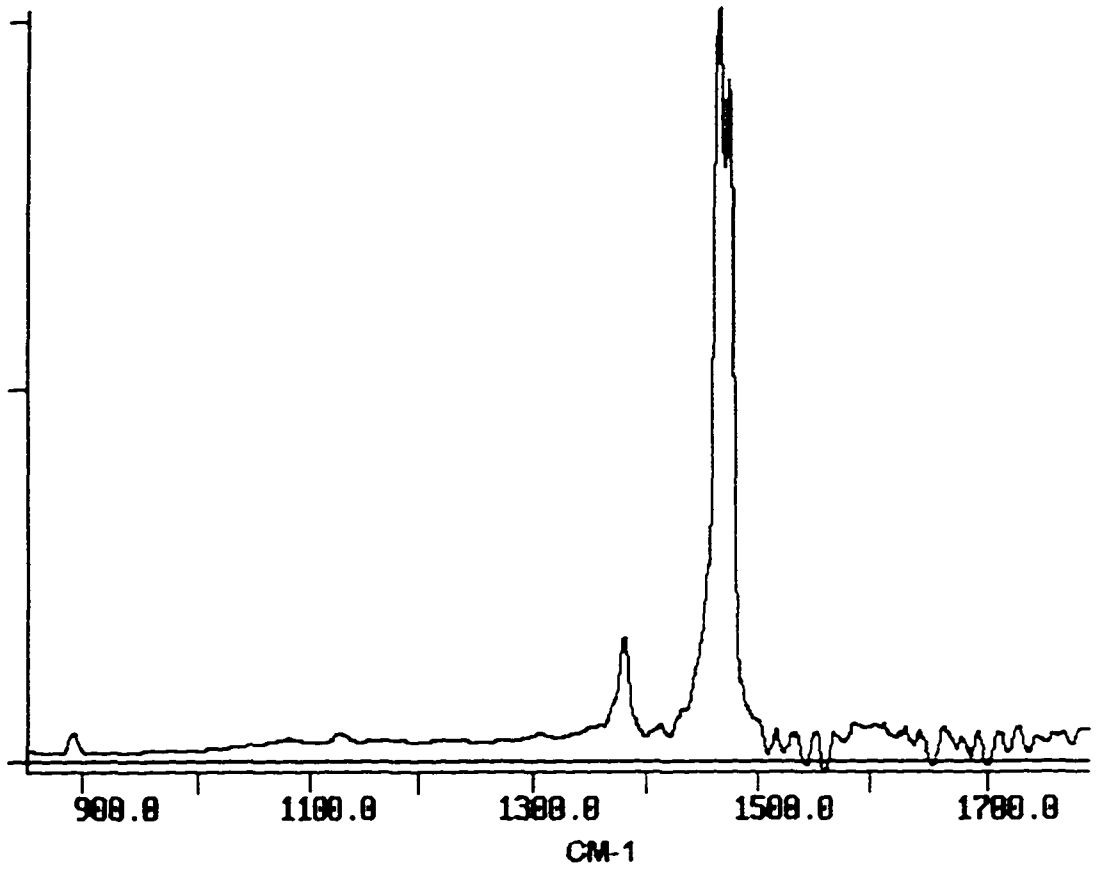


Figure 3:1 FT-IRM spectra between 850 and 1800 $cm^{-1}$ of the solidified paraffin wax used to infiltrate and embed cervical biopsy samples.

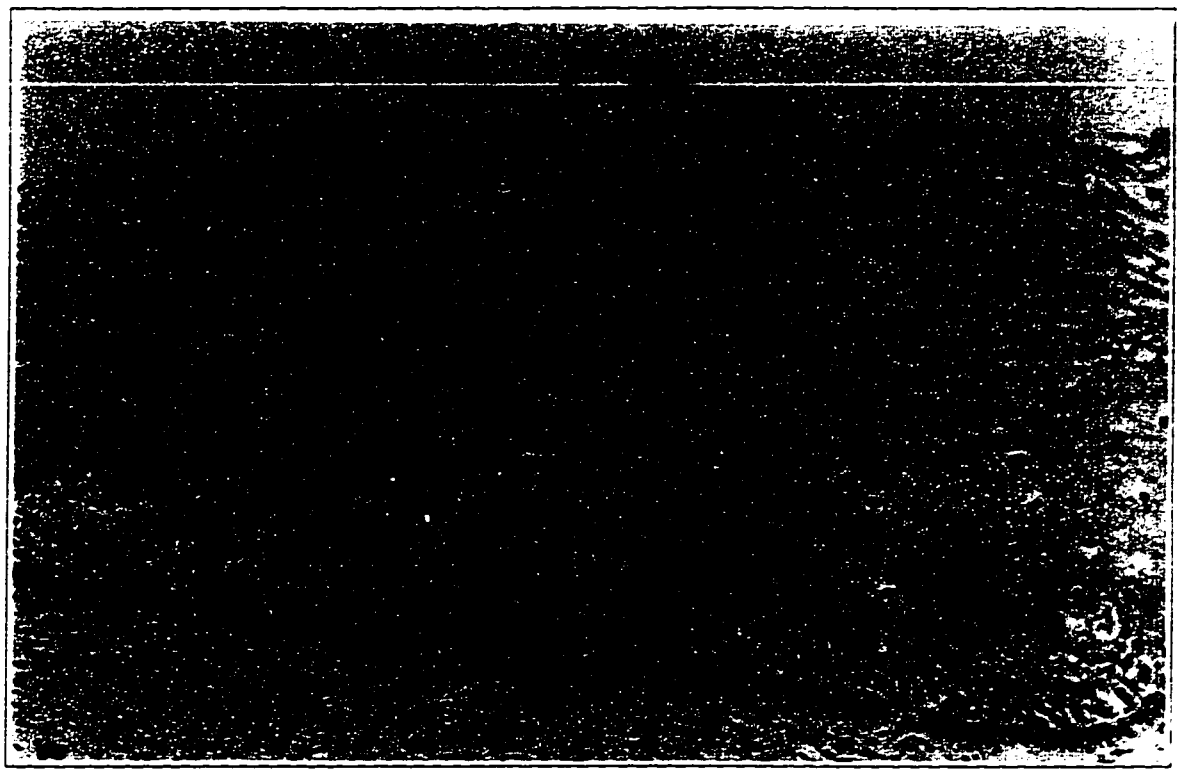

Figure 3.2 Photomicrograph of normal squamous cervical epithelium. Note the picket fence arrangement of the basal cell layer and organization of the upper layers. There are several stromal papillae which contain blood vessels projecting into the lower third of the epithelium. (ST= stroma, B= basal, P= parabasal, I= intermediate, S= superficial, 200X, H&E)

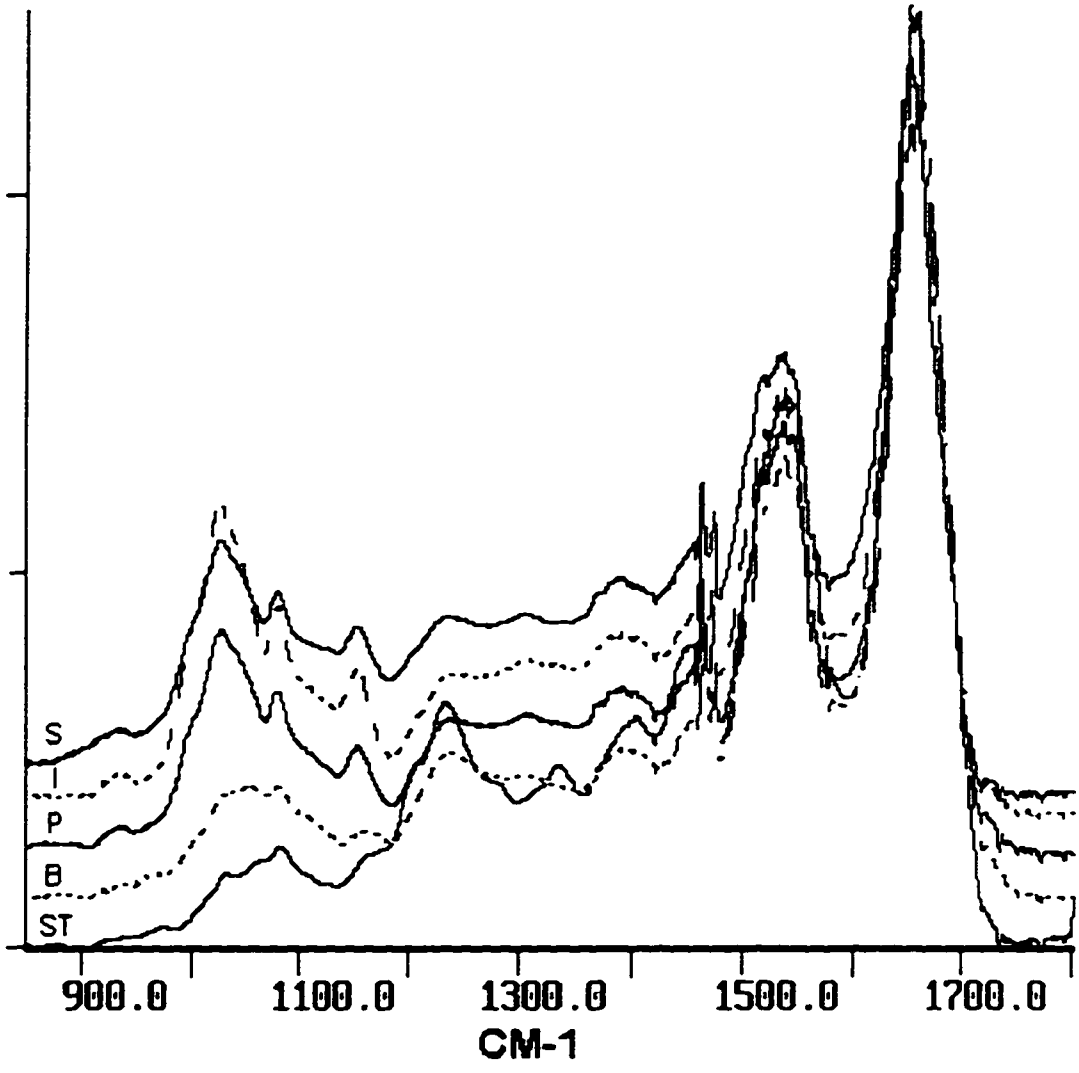


Figure 3.3 FT-IRM spectra between 850 and 1800 $cm^{-1}$ of the four epithelial layers and stroma shown in figure 3.2 ( ST= stroma, B= basal, P= parabasal, I= intermediate, S= superficial).

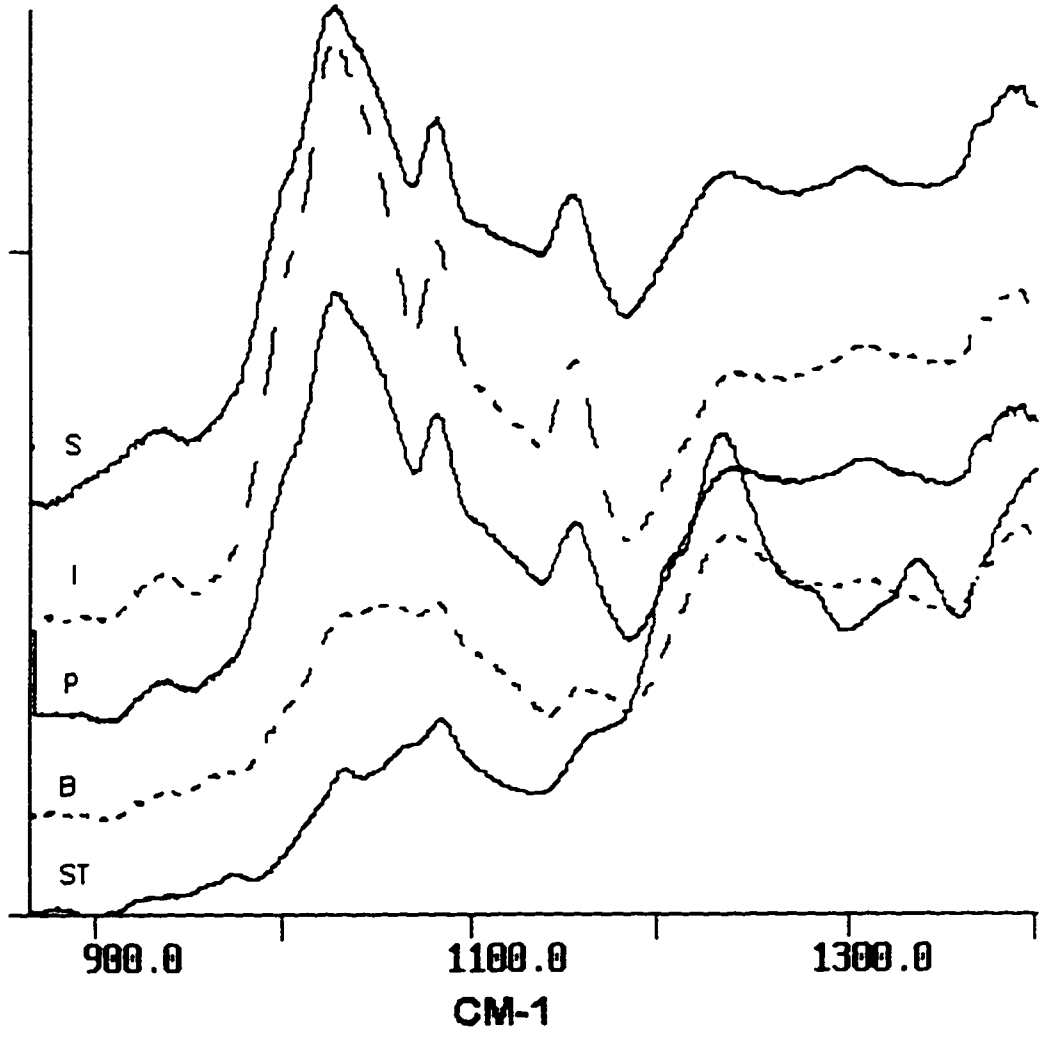


Figure 3:4 Expanded view between 850 and 1400 $cm^{-1}$ of the four epithelial layers and stroma. (ST= stroma, B= basal, P= parabasal, I= intermediate, S= superficial).

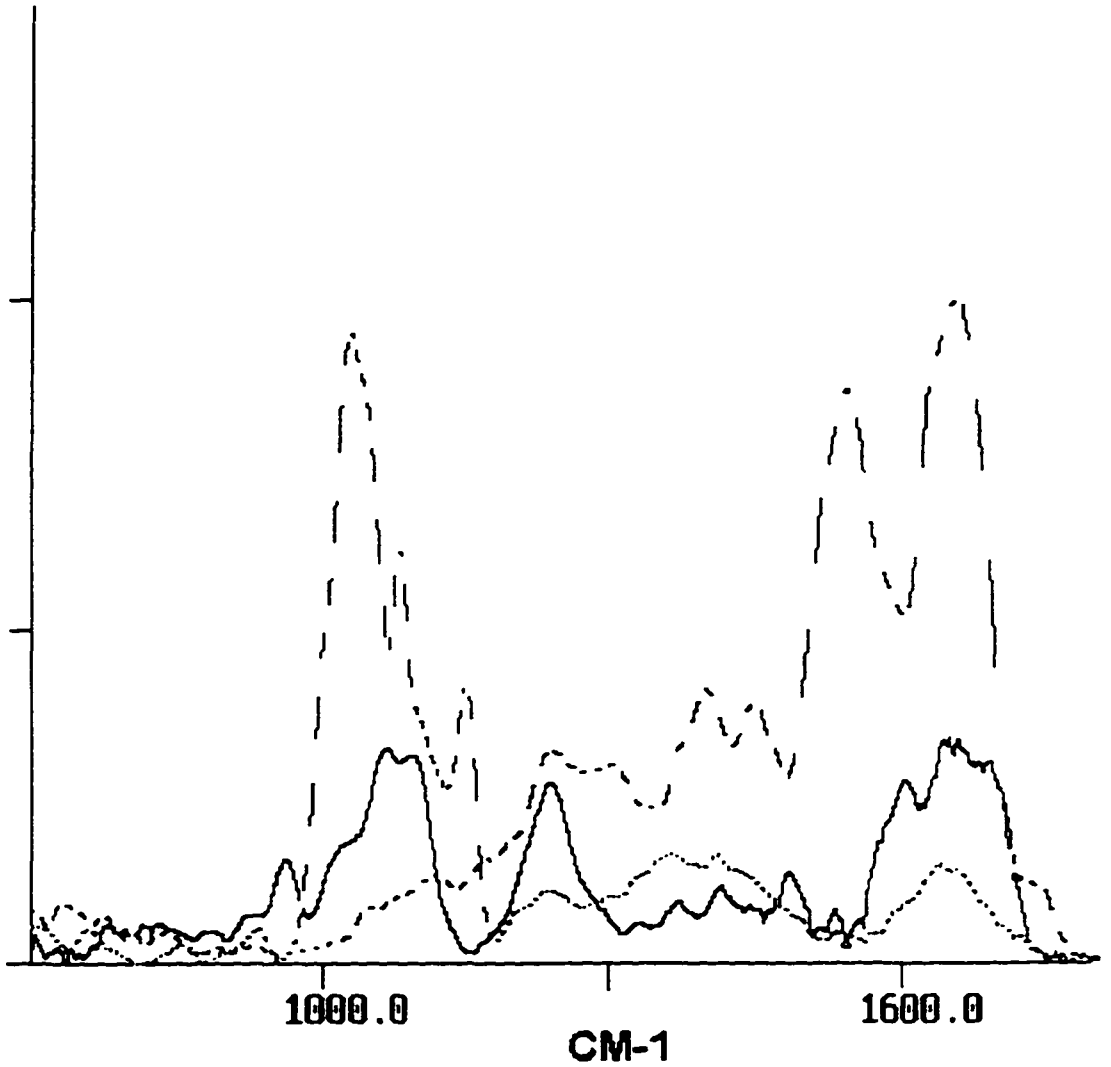


Figure 3:5 IR spectra between 850 and 1400 $cm^{-1}$ of bovine serum albumin (dashed), deoxyribonucleic acid (solid) and glycogen (dot). The spectra are not scaled so that fine details may be seen.

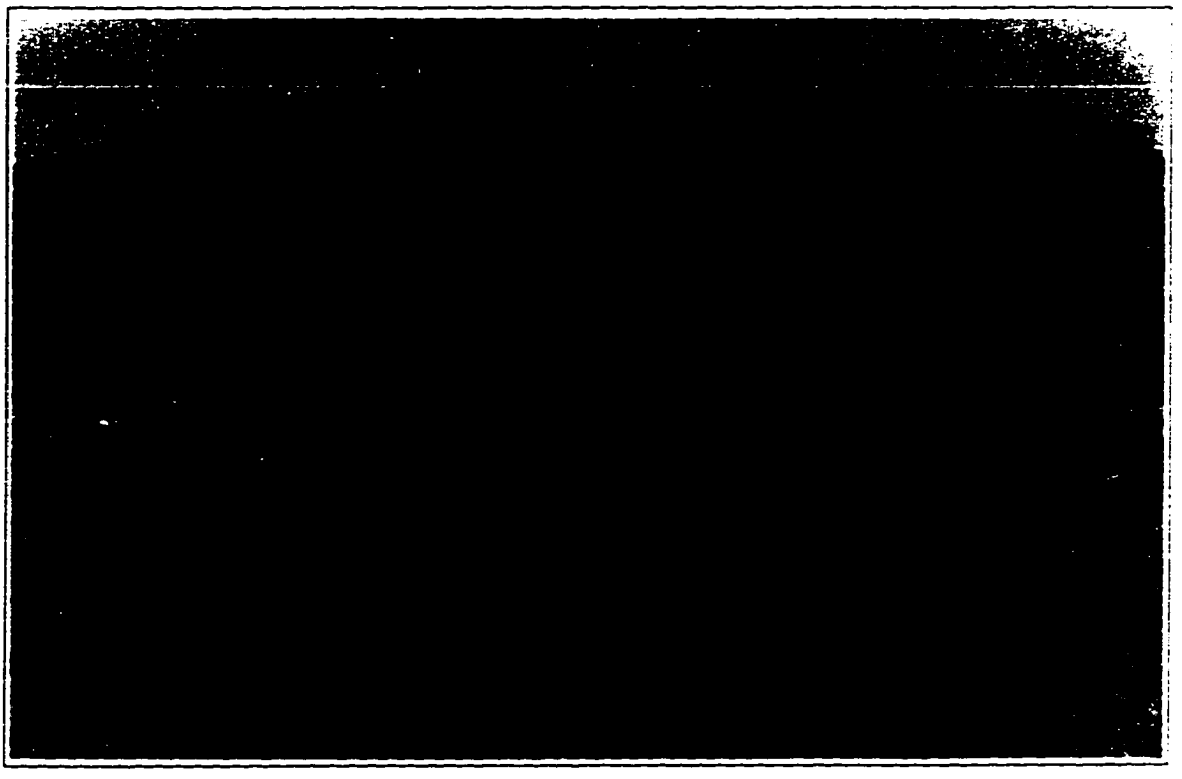

Figure 3:6 Photomicrograph of PAS reaction in non-neoplastic cervical epithelium demonstrating the presence of glycogen. Note the intensity of the intermediate layer reaction. Arrow indicates basement membrane exhibiting a positive PAS reaction See text for details (200X).

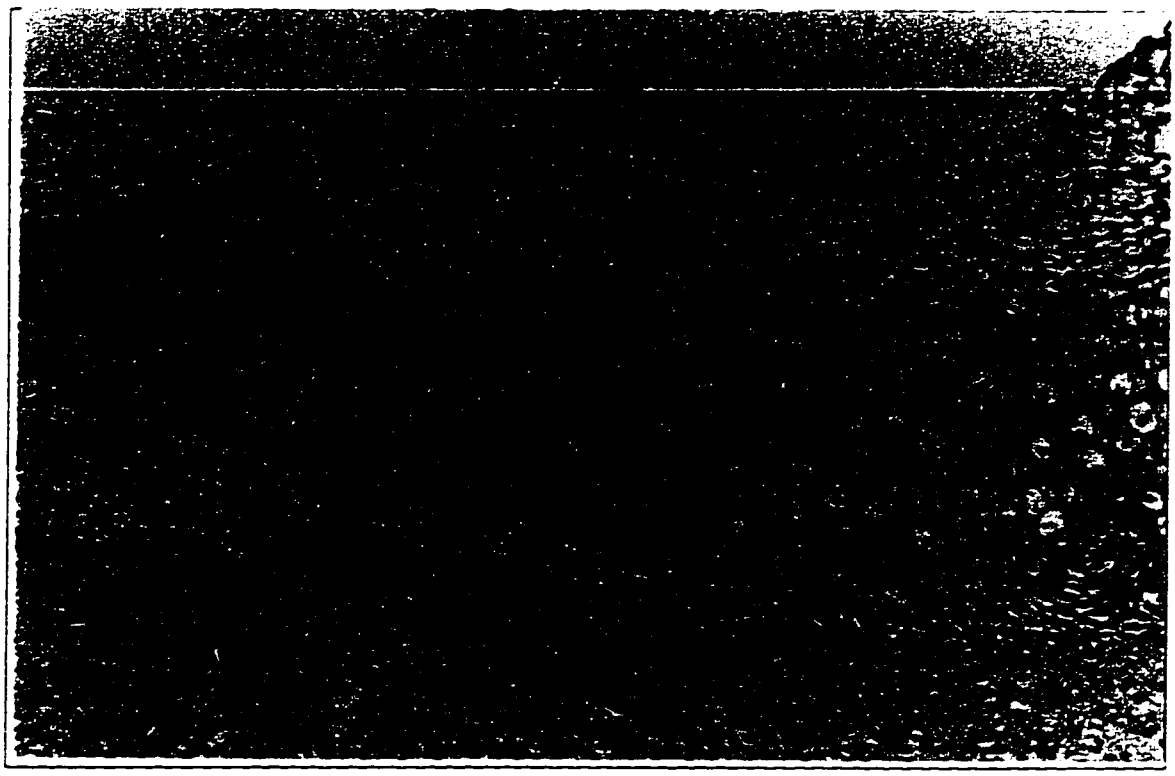

Figure 3.7 Photomicrograph of diastase treated cervical epithelium stained with PAS, demonstrating the loss of PAS positive staining after enzymatic treatment. Note that the basement membrane and endothelial lining are PAS reactive. See text for details (200X).

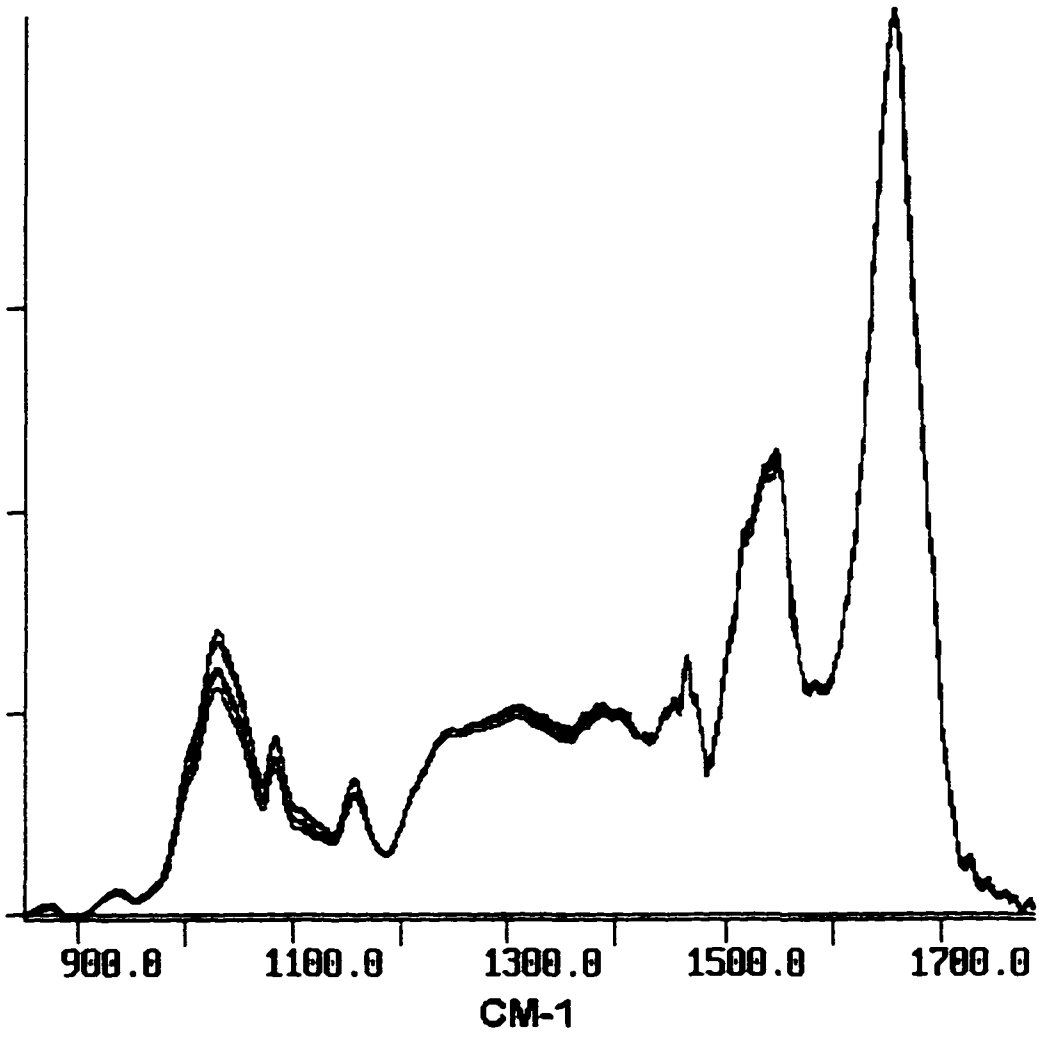


Figure 3:8 FT-IRM spectra between 850 and 1800 $cm^{-1}$ of the superficial layer of a normal sample collected from adjacent areas of the same sample.

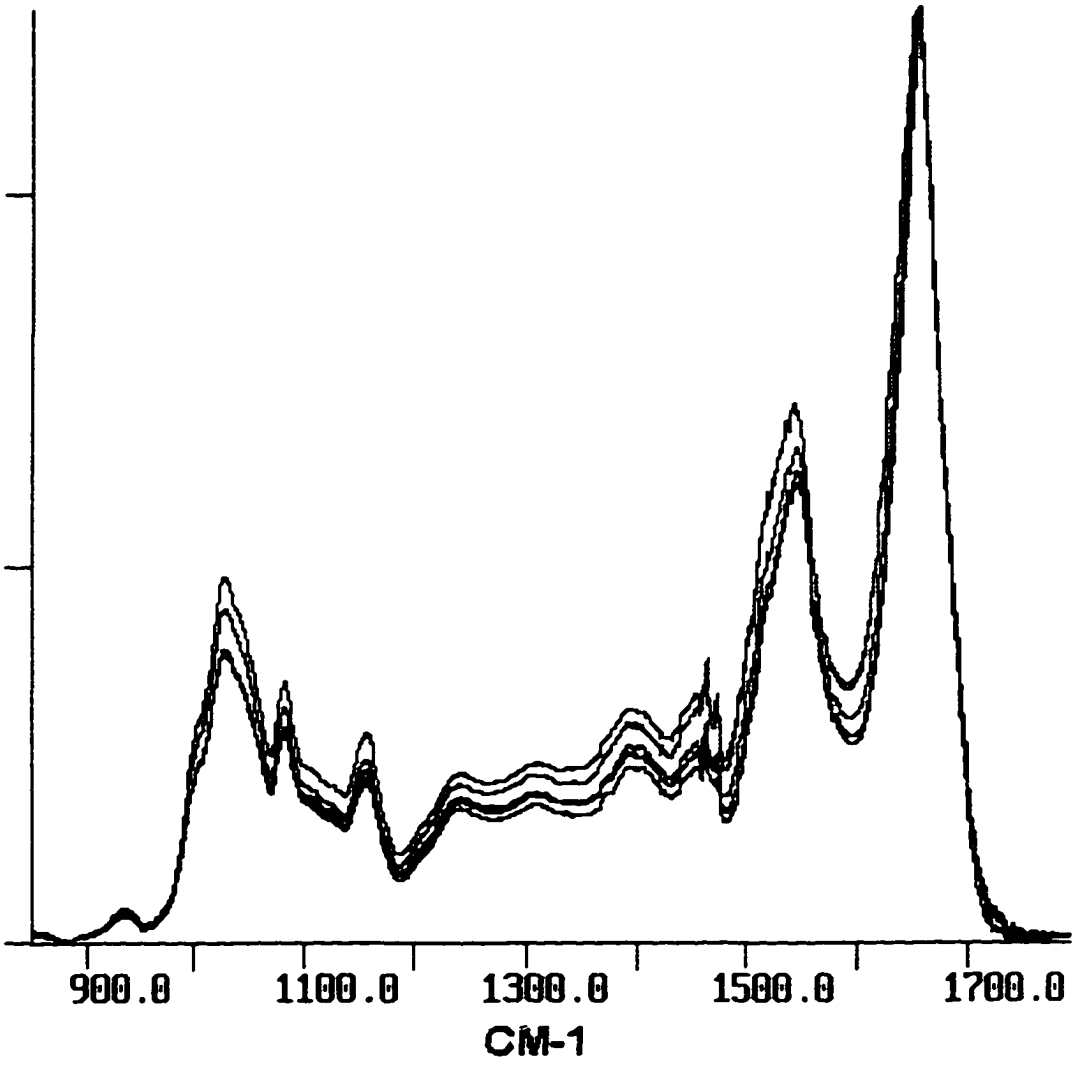


Figure 3:9 FT-IRM spectra between 850 and 1800 $cm^{-1}$ of the intermediate layer of a normal sample collected from adjacent areas of the same sample.

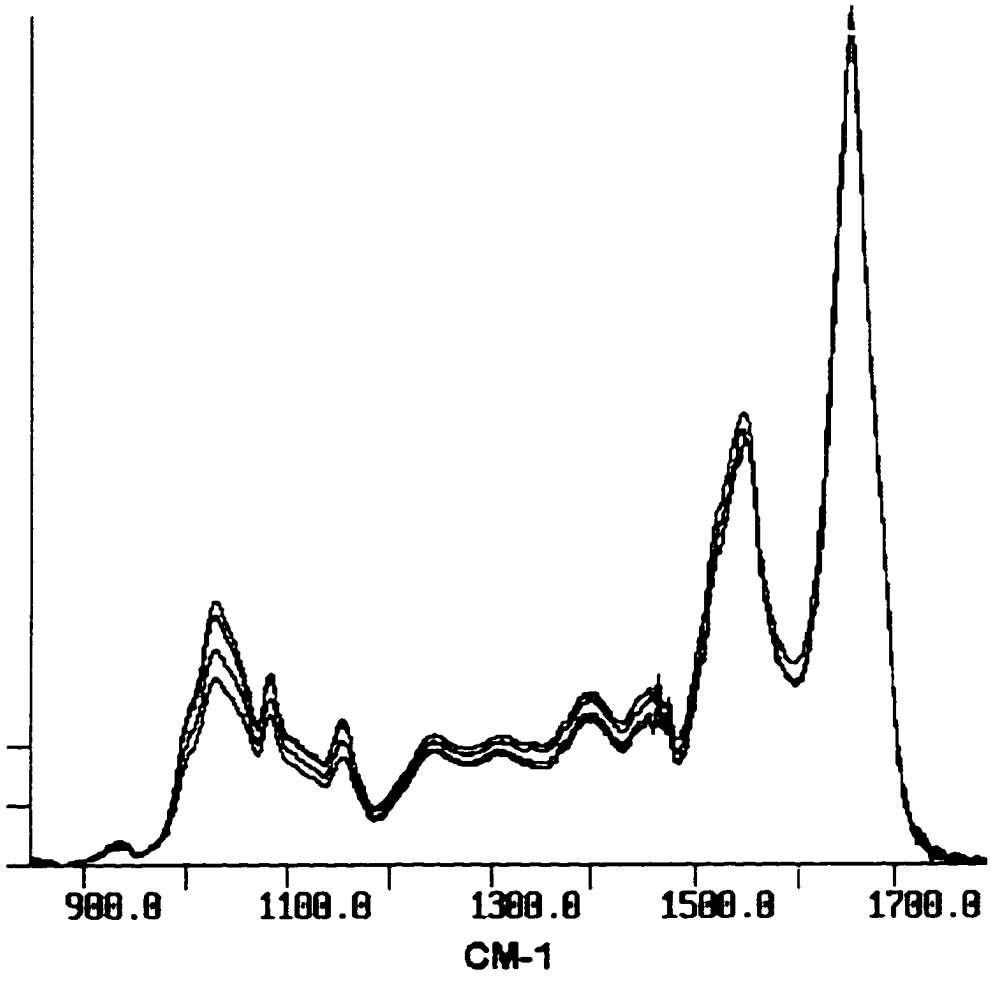


Figure 3:10 FT-IRM spectra between 850 and 1800 $cm^{-1}$ of the parabasal layer of a normal sample collected from adjacent areas of the same sample.

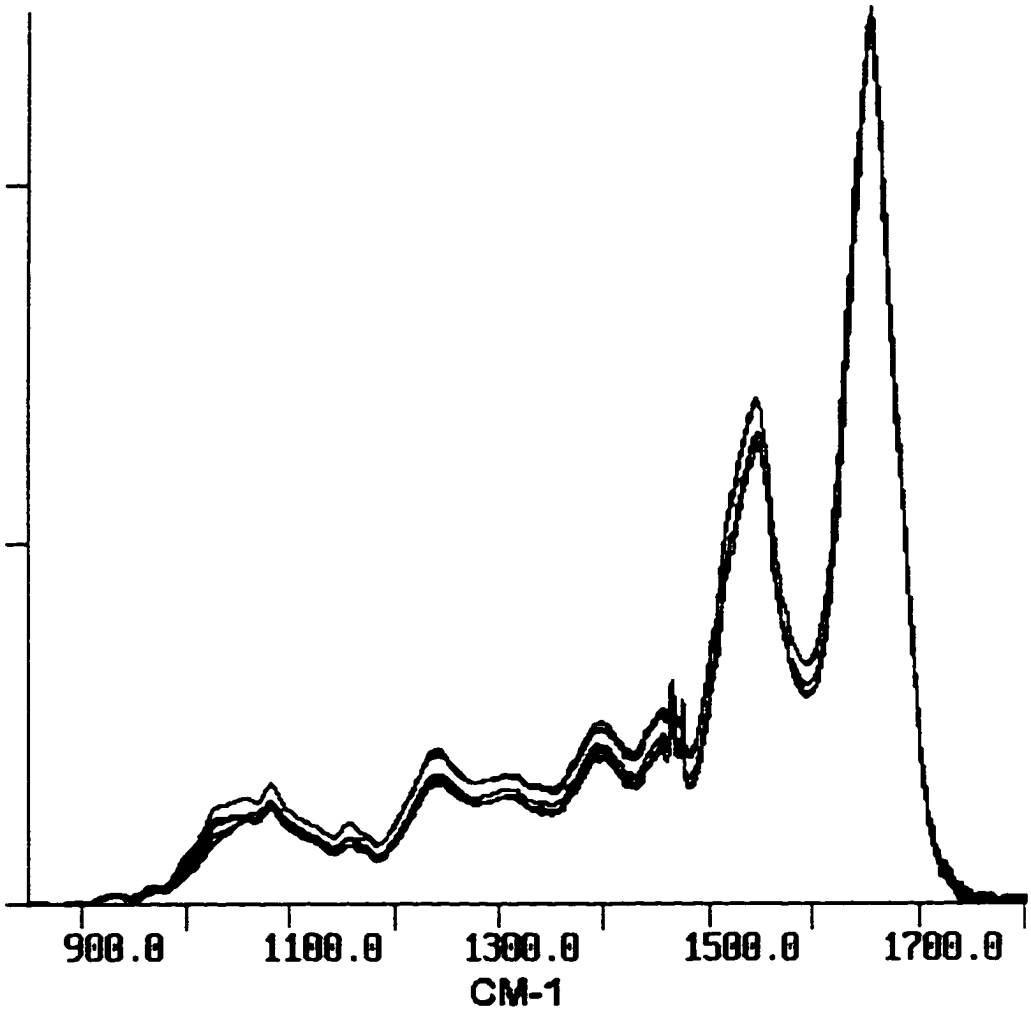


Figure 3:11 FT-IRM spectra between 850 and 1800 $cm^{-1}$ of the basal layer of a normal sample collected from adjacent areas of the same sample.

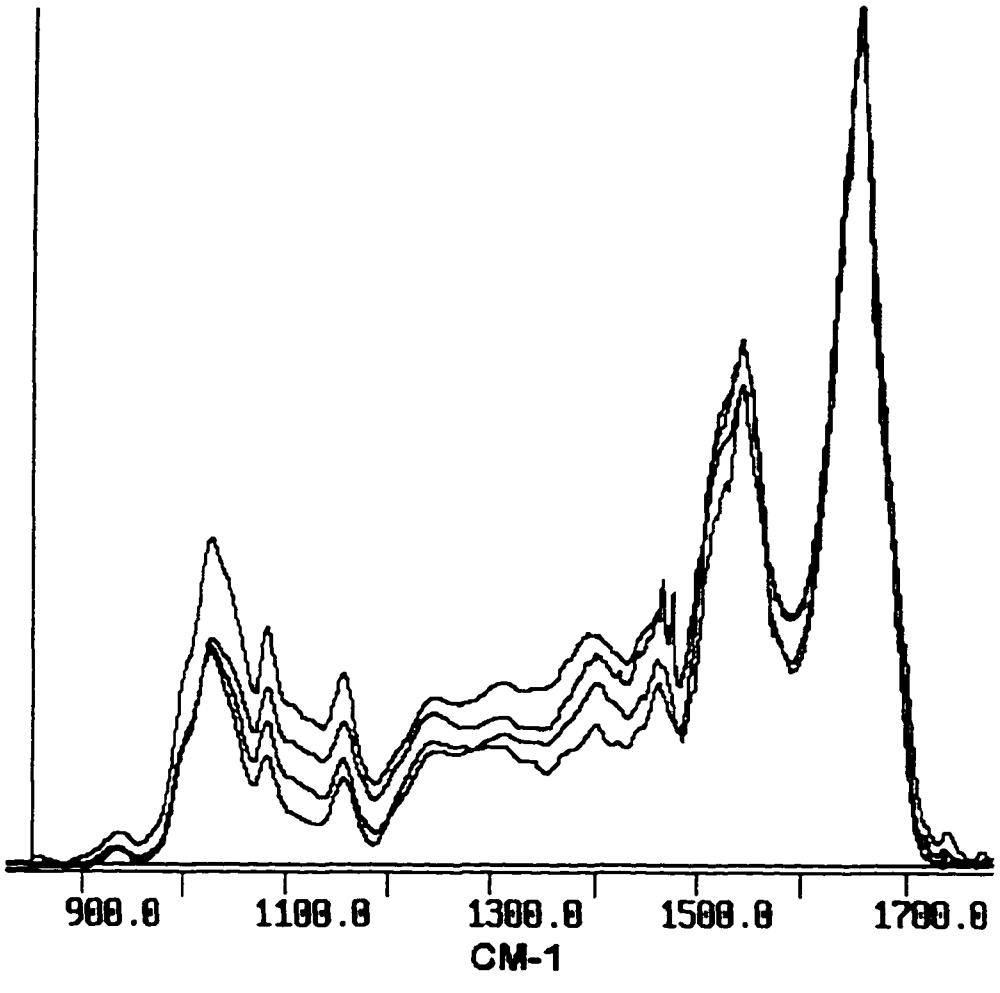


Figure 3:12 FT-IRM spectra between 850 and 1800 $cm^{-1}$ from the superficial layers of four biopsy samples with diagnoses of benign epithelium.

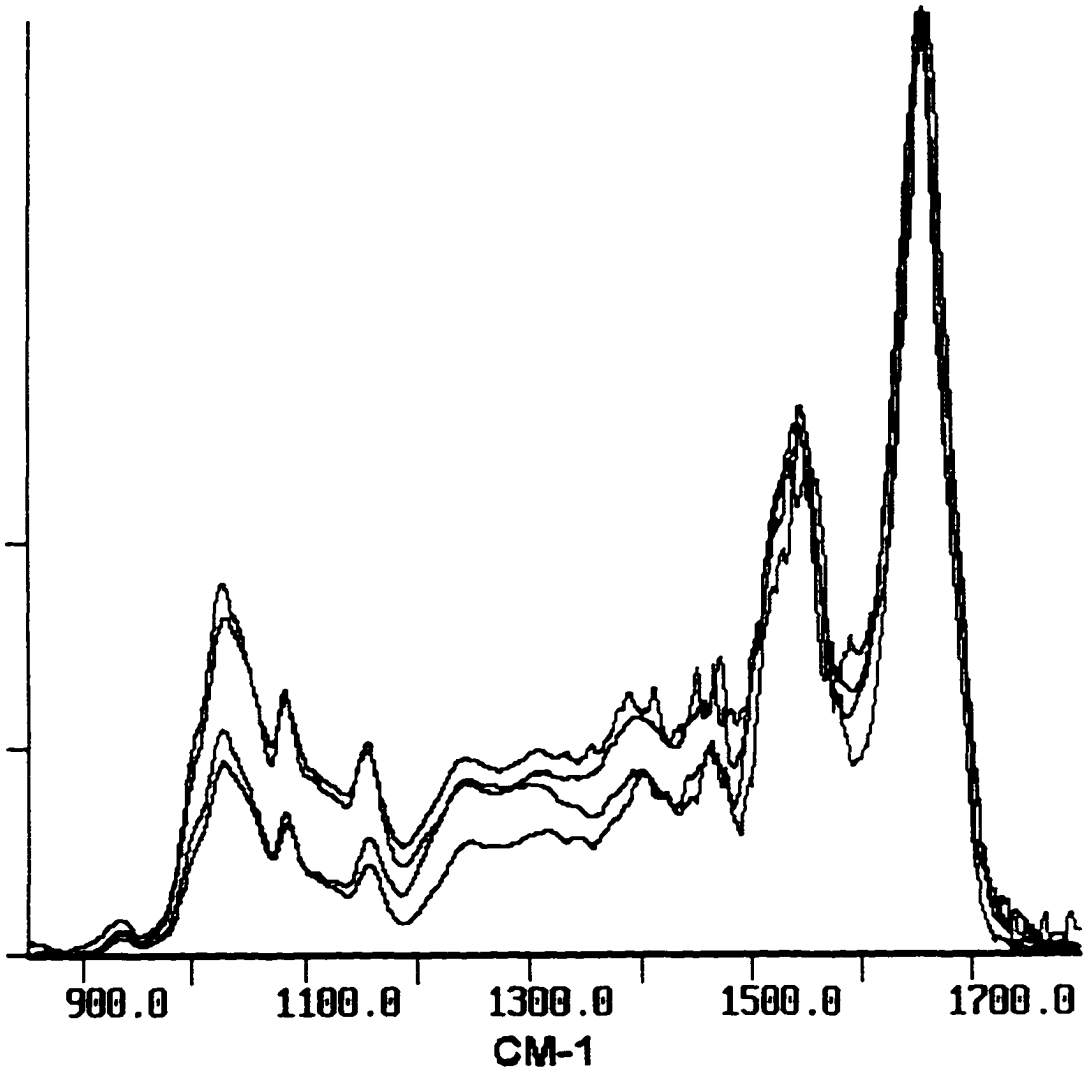


Figure 3:13 FT-IRM spectra between 850 and 1800 $cm^{-1}$ from the intermediate layers of four biopsy samples with diagnoses of benign epithelium.

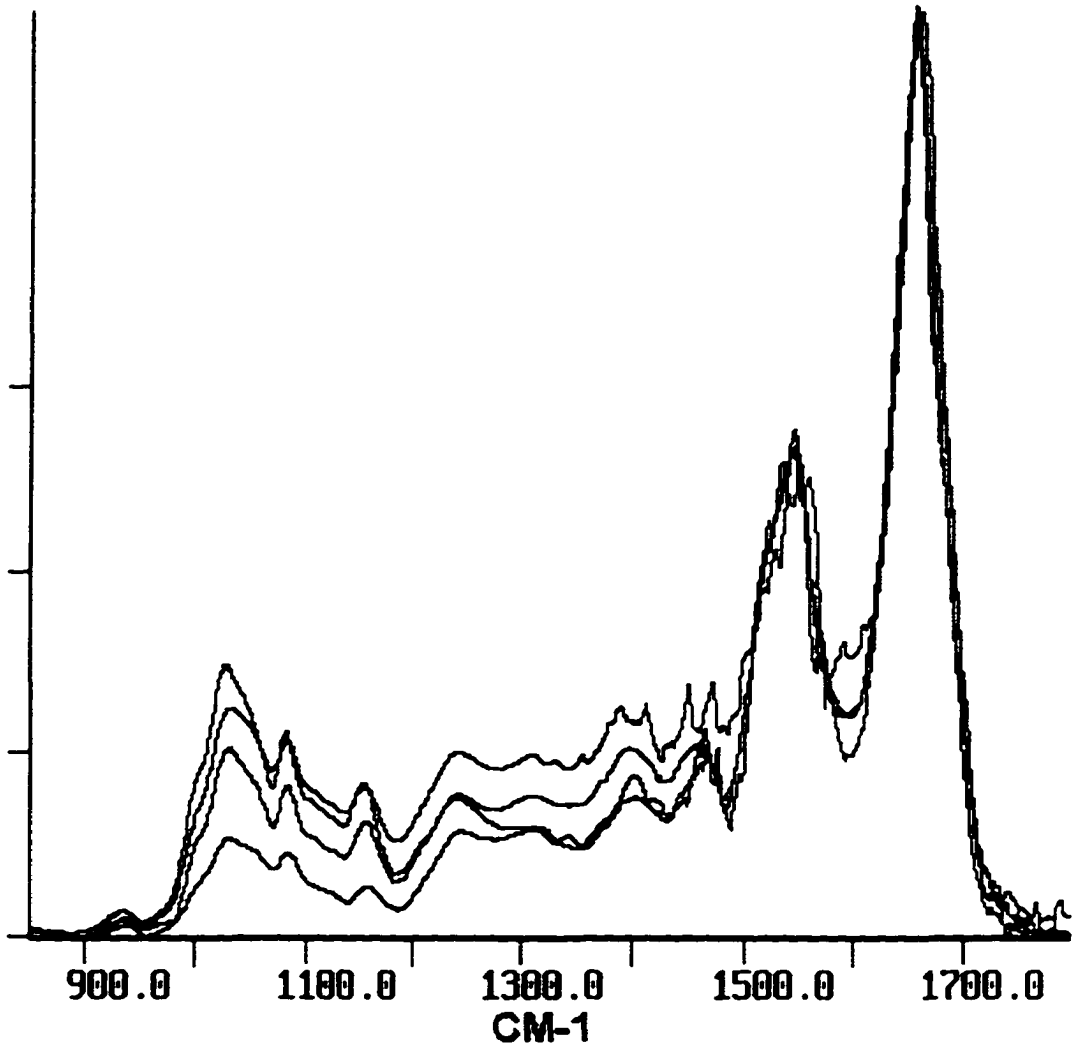


Figure 3:14 FT-IRM spectra between 850 and 1800 $cm^{-1}$ from the parabasal layers of four biopsy samples with diagnoses of benign epithelium.

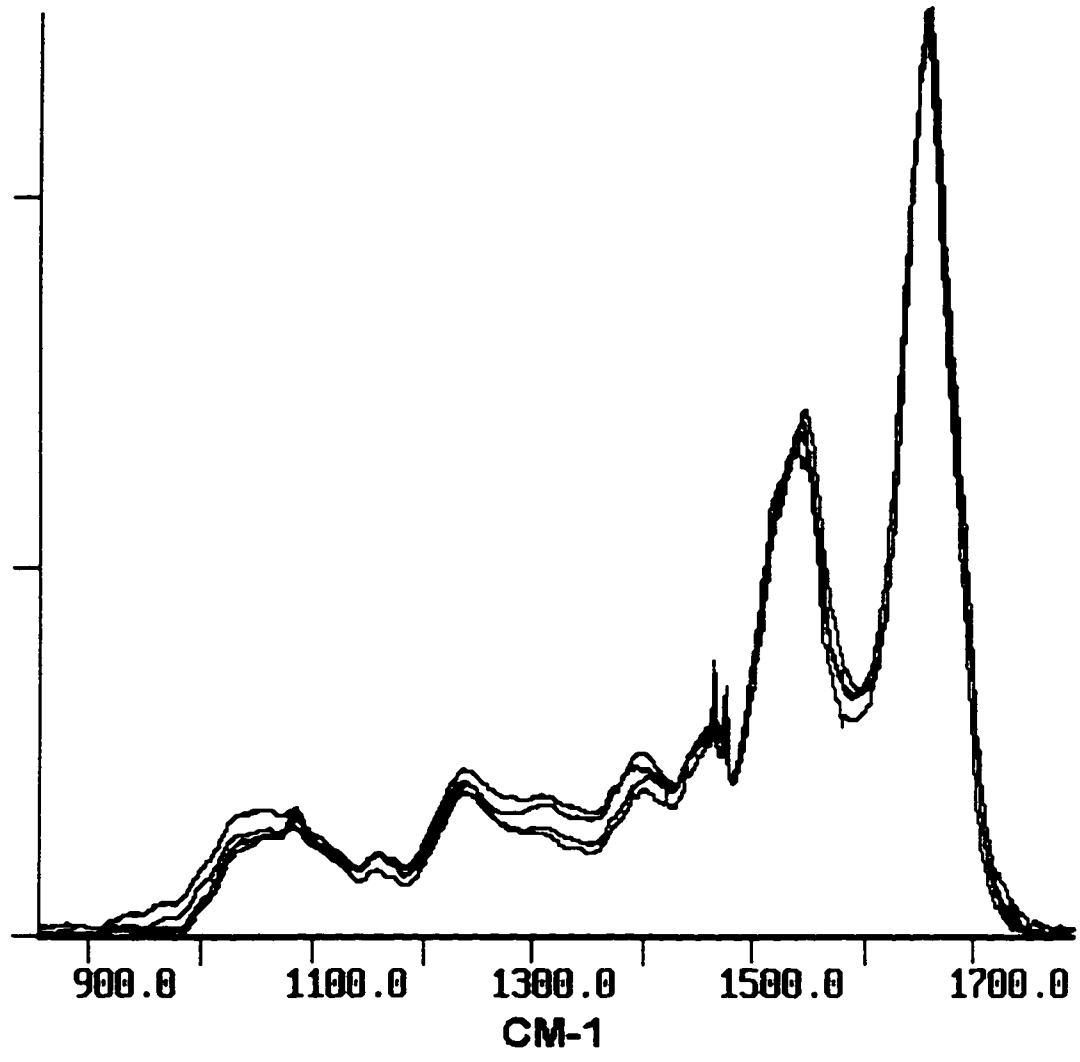


Figure 3:15 FT-IRM spectra between 850 and 1800 $cm^{-1}$ from the basal layers of four biopsy samples with diagnoses of benign epithelium.

## 3.2 FT-IRM Of Invasive Squamous Cell Carcinoma Of The Cervix:

Figure 3:16 is a photomicrograph of a tissue section diagnosed with a well differentiated, invasive squamous cell carcinoma. It is obvious that there is a complete loss of organization of the normal epithelial architecture. Invasive tongues of neoplastic cells can be seen penetrating into the stroma creating a ragged leading edge. Maturation is seen only at the extreme surface of the epithelium as the nuclei become somewhat smaller and condensed. The remainder of the epithelium shows a high degree of pleomorphism. Chromatin clumping is observed in many of the nuclei. The nuclear to cytoplasmic ratio is elevated throughout the epithelium and the cell membranes are indistinct. The leading edge of the invasion contains a greater proportion of anaplastic cells with a high N/C ratio, hyperchromatic nuclei and irregular nuclear envelope. The stroma contains abundant inflammatory cells at the periphery of the tumor. The stroma also shows thickening and increased vascularity below the lesion.

Figure 3:17 shows the spectra collected from the surface and "basal" layer of the invasive carcinoma shown in Figure 3:16. Since there is no true basal layer, the basal spectra are measured from the junction between the tumor and stroma. The spectra of the neoplastic surface have the outward appearance of basal layer spectra, but there are differences. The region between 1000 and 1100 wavenumbers is reduced relative to the 1235 $cm^{-1}$ band compared to normal basal layer spectra. In the

neoplastic surface, this range is also narrowed with a further reduction of the bands at 1031 and 1060 $cm^{-1}$ relative to the 1081 $cm^{-1}$ band. There is no change in the ratio of amide I/II intensities as compared to basal layer spectra of non-neoplastic samples The ratio of intensities of amide III (at 1235 $cm^{-1}$)/II is slightly reduced relative to non-neoplastic superficial cells. On the other hand, the neoplastic basal spectra lose all the features in the region between 1000 and 1100 $cm^{-1}$ and do not resemble any normal spectra. Instead they exhibit a broad absorbance with a prominent peak at 1080 $cm^{-1}$ There is also the appearance of a band at 965 $cm^{-1}$ and a shoulder at approximately 1100 $cm^{-1}$. The weak amide III band located at 1314 $cm^{-1}$ in the normal basal epithelium is significantly reduced compared to normal basal layer. In contrast to the surface spectra, the AIII/AII intensity ratio is elevated compared to normal basal layer spectra.

Figure 3:18 shows 5 spectra collected from the adjacent areas of the surface of the lesion shown in Figure 3:16. These spectra show a high degree of reproducibility indicating that the surface is covered with neoplastic cells that have the same spectral characteristics but are different from the neoplastic basal cells . This is consistent with the appearance of morphologically undifferentiated cells at the surface. Figure 3:19 is a PAS stain of the same lesion shown in Figure 3:16. There is an observable PAS reaction at the surface of the lesion. However, the stain is diffuse within the cells and does not show the same degree of granularity as non-neoplastic cervical epithelium (see Figure 3:6). Diastase digestion does not appreciably reduce the intensity of the PAS staining. This indicates that the staining reaction is not due to glycogen but may

be due to other PAS labile carbon-carbon bonds. The lower levels of neoplastic epithelium exhibit no PAS reaction.

Figure 3:20 shows spectra collected from the surface of a tissue sample diagnosed with moderately differentiated invasive squamous cell carcinoma compared to the well differentiated lesion shown above. The spectra are very similar showing the same loss of 1031 and 1060 $cm^{-1}$ bands with the 1081 $cm^{-1}$ band becoming the dominant feature in the low frequency region. A weak band at 965 $cm^{-1}$ is also present in the moderately differentiated lesion. In comparison, the ratio of amide III/II is not elevated in the moderately differentiated lesion and more closely approximates that which is observed for non-neoplastic basal cells.

The neoplastic basal layer spectra of the two different grades of neoplasia are shown in Figure 3:21. These spectra are similar but show a significant difference from the surface spectra. In both grades of neoplasia the band at 1081 $cm^{-1}$ becomes the dominant feature in the low frequency range. The moderately differentiated lesion is somewhat more influenced by a component in the 1030-1060 $cm^{-1}$ range that broadens the band toward the low frequency. The weak band at 1314 $cm^{-1}$ in the well-differentiated lesion is also present in the moderately differentiated lesion. As at the surface, the spectra of neoplastic basal cells of the moderately differentiated lesion, has an amide III/II ratio that is closer to that of normal basal cells. It should be noted that the invasive component of the section measured in the moderately differentiated lesion, had not progressed as far as the well differentiated lesion. The high degree of invasive character found in the well differentiated lesion is lacking in the epithelium of

the moderately differentiated lesion. As a result some of the spectral characteristics, especially in the basal layer, more closely resemble the normal basal layer spectra.

Since both of these lesions were invasive, the invasive components were also measured. Figure 3:22 shows the physical relationship of the surface and the invasive component of the well differentiated lesion described above. The invasive component shown at right in the Figure originates from a different area of the neoplasm which has moved perpendicular to the surface. The surface at left is approximately 6 millimeters from the invasive band which now occupies a large portion of the cervical stroma. Figure 3:23 is a higher magnification view of the left hand margin of the invasive component. A band of stroma interspersed with inflammatory cells is seen at the periphery of the lesion. Several nests of neoplastic cells are seen with keratin pearl formation in the center. The nests show some organization with a low degree of differentiation that is not seen in the epithelial component. These cells do not appear as anaplastic as those found at the surface.

Figure 3:24 shows the spectra collected from a chord of neoplastic cells of the well differentiated mass shown above and of the moderately differentiated neoplasm shown previousiy. The spectra are nearly superimposable. Both spectra show the same loss of features in the 1000-1100 wavenumber range. Mainly the loss of the 1031 and 1060 $cm^{-1}$ bands coinciding with the appearance of the 965 $cm^{-1}$ band. In contrast to the epithelial component, both invasive components have elevated AIII/AII intensity ratios.

In both well and moderately differentiated neoplasms, dyskeratosis is present within the tumor mass. In a well differentiated tumor, this is manifested by the formation of concentric whorls of heavily keratinizied superficial-like cells in the center of the neoplastic nests. In a moderately differentiated neoplasm keratin pearl formation is absent but individual cellular keratinization is seen in the center of tumor nests . Figure 3:25 shows the spectra of a keratin pearl (see Figure 3:19) compared to the neoplastic cells shown in Figure 3:24. The keratin spectra does not show the 965 $cm^{-1}$ band but does have prominent 1081 $cm^{-1}$ and 1130 $cm^{-1}$ bands in the low frequency region. The amide III peak is similar in shape and frequency to that observed in normal epithelium. However the amide III/II ratio is as low as that observed for non-neoplastic basal cells. The keratin AI/AII ratio is higher than any of the spectra and actually approaches the level of stroma. In comparison, the neoplastic invasive cells of both tumors do not resemble the keratin spectra very closely However, significant similarity is seen in the AI/AII ratio for the moderately differentiated lesion which has an AI/AII ratio that is closer to that of the keratin spectrum.

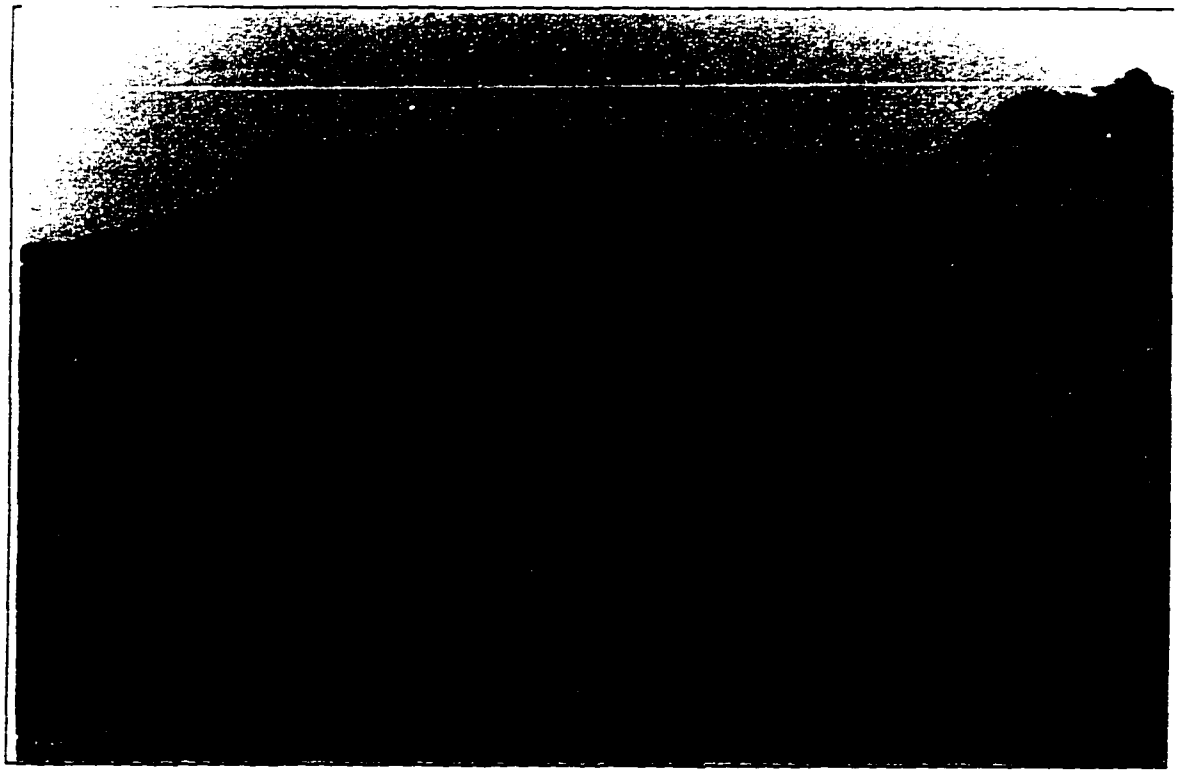

Figure 3:16 Photomicrograph of the epithelial surface of a well differentiated squamous cell carcinoma. Note the lack of organization and differentiation throughout the majority of the epithelium. (SU= surface, B= basal area, 200X, H&E).

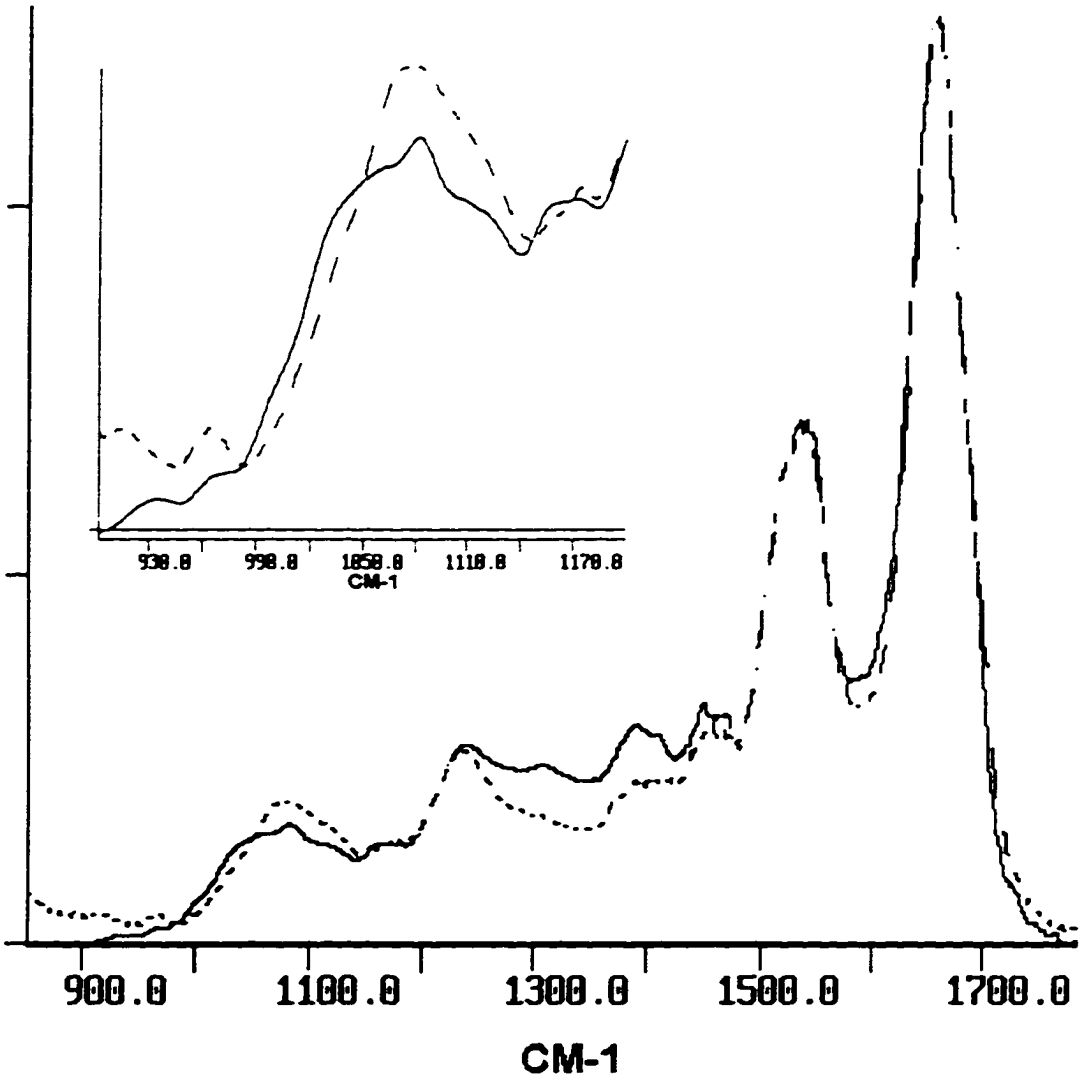


Figure 3:17 FT-IRM spectra between 850 and 1800 $cm^{-1}$ collected from the surface (solid) and basal (dot) area of the well differentiated squamous cell carcinoma shown in figure 3.15. Inset: expanded view between 900 and 1200 $cm^{-1}$.

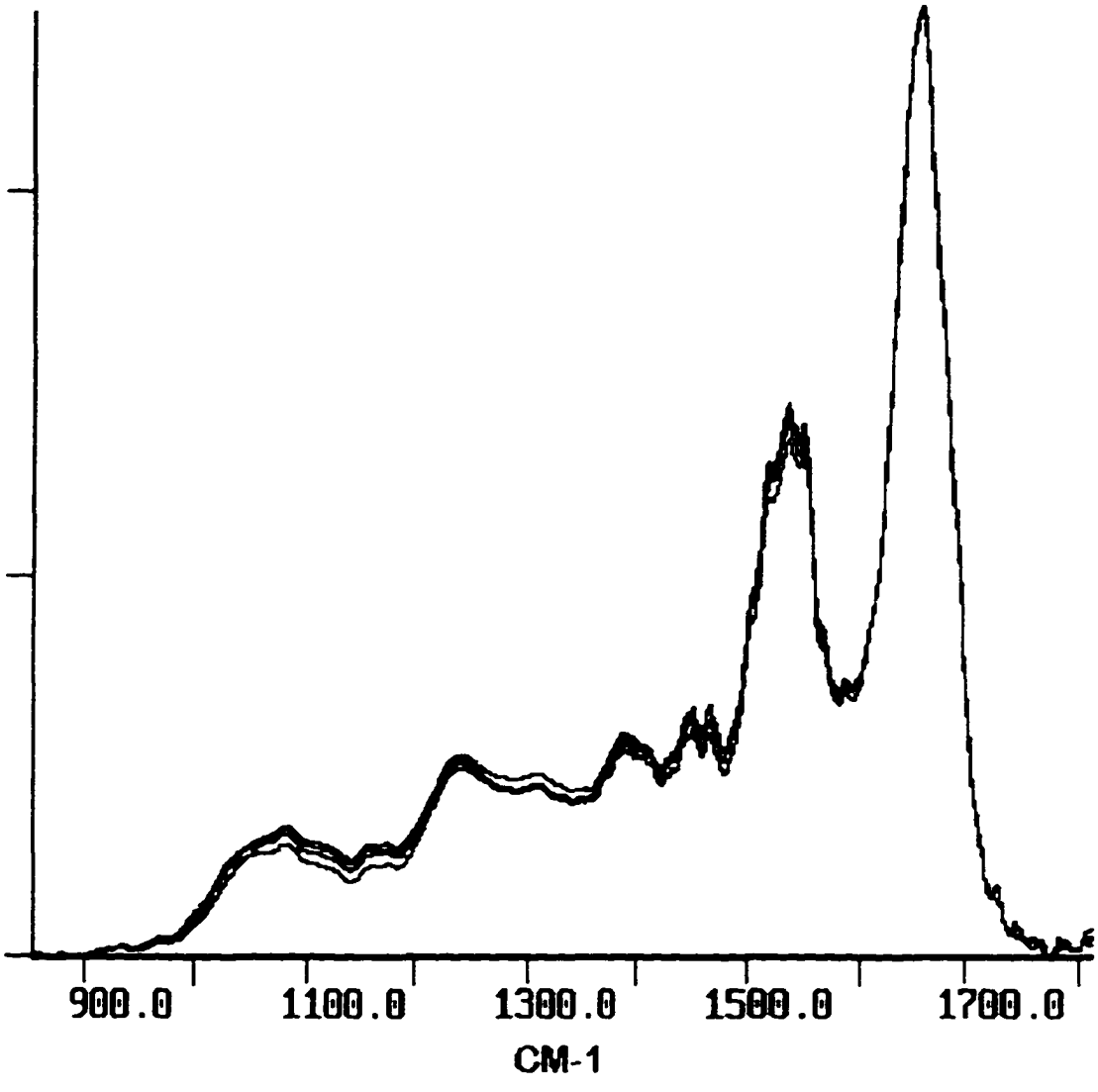


Figure 3:18 FT-IRM spectra between 850 and 1800 $cm^{-1}$ collected from five adjacent areas of the surface of a well differentiated squamous cell carcinoma.

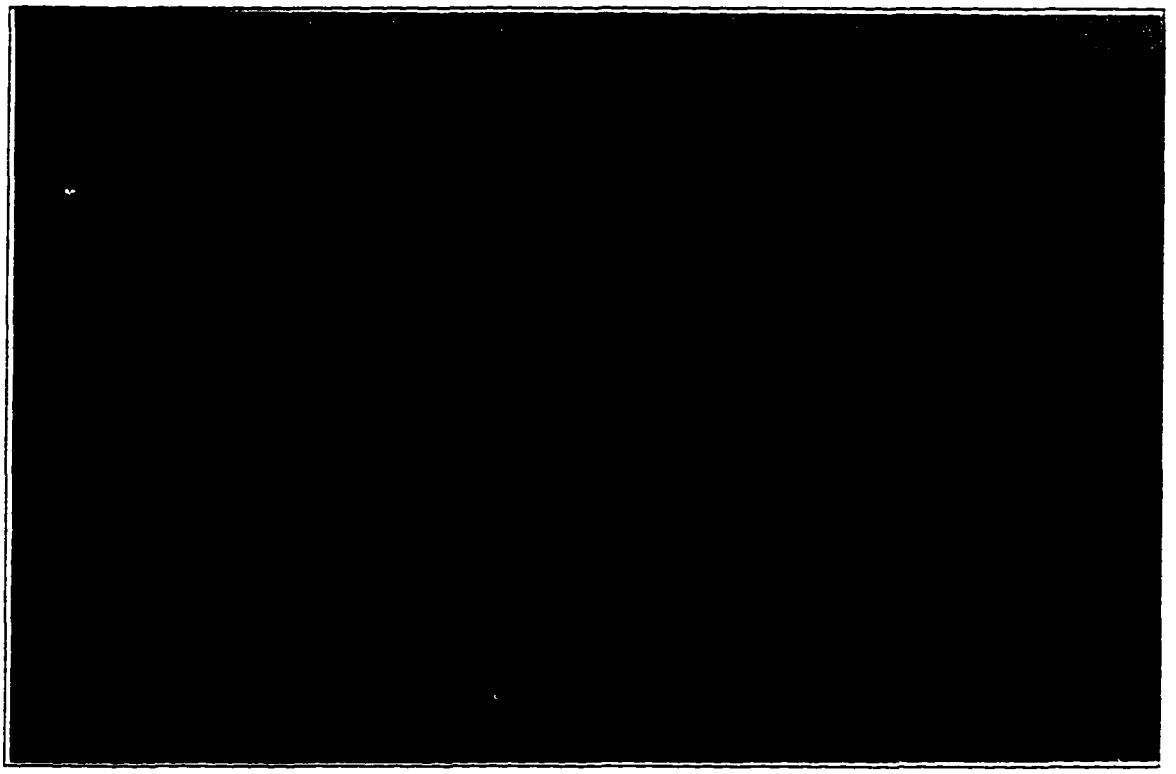

Figure 3:19 Photomicrograph of the PAS reaction in the epithelial surface of a well differentiated squamous cell carcinoma. There is diffuse PAS staining of the uppermost layer (arrow) with the remainder of the epithelium showing a weak reaction (400X).

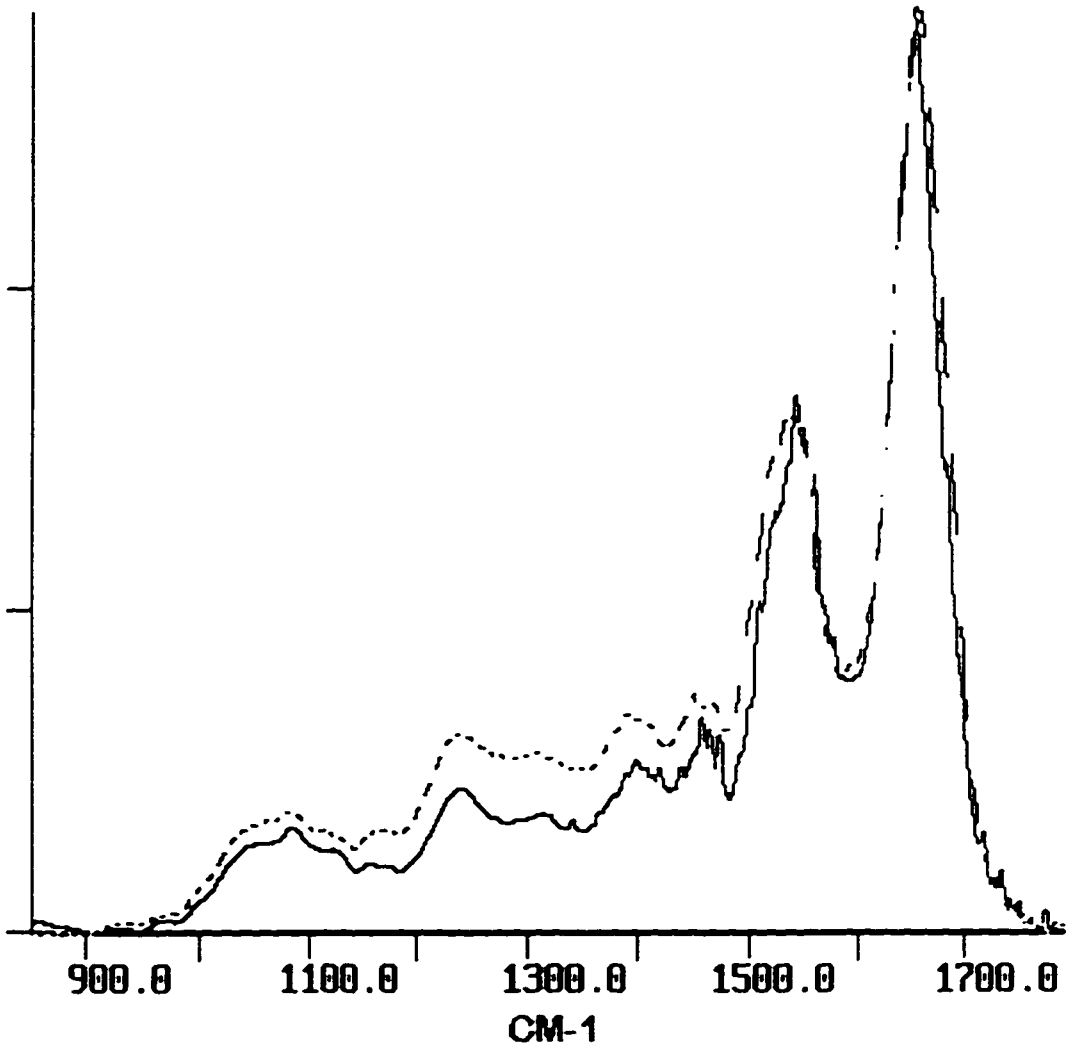


Figure 3:20 FT-IRM spectra between 850 and 1800 $cm^{-1}$ collected from the surface of a well differentiated (dot) and moderately differentiated (solid) squamous cell carcinoma.

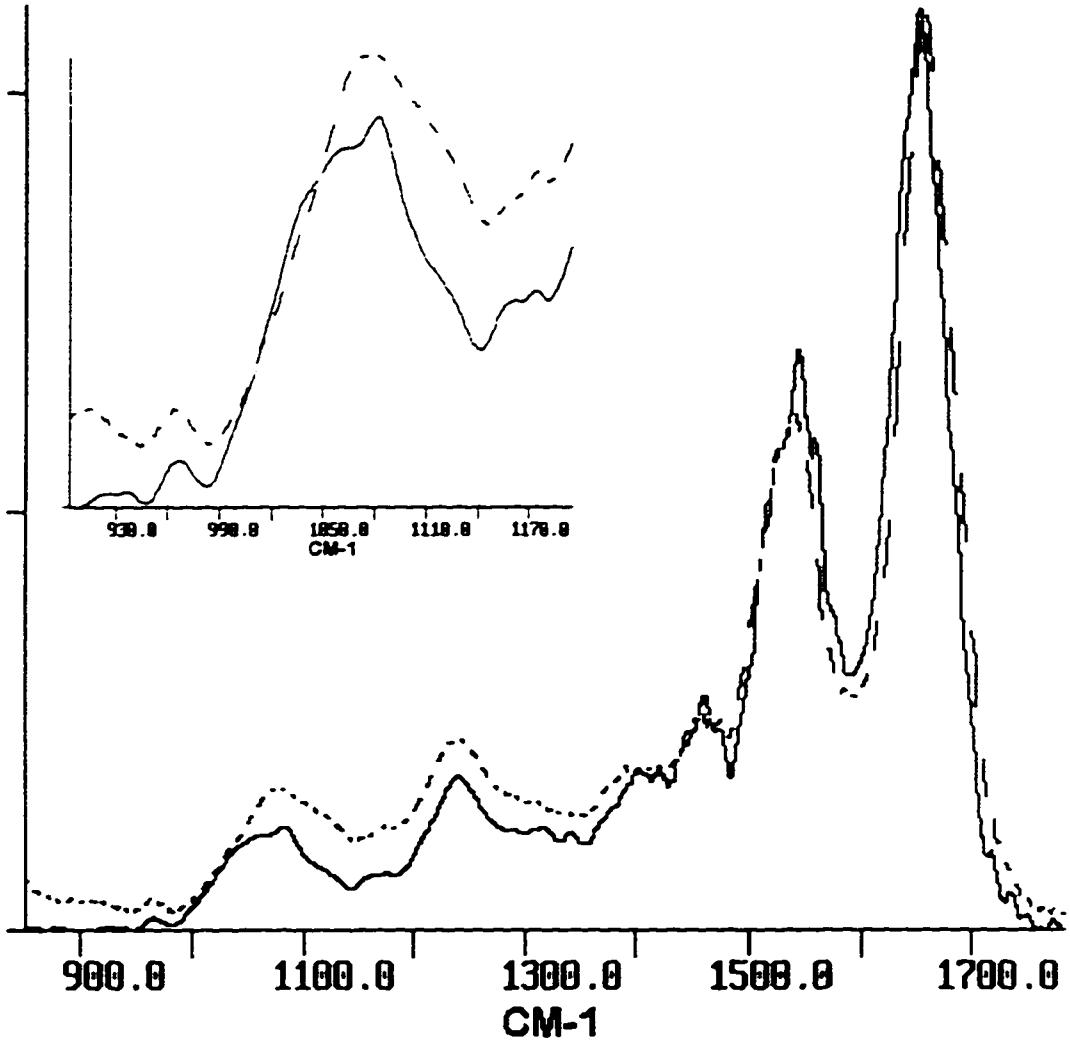


Figure 3:21 FT-IRM spectra between 850 and 1800 $cm^{-1}$ collected from the basal area of a well differentiated (dot) and moderately differentiated (solid) squamous cell carcinoma. Inset: expanded view between 900 and 1200 $cm^{-1}$.

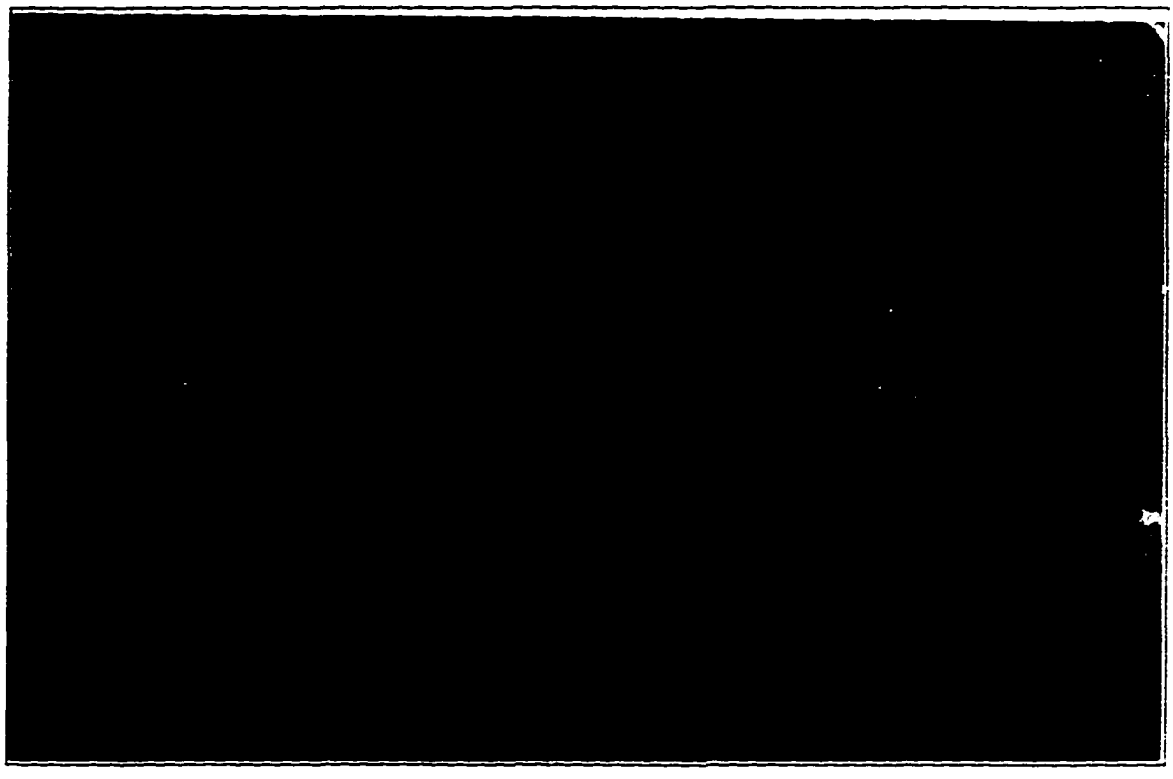

Figure 3:22 Photomicrograph showing the relationship of the epithelial surface (SU) and invasive component (IN) of a well differentiated invasive squamous cell carcinoma. The invasive component has penetrated 6 millimeters and occupies a large portion of the cervical stroma (ST) (4X, H&E).

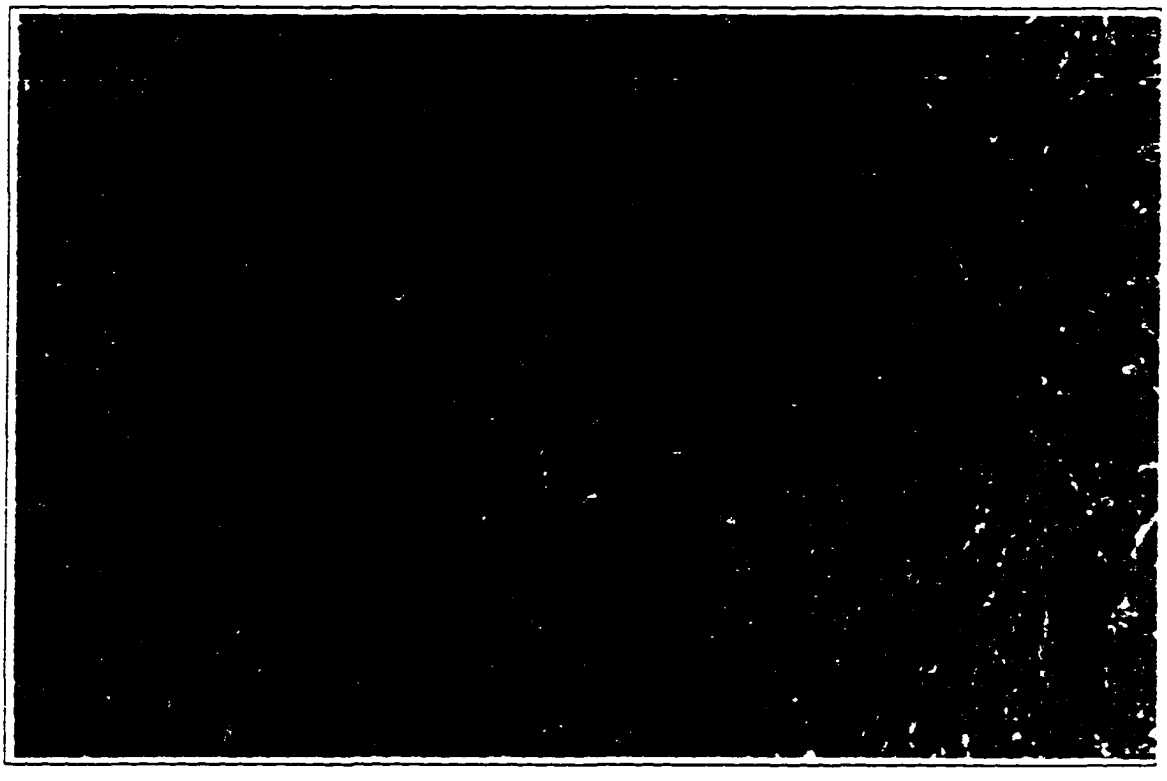

Figure 3.23 Photomicrograph of the proximal margin of the invasive lesion shown in figure 3.22. Multiple nests of tumor cells (TC) are present and surrounded stromal (ST) elements. Keratin pearl (KP) formation is evident in several of the tumor nests (200X, H&E).

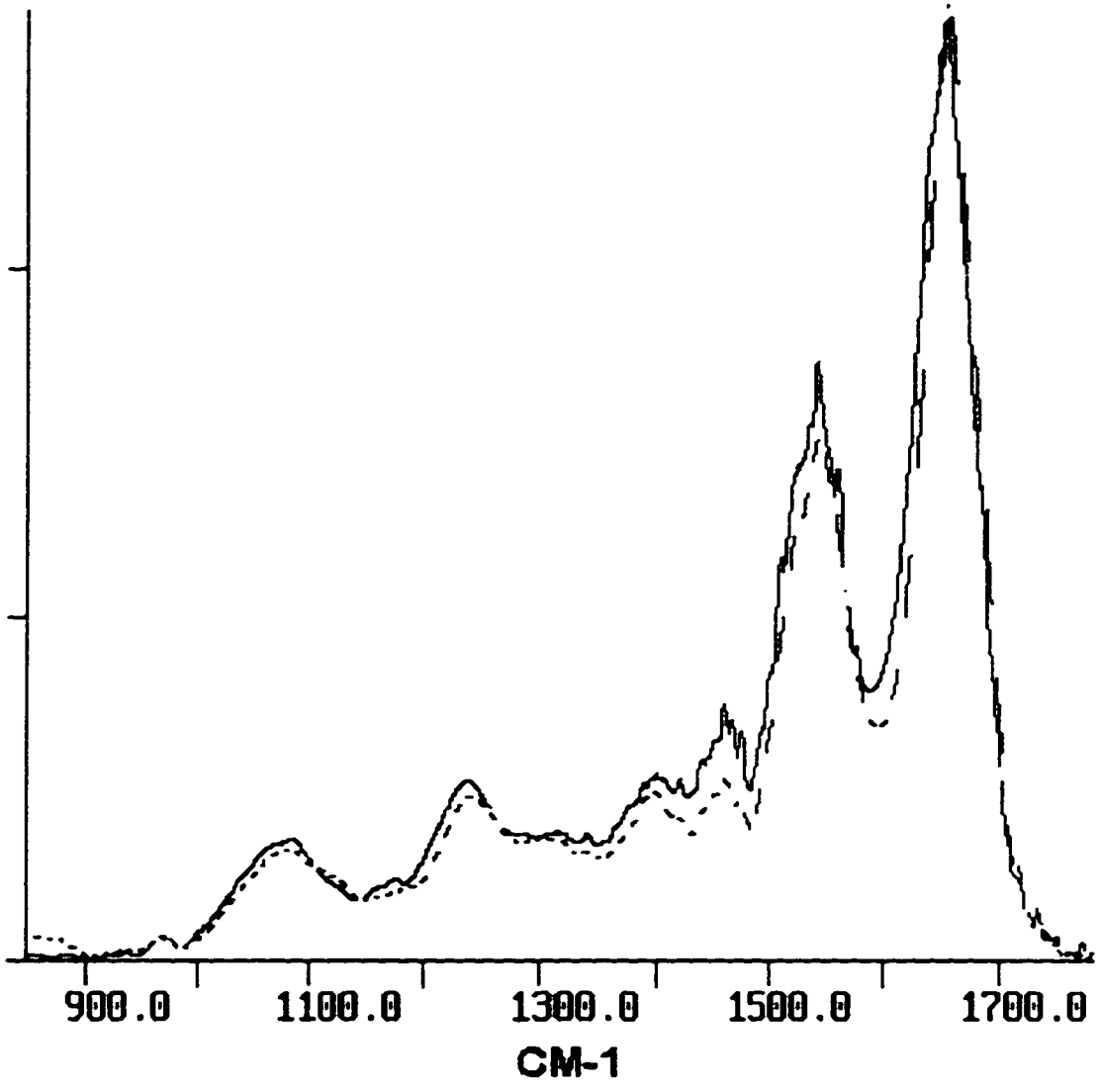


Figure 3:24 FT-IRM spectra between 850 and 1800 $cm^{-1}$ collected from the invasive tumor component of a well differentiated (dot) and moderately differentiated (solid) squamous cell carcinoma.

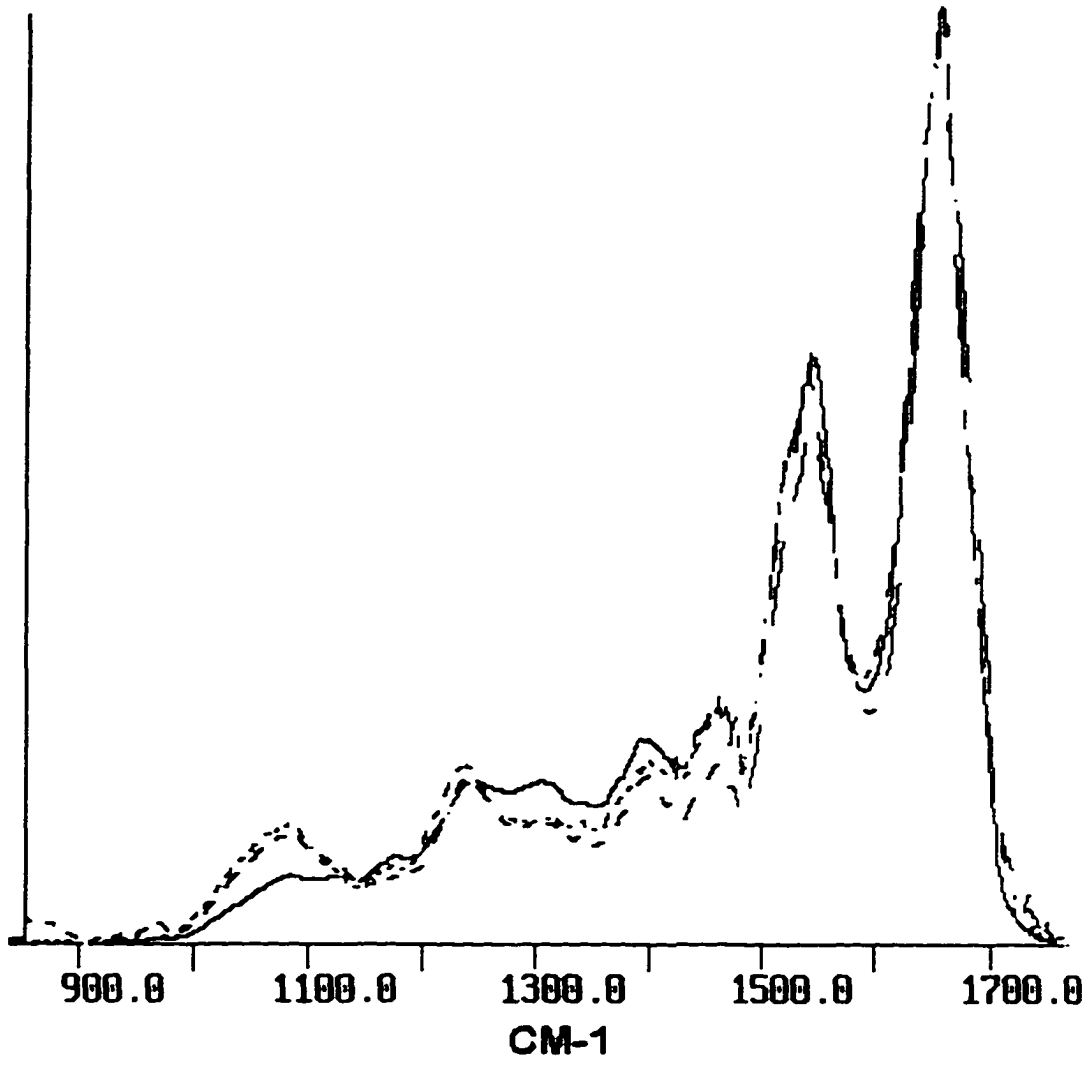


Figure 3:25 FT-IRM spectra between 850 and 1800 $cm^{-1}$ collected from a keratin pearl (solid) in the invasive component of the well differentiated carcinoma and compared to the well differentiated (dashed) and moderately differentiated (dot) tumor cells shown in figure 3.23.

# Chapter 4 : Discussion

It is clear from the previous section that the spectra of the various normal cervical epithelial layers exhibits a high degree of reproducibility among the same and different samples. With the exception of the lower layers, the spectra shown above are in agreement with the observations of others (Wong, Wong et al. 1991, Morris, Lee et al. 1995). Previous studies were based on data collected from exfoliated cervical epithelial cells. In contrast, the samples utilized in this study were obtained from formalin fixed paraffin embedded biopsies collected during routine cervical examination. The histopathologic methods used to prepare and visualize tissue sections have been in use for over 70 years and are extremely reliable. Formalin fixation, the most critical part of tissue processing, does not effect the infrared spectra obtained from processed tissue biopsies, consistent with the observations of others (O'Leary and Levin 1985; O'Leary 1989; O'Leary, Engler et al. 1989; Mason and TJ 1991; Estepa-Maurice, Hennequin et al. 1996). The largest effect of tissue processing results from the presence of residual paraffin wax in the tissue section. However, the areas in which the paraffin infrared signature is present can be neglected during qualitative spectral comparisons. Therefore, tissue processing has a minimal impact on the quality and reliability of the spectra obtained from this material. In addition, considering the differences between the sample preparation of exfoliated cells and tissue biopsies, the spectra show a remarkable degree of similarity. This also

indicates that biopsy sample treatment has a minimal impact on the quality of spectra obtained (A: Chiriboga, Xie et al. 1997; B: Chiriboga, Xie et al. 1997; C: Chiriboga, Xie et al. 1997).

There are two factors that require consideration when evaluating the results obtained from FT-IRM measurements of tissue sections. First, because the sample on the $BaF_2$ window is unstained, careful examination of an adjacent H&E section is required to correlate the window histology with the actual histology. However, the optical resolution of an unstained tissue section is such that accurate discrimination of distinguishing features between layers is not always possible. In addition, the maturation process of the epithelium is gradual and distinct boundaries between layers are not observed in the unstained section. Thus, overlap of measurements between layers cannot be avoided. Moreover, differences of more than 10 microns between sections can make visual interpretation and correlation difficult. Gross features of epithelial structure can be altered significantly in the span of 10 or 20 microns. This is exemplified by changes in the planarity of the basal layer. Stromal papillae punctuate the cervical epithelium providing vascularity to the lower levels of the epithelium. This causes undulations in the architecture of the epithelium generating the appearance of lower level cells closer to the epithelial surface (see Figure 3:2). Differences in the depth of the section obtained from the tissue block may obscure the presence of these features. Similarly, different angles of sectioning will influence the material obtained from the tissue block. In order to reduce artifacts of this type, only sequential sections were used to generate the window and corresponding H&E section, ensuring the smallest possible difference between H&E and IR sections. This allows for the

greatest degree of histologic accuracy to be attained from the superficial and basal layers where architectural and spectral features make avoidance of overlap of measurements straight forward. Secondly, measurements of the layers represent the average of fractions of several cells. In the superficial layer, the data are collected from a 6 micron-thick cross section of a group of cells that on average measures 50 microns in diameter. At a maximum, only 12% of the total cell volume of any superficial cell can be measured by IR in the superficial layer at any one time. Similarly in the basal layer, the cells measure 10 microns in diameter, yielding a 60% measurement of the total cell volume. Therefore, measurements of the different layers represent the average of a group of cells belonging to that specific layer. In order to enhance the averaging effect of measuring a cross sectional group of cells, long window apertures were used to maximize the sampling area. Unfortunately this tends to increase the influence of the artifacts mentioned above.

## 4.1 Normal Cervical Squamous Epithelium:

The main spectral differences observed for the different layers of normal cervical epithelium arise from the variation in the proportion of glycogen present in the layers. The spectra of the superficial, intermediate and parabasal layers clearly show the presence of glycogen as the distinct pattern between 900 and 1200 $cm^{-1}$. This correlates well with the observed distribution of positive staining in PAS treated cervical epithelial sections. The absence of staining when the samples are treated by diastase indicates that the positive PAS staining is due exclusively to glycogen. Spectrally the superficial and intermediate layers contain the greatest proportion of glycogen as measured by the G1/AI intensity ratio shown in Table 4.1. The parabasal layer contains, on average, 10% less glycogen in comparison to the upper layers. Spectrally, the basal layer contains little or no glycogen which can also be seen in the PAS stained section. The basal layer exhibits a weak PAS reaction because of the presence of small amounts of carbohydrates associated with the basement membrane. In the parabasal layer, the cells closest to the basal layer exhibit very little staining. As these cells mature the distribution of glycogen becomes more granular and encompasses a greater proportion of the cell. The spectral glycogen variation in one layer of the same sample is, on average, less than 5%. The variation arises from the displacement of epithelial layers by stromal papillae and/or measurement overlap among the layers. Both of these can be compounded by deviations in the thickness of

the epithelium due to improper embedding of the tissue sample. Samples that are not embedded perpendicularly across the entire length of epithelium can change the relative positions of the layer boundaries in different parts of the epithelium. Not surprisingly, intra-sample variation is quite large, and in some cases, may exceed 25%. This may be due to several factors of which the estrus cycle is the most obvious. Other factors such as recent pregnancy, use of medication and prior disease may also impact the level of glycogen within the different layers.

The other main spectral feature in the epithelial layers consists of the amide I and amide II bands. The position of the amide I band does not change significantly for the different layers and remains relatively constant between 1650 and 1655 $cm^{-1}$. This does not appear to be the case for the amide II absorption. Both the amide I and amide II bands contain a significant amount of information within their respective envelopes. However, because of poor purging of moisture from the instrument and water-subtraction, information available in the amide I and II bands was lost in the strong water vapor absorbance between 1500 and 1700 $cm^{-1}$. Of particular interest is the broadening of the amide bands. This is exemplified in the spectra of the stroma which has amide half widths of approximately 20 $cm^{-1}$ greater than in the epithelial layers as shown in Table 4.2.

In addition to relatively stable frequencies, the AI/AII ratio is also relatively constant among the four normal epithelial layers. This is surprising considering that the N/C ratio decreases significantly as the cells mature from basal zone to the superficial zone. An indication of the change in N/C ratio should be reflected in a shift

of the AI/AII intensity ratio. Figure 3:5 illustrates that nucleic acids can contribute to the magnitude of the amide I band but will have little effect on the amide II band. The amide II band intensity is principally derived from the protein component of the cells. Therefore, the AI/AII ratio should increase with increasing nucleic acid concentration. As the cells mature, and the N/C ratio decreases, one expects a smaller contribution from nucleic acids. However, this effect is not observed because the nuclei of normal epithelial cells are densely packed with protein and DNA. The concentration of infrared absorbing groups within a condensed nucleus of a normal cell is extremely high. Infrared measurements at such high concentrations would produce absorbance values well in excess of 1 absorbance unit. In principle, infrared light would not be capable of penetrating the nucleus. The opposite effect occurs in stained tissue sections. Hematoxylin only stains condensed nuclear material or heterochromatin. Examination of the H&E stained section in Figure 3:2 indicates that 99% of the cells are interphase and have homogeneously densely staining nuclei. Therefore the nucleus of normal interphase epithelial cells is condensed and non-transparent in the infrared. This is supported by examining the basal layer spectra since it represents the most likely location for observing any spectral features of nucleic acids. The nucleus in a basal cell occupies approximately 75% of the cell volume and proportionally should contribute strongly to the spectra. Figure 4.1 is a comparison of DNA with the basal layer obtained from a normal sample. The basal layer spectra contains only a weak absorbance at 965 $cm^{-1}$ and a shoulder at 1095 $cm^{-1}$ for which DNA or RNA might be responsible. Other distinctive features may be hidden in the spectra by overlap and more intense components. RNA in the form of ribosomes may contribute to the

spectral signature. Typically, cells that produce large amounts of proteins for internal use display cytoplasmic basophillia. This is not due to the protein but the result of a large number of free ribosomes within the cytoplasm. Epithelial basal cells express a moderate amount of basophilic staining. Ribosomes are relatively small particles, measuring about 0.02 microns. The local nucleic acid concentration is not prohibitively high. Thus it is possible that RNA will contribute to the spectrum. However, a strong spectral signature of nucleic acids is essentially absent in the spectra of normal mature epithelial layers and only weakly present in the basal layer. This interpretation is also supported by the AI/AII intensity ratios which vary by less than 3%.

A similar but opposite effect is observed in the AI/AII intensity ratio of cervical stroma. The spectral signature of stroma is by far the most easily recognizable and distinguishable of all spectra collected. Similar spectra for connective tissue from different sources has been observed by others (Jackson, Choo et al. 1995). The main component contributing to the unique spectra of stroma is collagen. The bulk of the cervical stroma is composed of extracellular collagen generated by connective tissue fibroblasts. The large proportion of collagen manifests itself as an increase in the AI/AII intensity ratio. By comparison, the AI/AII intensity ratio for a pure protein such as BSA shown in Figure 3:5 is approximately 0.85. Table 4.1 shows that the AI/AII ratio for stroma is lower than pure protein, but still approximately 15% higher than found in normal epithelium. The predominant $\alpha$ helical secondary structure and unique amino acid composition of collagen is responsible for the elevated AI/AII intensity ratio and the distinctive amide III vibration seen in cervical stroma. In

contrast to most proteins, more than half of the amino acid sequence of collagen is made up of glycine and proline residues. These residues help maintain the helical nature of collagen. The amino acid distribution of BSA is much more heterogeneous and so the spectra shows a subdued amide III band. Therefore it seems reasonable to suggest that these two residues are responsible for the triad of peaks at 1206, 1235 and 1280 $cm^{-1}$. In addition, the low frequency triplet set at 1031, 1060 and 1080 $cm^{-1}$ are distinctive in stroma. These vibrations fall into the C-O and C-C stretching regions. The extracellular matrix of connective tissues contains carbohydrates in the form of glycosaminoglycans as well as a small number of sugar residues attached to collagen. This can be seen in the PAS stained section shown in Figure 3.6. Therefore, this group of low frequency bands can be assigned to carbohydrate components in the connective tissue matrix. Interestingly, this area is quite distinct from the basal layer spectra of the cervical epithelium as shown in Figure 4.2. Because of the difficulty in observing the basement membrane, it is not clear whether the basement membrane is measured as part of the basal layer. The basement membrane is composed of a complex mixture of mucopolysaccarides, glycoproteins and heteroglycans that could conceivably contribute to the spectra in the low frequency region of basal layer spectra.

The acquisition of uncontaminated basal layer spectra is important for any comparison with neoplastic epithelium. Since neoplastic lesions arise from damaged basal cells and histologically tend to resemble undifferentiated epithelium, high quality uncontaminated basal layer spectra are essential for comparison. Therefore, the identification of stromal contamination is extremely important. Examination of the

amide III region facilitates this determination. Figure 4.2 compares the spectrum of a basal layer from a normal biopsy with the basal layer from the same biopsy contaminated with stromal overlap. The appearance of shoulders at 1206 and 1280 $cm^{-1}$ on the 1239 $cm^{-1}$ band are clearly indicative of stromal influence. In addition the presence of a band at 1334 $cm^{-1}$, absent in the epithelium (see Figures 3:4), aids in this interpretation. There is also evidence of stromal contribution in the low frequency region. The suppressed feature at 1031 $cm^{-1}$ in normal basal spectra becomes more prominent but the ratio with the 1081 $cm^{-1}$ remains low when stromal contamination is present. Similarly the band at 1157 $cm^{-1}$ in the basal layer is reduced. Figure 4.2 also illustrates the extreme care that must be taken when evaluating the band at 1239 $cm^{-1}$ This band is formed as a combination of contributions from the amide III and anti-symmetric phosphate vibration. Clearly its intensity is going to revolve around the contributions from both protein and nucleic acids (see Figure 3:5) Therefore, changes in this band should be evaluated with respect to the presence of other effects elsewhere in the spectra.

The spectra collected from the different layers of non-neoplastic cervical epithelium are consistent with the maturation and differentiation processes known to occur in normal cervical epithelium. These effects are principally observed as a relative increase in the glycogen content in the epithelial layers starting with the parabasal layer and intensifying to the superficial layer. The basal layer contains little or no glycogen which agrees with morphological observations. The decreasing N/C ratio that occurs during maturation is not seen, indicating that the cytoplasm is the dominant feature contributing to the spectral pattern in normal cervical epithelium

Table 4:1 Glycogen(G1)/amide I and amide I/amide II intensity ratios observed for the different layers of normal cervical epithelium.

| Layer | G1/AI* | AI/AII* |
|---|---|---|
| Superficial | 0.30 ±0.10 | 0.52 ±0.06 |
| Intermediate | 0.29 ±0.08 | 0.49 ±0.02 |
| Parabasal | 0.20 ±0.07 | 0.49 ±0.02 |
| Basal | NA | 0.51 ±0.02 |
| Stroma | NA | 0.64 ±0.02 |

*Average of 5 samples: NA, Not calculated

Table 4:2 Amide II maximum and half bandwidths ($\Delta\nu_{\frac{1}{2}}$) for the 5 different layers in the same sample of benign cervical epithelium.

| *Layer* | *Amide II maximum ($cm^{-1}$)* | *$\Delta\nu_{\frac{1}{2}}$ ($cm^{-1}$)* |
|---|---|---|
| Superficial | 1550 | 64 |
| Intermediate | 1541 | 55 |
| Parabasal | 1542 | 53 |
| Basal | 1543 | 53 |
| Stroma | 1548 | 70 |

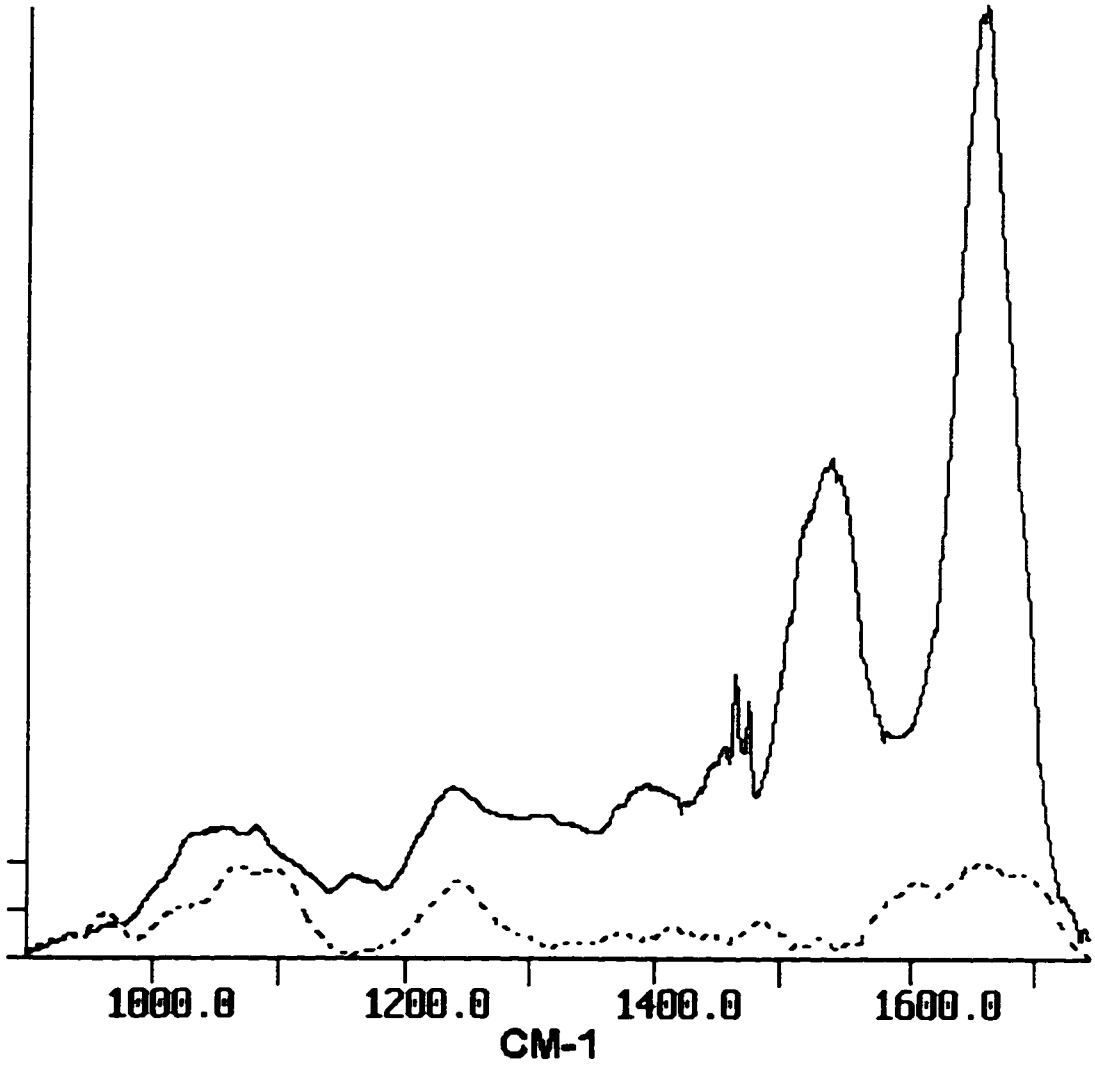


Figure 4:1 FT-IRM spectra between 850 and 1750 $cm^{-1}$ of normal basal layer epithelium (solid) and IR spectra of DNA (dot).

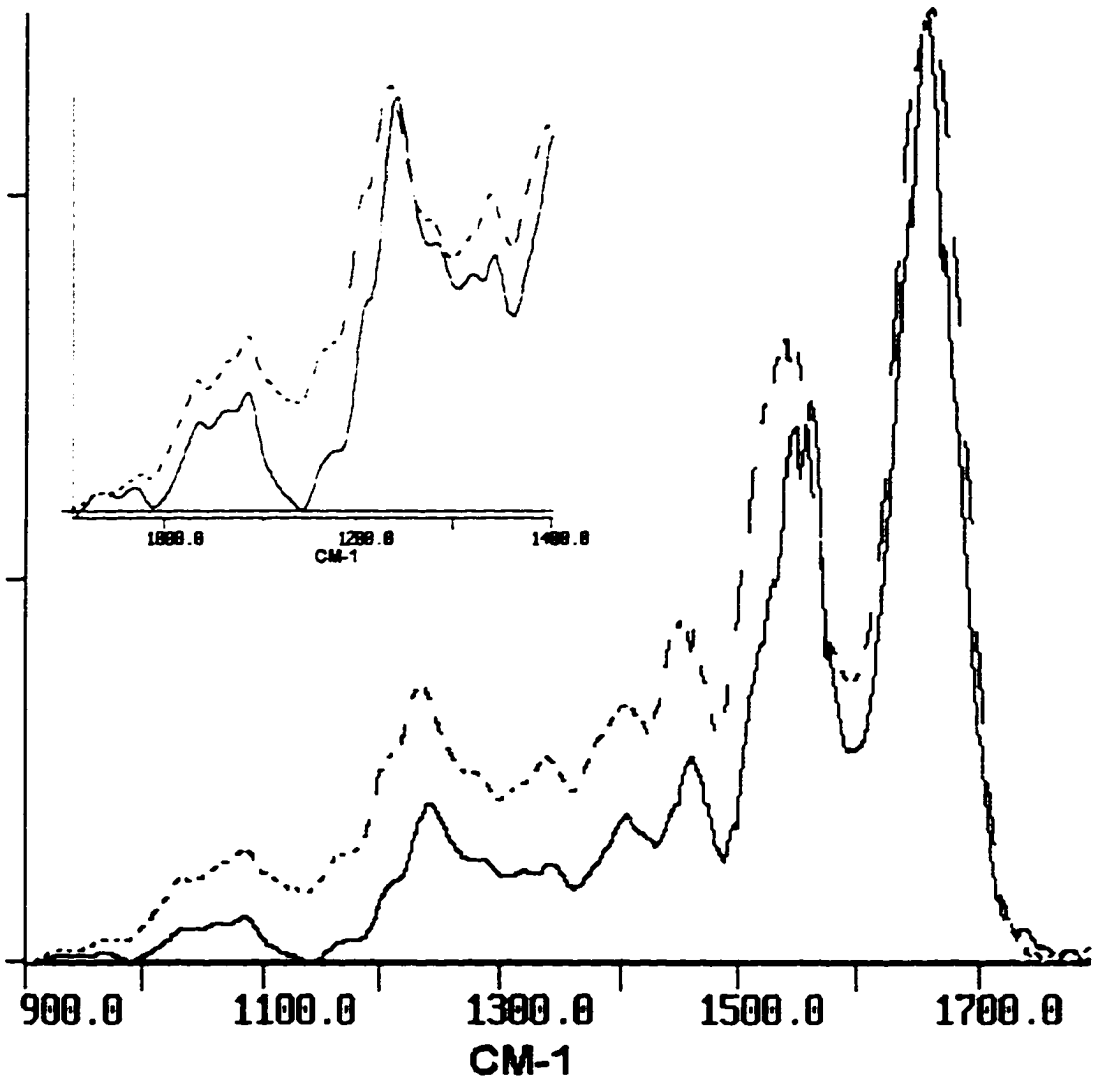


Figure 4:2 FT-IRM collected between 1800 and 900 $cm^{-1}$ of cervical stroma (dot) and normal basal layer (solid) that is contaminated with stromal overlap. Inset: expanded view between 900 and 1400 $cm^{-1}$.

## 4.2 Neoplastic Cervical Squamous Epithelium:

One of the most important characteristics evaluated in histopathology is the degree of differentiation in a neoplastic lesion. In dysplastic cervical epithelium this is indicated by the presence of undifferentiated cells encompassing larger portions of the cervical epithelium. In invasive carcinoma, these morphologically undifferentiated cells reach the surface of the cervical epithelium. In conjunction with the defect in differentiation in squamous cell carcinoma, the epithelium becomes thinner as abortive maturation and abatement of stratification occur. A consequence of the cessation of differentiation is the parallel loss of histologic landmarks of maturing cervical epithelium. Therefore measurements can no longer be based on the relative positions of layers that are no longer present. This effect is mirrored in the surface spectra of neoplastic cervical epithelium. The spectra collected from the surface of a neoplastic lesions resemble the basal layer spectra obtained from normal cervical epithelium. This can be reproduced in two different grades of squamous cell carcinoma. However, it must be stressed that this does not imply that the cells at the surface of the lesion are the same as the basal cells of normal cervical epithelium. In fact, while the two have similar spectral signatures, there are distinct differences in the spectra and morphology between normal basal and neoplastic cells. In essence, the observation of spectral features at the surface that resemble cells lower in the epithelium is in agreement with

the histolopathologic observations of undifferentiated cells at the surface of squamous cell lesions.

Figure 4:3 is a comparison of neoplastic surface spectra with normal superficial and basal layers. It is obvious that the neoplastic surface cells do not resemble the normal superficial layer spectra obtained from the surface of normal cervical epithelium. The principal differences between the neoplastic surface and superficial layer spectra is the complete loss of the glycogen signature. Pathologically this occurs for two reasons. First, the cells have differentiated into an alternate pathway and do not follow the normal course of maturation. An integral part of the maturation process in cervical epithelium is the accumulation of intracytoplasmic glycogen. Secondly, neoplasms show an increase in anaerobic metabolism for which glycogen is the main source. Histologically, the effect is seen as a decreased PAS reaction throughout the epithelium. Figure 3:18 shows that the surface layer of a neoplastic lesion is still capable of exhibiting a positive PAS reaction. Diastase treatment of the section shown in Figure 3:18 fails to inhibit PAS positive staining, indicating that the reaction does not involve glycogen. This raises the possibility that the stain is reacting with other PAS labile C-C bonds. This may explain the prominent band at 1080 $cm^{-1}$ in the neoplastic surface spectra. This band is assigned to the C-C stretching vibration. In fact, the 1151 $cm^{-1}$ band in neoplastic surface spectra is reduced concurrent with the appearance of a band at 1174 $cm^{-1}$. This indicates a loss of the C-O stretching vibration or a change in the origin of the predominate species responsible for its contribution to the observed frequency. Nevertheless, the reason for an increased availability of PAS labile carbon bonds is unclear.

Figure 4:3 also demonstrates the similarity between neoplastic surface and normal basal layer spectra. The overall features of these two spectra are comparable, showing similar intensities and frequencies for the major bands. The similarities are seen in both grades of disease studied. Consistent with the differences observed between normal superficial and normal basal layers, the ratio between the 1314 $cm^{-1}$ and amide III band is reversed in the neoplastic surface spectra. In contrast to the normal basal layer, the neoplastic surface layer exhibits a narrowing of the absorbance between 980 and 1140 $cm^{-1}$. The band found at 1031 $cm^{-1}$ in the normal basal layer is reduced which causes the region to become less well defined. The 1060 $cm^{-1}$ band also appears to be reduced leaving the 1081 $cm^{-1}$ band as the most conspicuous feature in the low frequency region. The loss of the well defined basal layer features indicates that these neoplastic surface cells are not basal cells. In fact, the decay of spectral features in this range becomes more noticeable as the cells become more anaplastic.

In the basal area of the neoplastic epithelium, the cells are even less differentiated than at the surface. The designation of this area as basal is purely descriptive. These cells are distal to the surface and have migrated past the relative location of a normal basal layer. The presence of stromal papillae that extend into the upper parts of the epithelium demonstrates the invasive nature of this process (compare Figures 3:2 and 3:15). The cells are not basal cells in the classical sense. They are neoplastic cells distinguishable by their increased N/C ratio and pleomorphic character . The cells have large hyperchromatic nuclei with aggregated chromatin and frequent nucleoli. The cell boarders are indistinct and the cytoplasmic volume is reduced and devoid of glycogen. A comparison of a neoplastic basal and normal basal

layer are shown in Figure 4:4. Grossly, the amide bands are fairly consistent with those found in the normal epithelial layers. The most notable differences are the reduction of the band at 1314 $cm^{-1}$ as well as the elevated AIII/AII ratio in the neoplastic basal cells. In normal basal layers, this ratio is on average 10% lower.

As in previous comparisons, the primary differences between normal and neoplastic basal layer spectra are found in the low frequency region. The region between 980 and 1140 $cm^{-1}$ has lost the distinguishing features observed in normal basal layers. The distinctive band at 1081 $cm^{-1}$ that was present in the surface spectra is no longer visible in the neoplastic basal layer. Similarly, the band at 1151 $cm^{-1}$ is reduced and the feature at 1174 $cm^{-1}$ has become dominant. This trend is consistent with the changes seen in the neoplastic surface spectra. In contrast to the histology on the surface, the basal area is PAS negative indicating a lack of PAS labile carbon bonds. This is reflected in the loss of the dominant 1081 $cm^{-1}$ band in the spectra of neoplastic basal cells. It also suggests that the species responsible for this band are no longer a governing feature in the neoplastic basal layer. In addition, there is the loss of the C-O stretching band and the appearance of a band at 1174 $cm^{-1}$ indicating a possible shift in the carbohydrate or protein complement of the neoplastic cells.

There is evidence in the neoplastic basal spectra of a greater presence of nucleic acids. A more intense band at 965$cm^{-1}$ is clearly visible, which is found in the spectrum of pure DNA. In addition, the broad low frequency absorbance has a high frequency shoulder. This feature indicates the possible contribution from the 1095 $cm^{-1}$ band found in DNA. Moreover, there is an increase in the ratio of AIII/AII,

suggesting that there is a greater contribution of nucleic acids to the overall spectra. However, there is no significant change to the amide I/II intensity ratio. The combined contribution of protein and nucleic acid to the AIII make direct assignment difficult. Therefore, the change in amide III/II ratio may occur contemporaneously with a change in the amide I/II intensity ratio. The histopathology of the neoplastic basal cells is in agreement with this interpretation. An important feature observed in neoplastic cells of invasive squamous cell carcinoma is an aneuploid DNA content (Fu, Cheng et al. 1989; Mariuzzi, Santinelli et al. 1992; Steinbeck, Heselmeyer et al. 1995, Heselmeyer, Schrock et al. 1996). Examination of Figure 3:15 shows that many of the nuclei have large areas of euchromatin, unmistakable because of their lack of hematoxylin staining. These regions have elevated gene activity which causes a reduction in the local heterochromatic DNA and protein concentration. Chromosomal abnormalities will also contribute to this effect. In comparison to the basal layer of normal epithelium, the nuclear area of neoplastic cells is larger and displays more euchromatin. This gives the nuclei of neoplastic cells a greater capability to transmit infrared radiation. Similarly, increased transcriptional activity will increase the cytoplasmic ribosome concentration. The result is a larger influence of nucleic acids in the spectra of neoplastic basal cell layer. This effect is not seen in the neoplastic surface spectra because these cells have differentiated and therefore have reduced N/C ratios and a greater degree of heterochromatin. This effect is observed regardless of the grade of disease and therefore present in both well and moderately differentiated lesions.

Figure 4:5 is a comparison between neoplastic basal cells and invasive tumor cells from a well differentiated tumor (see Figure 3:21) and a moderately differentiated tumor. In the center of the tumor nests of the well differentiated lesion, there are areas of keratinization from which spectra were collected that is also shown in Figure 4:5. The tumor cells have spectral characteristics that are similar to those in the neoplastic basal cells. The 965 $cm^{-1}$ band is present as is a high frequency shoulder at 1095 $cm^{-1}$. There are no distinct bands within the low frequency region except for the broad absorbance between 980 and 1140 $cm^{-1}$. The two small bands observed at 1151 and 1174 $cm^{-1}$ are absent in the well differentiated tumor. In the moderately differentiated tumor the 1174 $cm^{-1}$ band is present. The amide III/II ratio is elevated for both grades as in the neoplastic basal layer. The band at 1314 $cm^{-1}$ is more clearly visible in the tumor cells than in the neoplastic basal layer. These findings are consistent with the histopathology for the different grades of carcinoma. The tumor cells in the well differentiated lesion are slightly better differentiated than the neoplastic basal cells of the same lesion as indicated by their organization in Figure 3:2. However, the tumor does not approach the degree of differentiation, histologically or spectrally, as the neoplastic surface cells. The tumor is PAS negative exhibiting virtually no reaction. In contrast to the well differentiated lesion, the tumor cells in the moderately differentiated lesion exhibit characteristics of both neoplastic basal and invasive tumor cells of the well differentiated lesion. The moderately differentiated tumor cells have the same broad absorbance between 980 and 1140 $cm^{-1}$ observed in neoplastic spectra. In agreement with the well differentiated tumor cells, the 1174 $cm^{-1}$ band is present in the moderately differentiated tumor cells. In addition,

the band at 1314 $cm^{-1}$ observed in the well differentiated tumor cells is also present in the moderately differentiated tumor. These results indicate that the moderately and well differentiated tumors are influenced by a similar constituent. In moderately differentiated lesions, the majority of the cells produce keratin even though they show fewer architectural and organizational characteristics than their well differentiated counterpart. In the well differentiated tumors, the cells produce keratin as they organize and mature slightly with in the tumor mass. Therefore it is reasonable to speculate that the moderately and well differentiated tumors show an influence from cellular keratinization. By comparison, the keratin spectra shown in Figure 4:5 has features found in both the well and moderately differentiated tumor cell spectra. The maximum of the low frequency region is centered over the 1081 $cm^{-1}$ band in keratin. The 1174 $cm^{-1}$ band is present, as is the 1314 $cm^{-1}$ absorbance. In addition, the AI/AII intensity ratios are slightly elevated. However, supplementary data in the form of additional samples and measurements is necessary to clearly evaluate this hypothesis.

The keratin spectra shown in Figure 4:5 is an important component of this disease process since both grades of neoplasia express it in abundance. However, this spectra should not be confused with the spectra of pure keratin. There are over 20 different iso-types of keratin found in normal cervical squamous epithelium (Smedts, Ramaekers et al. 1993). While they may be spectrally very similar, tumor cells may produce these proteins with different primary sequences as well as post translational modifications. Keratin pearls also contain additional proteins and nucleic acid material whose influence on the overall spectral pattern should be taken into account.

In conclusion, the spectral pattern of neoplastic cervical squamous epithelium can be described in terms of two dominant characteristics. First, the presence of basal cell-like spectral patterns in improper anatomical locations. Second, the neoplastic spectral pattern is dominated by a combination of nucleic acids and protein features. These characteristics are more prominent due to the absence of a large spectral contribution from glycogen.

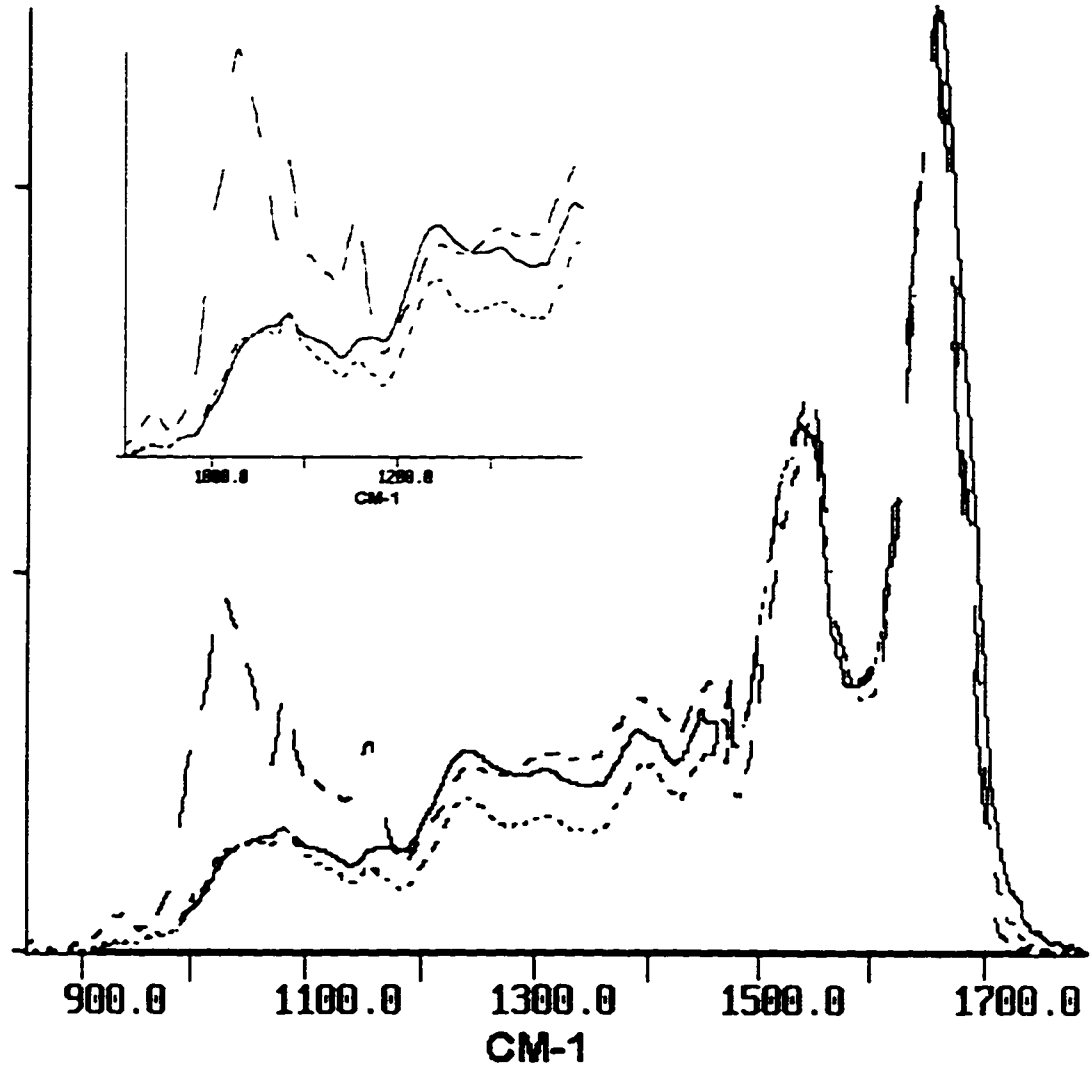


Figure 4:3 FT-IRM spectra between 850 and 1800 $cm^{-1}$ comparing neoplastic surface cells (solid) normal basal layer cells (dot) and normal superficial layer (dashed). Inset: expanded view between 900 and 1400 $cm^{-1}$.

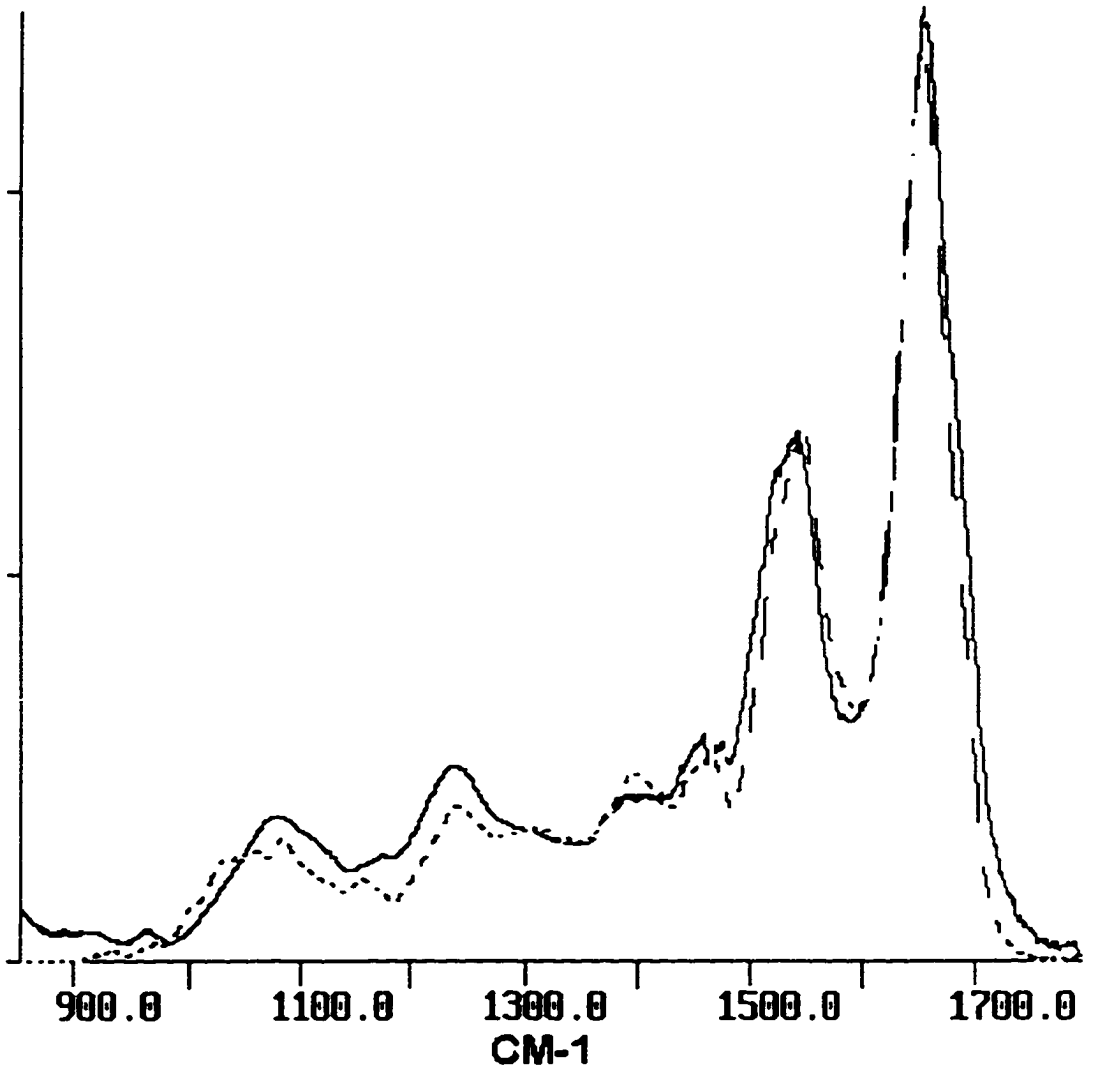


Figure 4:4 FT-IRM spectral comparison between 850 and 1800 $cm^{-1}$ of normal basal cells (dashed) and neoplastic basal cells (solid).

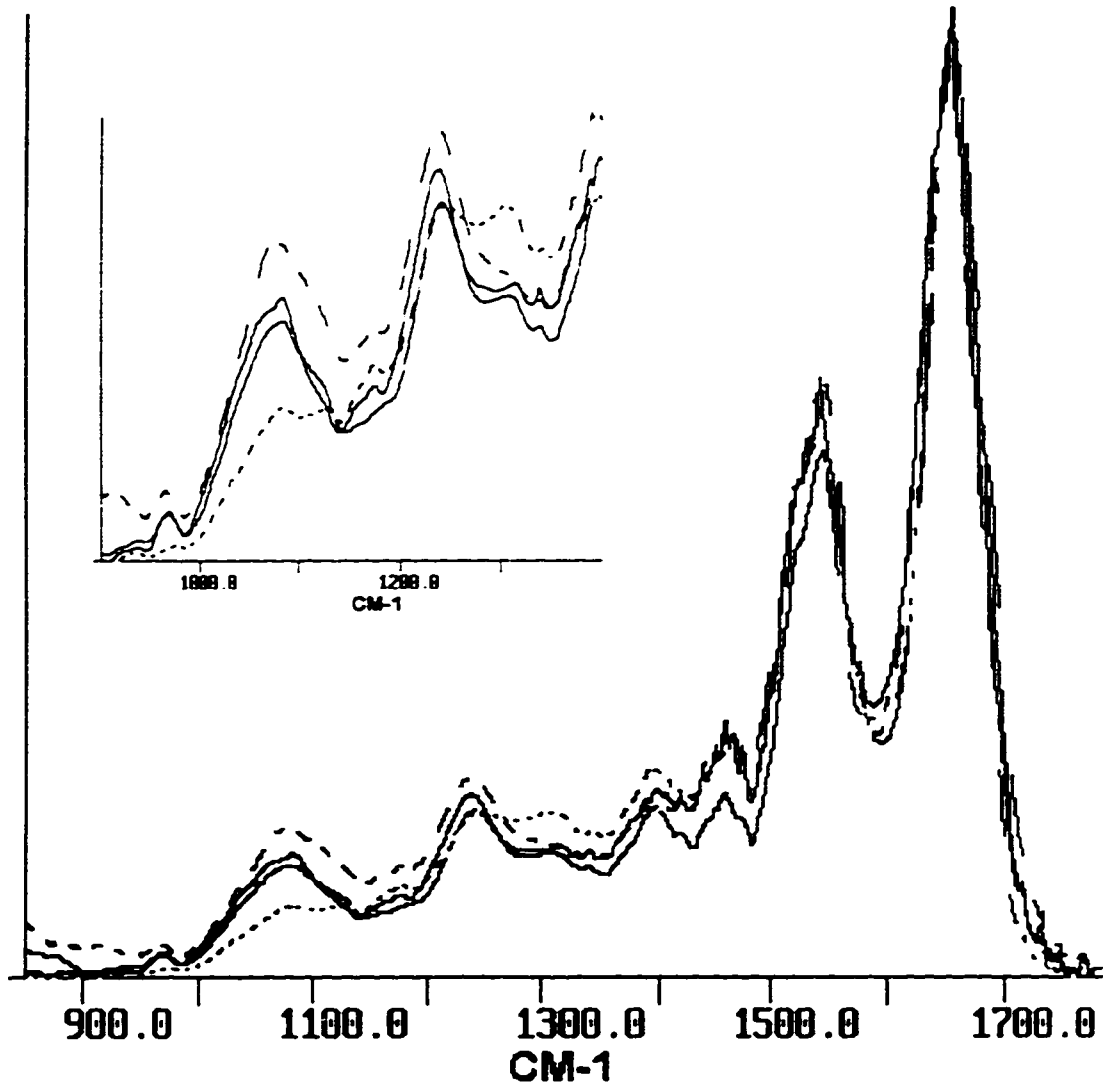


Figure 4:5 FT-IRM comparison between 850 and 1800 of well differentiated tumor cells (solid), keratin pearl (dot), neoplastic basal cells (dashed) and moderately differentiated tumor cells (solid). Inset: expanded view from 900 to 1400 $cm^{-1}$.

## 4.3 Summary:

In conclusion, the results of this study indicate that FT-IRM is a method capable of distinguishing different histological components of cervical squamous epithelium. The anatomic layers present in normal squamous epithelium can be observed and measured accurately and reproducibly from different samples. These layers exhibit different spectral signatures depending on their anatomical location and cellular composition. The results from these measurements correlate well with the normal differentiation and maturation processes observed in normal cervical epithelium. In contrast, measurements of neoplastic epithelium show a progressive loss of spectral information. This is consistent with the morphologic changes seen in neoplastic epithelium in that the cells become anaplastic. Neoplastic cells lose their ability to differentiate and mature resulting in a loss of the morphological characteristics previously associated with maturation. These changes are reflected spectrally as the loss of distinct features. The FT-IRM results also coincide with histopathology observations of undifferentiated cells in anatomic locations ordinarily occupied by differentiated cells. Therefore, FT-IRM is a powerful method for characterizing and observing the processes of differentiation and transformation in cervical epithelium. In closing, FT-IRM is capable of accurate and reproducible infrared measurement of precise anatomic locations based on correlation with observed histopathology in formalin fixed paraffin embedded tissue.

# Bibliography

Alben, J. O. and Caughey W. S. (1968). "An infrared study of bound carbon monoxide in the human red blood cell, isolated hemoglobin and heme carbonyls." Biochemistry 7(1): 175-183.

Austin, J. P., Degefu S., et al. (1994). "Cervical carcinoma in women less than 35 years of age." Southern Medical Journal **87**(3): 375-9.

Benedet, J. L. and Anderson G. H. (1996). "Stage IA carcinoma of the cervix revisited." Obstetrics & Gynecology **87**(6): 1052-9.

Benedet, J. L., Anderson G. H., et al. (1992). "A comprehensive program for cervical cancer detection and management." American Journal of Obstetrics & Gynecology **166**(4): 1254-9.

Benedetti, E., Palatresi M. P., et al. (1986). "Infrared characterization of nuclei isolated from normal and leukemic (B-CLL) lymphocytes: Part III." Applied Spectroscopy **40**(1): 39-43.

Benedetti, E., Palatresi M. P., et al. (1985). "New possibilities of research in chronic lymphatic leukemia by means of Fourier transform-infrared spectroscopy-II." Leukemia Research **9**(8): 1001-1008.

Benedetti, E., Papineschi F., et al. (1984). "Analytical infrared spectral differences between human normal and leukaemic cells (CLL) -I." Leukemia Research **8**(3): 483-489.

Benedetti, E., Teodori L., et al. (1990). "A new approach to the study of human solid tumor cells by means of FT-IR microspectroscopy." Applied Spectroscopy **44**(8): 1276-1280.

Benedetti-Panici, P., Maneschi F., et al. (1996). "Lymphatic spread of cervical cancer: an anatomical and pathological study based on 225 radical hysterectomies with systematic pelvic and aortic lymhadenectomy." Gynecologic Oncology **62**(1): 19-24.

Beral, V., Hermon C., et al. (1994). "Cervical cancer." Cancer Surveys **19-20**: 265-85.

A. Ferenczy, Anatomy and histology of the cervix. In: Blaustein, A. Ed. Pathology of the female genital tract. Second ed., New York: Springer Verlag, 1982; Chap. 5, 119-135.

A. Ferenczy, Carcinoma and other tumors of the cervix. In: Blaustein, A. Ed. Pathology of the female genital tract. Second ed., New York: Springer Verlag, 1982, Chap. 9, 184-219.

A. Ferenczy, Cervical Intraepithelial Neoplasia. In: Blaustein, A. Ed. Pathology of the female genital tract. Second ed., New York: Springer Verlag, 1982; Chap. 7, 156-175.

Blout, E. R. and Mellors R. C. (1949). "Infrared spectra of tissues." Science **110**: 137-138.

Bremer, G. L., Tiebosch A. T., et al. (1995). "Basement membranes in cervical cancer: relationship to pelvic lymph node metastasis and prognosis." Gynecologic Oncology **57**(3): 351-5.

Cannistra, S. A. and Niloff J. M. (1996). "Cancer of the uterine cervix." New England Journal of Medicine **334**(16): 1030-1038.

A: Chiriboga, L., Xie P., et al. (1997). "Infrared studies of the differentiation and maturation of epithelial cells in the human cervix." Nature Submitted 4/97.

B: Chiriboga, L., Xie P., et al. (1997). "A comparison of infrared spectra of biopsies of healthy cervical squamous epithelium and of healthy exfoliated cervical cells." Nature Submitted 3/97.

C: Chiriboga, L., Xie P., et al. (1997). "Infrared spectroscopy of squamous and columnar tissue and cells from the human cervix." Biospectroscopy Submitted 4/97

Comerci, J. T., Jr., Runowicz C. D., et al. (1996). "Altered expression of transforming growth factor-beta 1 in cervical neoplasia as an early biomarker in carcinogenesis of the uterine cervix." Cancer **77**(6): 1107-14.

Cristoforoni, P., Favre A., et al. (1995). "Expression of a novel beta 1 integrin in the dysplastic progression of the cervical epithelium." Gynecologic Oncology **58**(3): 319-26.

Daudon, M., Marfisi C., et al. (1991). "Investigation of urinary crystals by Fourier transform infrared microscopy." Clinical Chemistry **37**(1): 83-7.

Diem, M. (1993). Introduction to modern vibrational spectroscopy. New York, John Wiley and Sons.

DiPaolo, J. A., Popescu N. C., et al. (1993). "Cellular and molecular alterations in human epithelial cells transformed by recombinant human Papillomavirus DNA." Critical Reviews in Oncogenesis **4**(4): 337-60.

Dong, A., Messerschmidt R. G., et al. (1988). "Infrared spectroscopy of a single cell--the human erythrocyte." Biochemical & Biophysical Research Communications **156**(2): 752-6.

Elliott, P. (1995). "Lymph node metastases, cell type, age, HPV status and type, neoadjuvant chemotherapy and treatment failures in cervical cancer." International Journal of Gynecology & Obstetrics **49**(Suppl): S17-25.

Estepa-Maurice, L., Hennequin C., et al. (1996). "Fourier transform infrared microscopy identification of crystal deposits in tissues: clinical importance in various pathologies." American Journal of Clinical Pathology **105**(5): 576-82.

Fu, Y. S., Cheng L., et al. (1989). "DNA ploidy analysis of cervical condyloma and intraepithelial neoplasia in specimens obtained by punch biopsy." Analytical and Quantitative Cytology and Histology **11**(3): 187-195.

Gershenson, D. M., DeCherney A. H., et al. (1993). Operative Gynecology. Philadelphia, W.B. Saunders Compony.

Girardi, F., Burghardt E., et al. (1994). "Small FIGO stage IB cervical cancer." Gynecologic Oncology **55**(3 Pt 1): 427-32.

Gustafsson, L., Sparen P., et al. (1995). "Low efficiency of cytologic screening for cancer in situ of the cervix in older women." International Journal of Cancer **63**(6): 804-9.

Heselmeyer, K., Schrock E., et al. (1996). "Gain of chromosome 3q defines the transition from severe dysplasia to invasive carcinoma of the uterine cervix." Proceedings of the National Academy of Sciences of the United States of America **93**(1): 479-84.

Iwasaka, T., Matsuo N., et al. (1996). "Non-detection of human Papillomavirus DNA in cervical dysplasia and disease progression [letter]." Lancet **348**(9023): 333-4.

Jackson, M., Choo L. P., et al. (1995). "Beware of connective tissue proteins: assignment and implications of collagen absorptions in infrared spectra of human tissues." Biochimica et Biophysica Acta **1270**(1): 1-6.

Jackson, M. and Mantsch H. H. (1995). "The use and misuse of FTIR spectroscopy in the determination of protein structure." Critical Reviews in Biochemistry & Molecular Biology **30**(2): 95-120.

Jobsis, F. F. (1977). "Noninvasive, infrared monitoring of cerebral and myocardial oxygen sufficiency and circulatory parameters." Science **198**(4323): 1264-7.

Jones, C. (1995). "Cervical cancer: is herpes simplex virus type II a cofactor?" Clinical Microbiology Reviews **8**(4): 549-56.

Jones, W. B., Mercer G. O., et al. (1993). "Early invasive carcinoma of the cervix." Gynecologic Oncology **51**(1): 26-32.

Konishi, I., Fujii S., et al. (1991). "Immunohistochemical analysis of estrogen receptors, progesterone receptors, Ki-67 antigen and human Papillomavirus DNA in normal and neoplastic epithelium of the uterine cervix." Cancer **68**(6): 1340-1350

Kwiatkoski, J. M. and Reffner J. A. (1987). "FT-IR microspectrometry advances." Nature **328**(27): 839-838.

Levine, A. J., Harper J., et al. (1993). "HPV DNA and the risk of squamous intraepithelial lesions of the uterine cervix in young women." American Journal of Clinical Pathology **100**(1): 6-11.

Mariuzzi, G., Santinelli A., et al. (1992). "Cytometric evidence that cervical intraepithelial neoplasia I and II are dysplasias rather than true neoplasias. An image analysis study of factors involved in the progression of cervical lesions." Analytical & Quantitative Cytology & Histology **14**(2): 137-47.

Mason, J. T. and TJ O. L. (1991). "Effects of formaldehyde fixation on protein secondary structure: a calorimetric and infrared spectroscopic investigation." Journal of Histochemistry & Cytochemistry **39**(2): 225-9.

Maxwell, J. C., Barlow C. H., et al. (1974). "The utility of infrared spectroscopy as a probe of intact tissue: determination of carbon monoxide and hemeproteins in blood and heart muscle." Biochemical & Biophysical Research Communications **61**(1): 230-6.

Maxwell, J. C. and Caughey W. S. (1978). "Infrared spectroscopy of ligands, gases and other groups in aqueous solutions and tissue." Methods in Enzymology **54**: 302-323.

Mittal, K. R., Demopoulos R. I., et al. (1993). "Proliferating cell nuclear antigen (cyclin) expression in normal and abnormal cervical squamous epithelia." American Journal of Surgical Pathology **17**(2): 117-22.

Morris, B. J., Lee C., et al. (1995). "Fourier Transform infrared spectroscopy of dysplastic, Papillomavirus-positive cervicovaginal lavage specimens." Gynecologic Oncology **56**: 245-249.

Munoz, N., Bosch F. X., et al. (1994). "The role of HPV in the etiology of cervical cancer." Mutation Research **305**(2): 293-301.

Nanogaki, H., Fujii S., et al. (1990). "Estrogen receptor localization in normal and neoplastic epithelium of the uterine cervix." Cancer **66**(12): 2620-2627.

Nieminen, P., Kallio M., et al. (1995). "The effect of mass screening on incidence and mortality of squamous and adenocarcinoma of cervix uteri." Obstetrics & Gynecology **85**(6): 1017-21.

Noda, K. (1992). "Cervical intraepithelial neoplasia and microinvasive carcinoma of the cervix." Current Topics in Pathology **85**: 57-80.

O'Leary, T. and Levin I. W. (1985). "Secondary structure of endocrine amyloid: infrared spectroscopy of medullary carcinoma of the thyroid." Laboratory Investigation **53**(2): 240-2.

O'Leary, T. J. (1989). "IR Microspectroscopy of pathological tissue." SPIE **1145**: 534-535.

O'Leary, T. J., Engler W. F., et al. (1989). "Infrared microspectroscopy of human tissue." Applied Spectroscopy **43**(6): 1095-1097.

Ostor, A. G. (1993). "Studies on 200 cases of early squamous cell carcinoma of the cervix." International Journal of Gynecological Pathology **12**(3): 193-207.

Qualters, J. R., Lee N. C., et al. (1992). "Breast and cervical cancer surveillance, United States, 1973-1987." MMWR CDC Surveillance Summaries **41**(2): 1-7.

Raju, G. C. (1994). "Expression of the proliferating cell nuclear antigen in cervical neoplasia." International Journal of Gynecological Pathology **13**(4): 337-41.

Rakar, S., Kovacic J., et al. (1994). "Cervical carcinoma in young women." European Journal of Obstetrics, Gynecology, & Reproductive Biology **55**(1): 19-20.

Rigas, B., Morgello S., et al. (1990). "Human colorectal cancers display abnormal Fourier-transform infrared spectra." Proceedings of the National Academy of Sciences of the United States of America **87**(20): 8140-4.

Rigas, B. and Wong P. T. (1992). "Human colon adenocarcinoma cell lines display infrared spectroscopic features of malignant colon tissues " Cancer Research **52**(1): 84-8.

Rosai, J. (1989). Ackerman's Surgical Pathology. St. Louis, Mosby Year books.

Saegusa, M., Takano Y., et al. (1995). "The possible role of bcl-2 expression in the progression of tumors of the uterine cervix." Cancer **76**(11): 2297-303.

Sheehan, D. C. (1980). Theory and Practice of Histotechnology. St. Louis, C.V. Mosby.

Shoji, Y., Saegusa M., et al. (1996). "Correlation of apoptosis with tumor cell differentiation, progression, and HPV infection in cervical carcinoma." Journal of Clinical Pathology **49**(2): 134-8.

Shroyer, K. R., Lovelace G. S., et al. (1993). "Detection of human Papillomavirus DNA by in situ hybridization and polymerase chain reaction in human Papillomavirus equivocal and dysplastic cervical biopsies." Human Pathology **24**(9): 1012-6.

Shurbaji, M. S., Brooks S. K., et al. (1993). "Proliferating cell nuclear antigen immunoreactivity in cervical intraepithelial neoplasia and benign cervical epithelium." American Journal of Clinical Pathology **100**(1): 22-6.

Smedts, F., Ramaekers F. C., et al. (1993). "The dynamics of keratin expression in malignant transformation of cervical epithelium: a review." Obstetrics & Gynecology **82**(3): 465.

Steinbeck, R. G., Heselmeyer K. M., et al. (1995). "The relationship between proliferating cell nuclear antigen (PCNA), nuclear DNA content and mutant p53 during genesis of cervical carcinoma." Acta Oncologica **34**(2): 171-6.

Stewart, C. J. and McNicol A. M. (1992). "Distribution of type IV collagen immunoreactivity to assess questionable early stromal invasion." Journal of Clinical Pathology **45**(1): 9-15.

Stone, K. M., Zaidi A., et al. (1995). "Sexual behavior, sexually transmitted diseases, and risk of cervical cancer." Epidemiology **6**(4): 409-14.

Vecchione, A., Cermele C., et al. (1994). "p53 expression and genetic evidence for viral infection in intraepithelial neoplasia of the uterine cervix." Gynecologic Oncology **55**(3 Pt 1): 343-8.

Wong, P. T., Wong R. K., et al. (1991). "Infrared spectroscopy of exfoliated human cervical cells: evidence of extensive structural changes during carcinogenesis."

Proceedings of the National Academy of Sciences of the United States of America **88**(24): 10988-92.

Wong, P. T. T. and Rigas B. (1990). "Infrared spectra of microtome sections of human colon tissue." Applied Spectroscopy **44**(10): 1715-1718.

Wong, P. T. T., Wong R., et al. (1993). "Pressure-tuning FT-IR study of human cervical tissue." Applied Spectroscopy **47**(7): 1058-1063.

Wood, B. R., Quinn M. A., et al. (1996). "An investigation into FTIR spectroscopy as a biodiagnostic tool for cervical cancer." Biospectroscopy **2**: 143-153.